RADAR ALTIMETRY METHODS FOR SOLID EARTH GEODYNAMICS STUDIES

by

Hyong Ki Lee

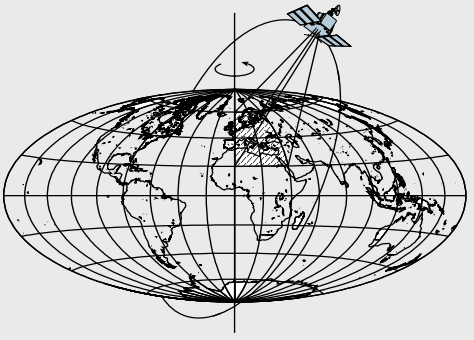

Report No. 489

Geodetic Science and Surveying

The Ohio State University
Columbus, Ohio 43210

September 2008

RADAR ALTIMETRY METHODS
FOR SOLID EARTH GEODYNAMICS STUDIES

by

Hyong Ki Lee

The Ohio State University

2008

ABSTRACT

Satellite radar altimetry, which was initially designed for accurate measurements of sea surface height, has been demonstrated to be applicable to non-ocean surfaces as well. In this study, three different applications of satellite altimetry to geodynamics studies have been examined: solid Earth crustal deformation due to Glacial Isostatic Adjustment (GIA) over Hudson Bay, North America, water level fluctuation over vegetated wetlands of Louisiana, and ice sheet elevation change over the Amundsen Sea sector, West Antarctica. For efficient altimetry data processing, high-rate (10-Hz for TOPEX, 18-Hz for Environmental Satellite (Envisat)) regional stackfiles were developed based on the original low-rate (1-Hz) global ocean stackfile. A modified threshold retracker has also been developed for more accurate land radar waveform retracking. 90-m resolution C-band Shuttle Radar Topography Mission (SRTM) Digital Elevation Model (DEM) plays an important role to be used as a reference surface to select an optimal retracker, to correct surface gradient errors, and to calculate land surface anomalies over Hudson Bay. As a result, the crustal vertical motion is estimated from TOPEX decadal (1992-2002) time series over land surfaces with height variation (in terms of standard deviation) less than 2 m. The estimated vertical motion has been compared with the vertical motion derived from Gravity Recovery and Climate Experiment (GRACE) satellite and several GIA models. It agrees well with the laterally varying 3D GIA model, RF3S20 (β=0.4) with differences of -0.1 ± 2.2 mm/year. It is anticipated that the new observation from this study can be used to provide additional constraints for GIA model improvement. The 10-Hz stackfile procedure has also been utilized to observe the Louisiana wetland water level variations over each of 10-Hz stackfile bin with along-track spacing of ~660 meter using TOPEX altimeter measurements. The feasibility of applying retracking has also been examined. Specifically, the water level variation over the swamp forest along the Atchafalaya River basin has been examined with the SRTM DEM elevation and L-band Advanced Land Observing Satellite (ALOS) Synthetic Aperture Radar (SAR) imagery. It has been found that the water level fluctuations in terms of amplitude of each 10-Hz TOPEX time series becomes larger as the elevation decreases and the SAR backscattered power increases. Over the Amundsen Sea sector, which suffers dynamic thinning due to the recent acceleration of coastal glaciers, the 18-Hz stackfile has been built using Envisat retracked measurements. The rates of ice sheet elevation changes have been estimated over 1˚ × 1˚ regions with 1-km resolution Antarctic DEM which is used to correct for the surface gradient error. The ice mass loss from September 2002 – May 2005 has been estimated to be -49 ± 5 Gigaton/year after correcting for the firn depth changes, which correspond to equivalent sea level change of 0.14 ± 0.01 mm/year.

PREFACE

This research is partially supported by grants from NOAA/NEDIS NA06NES400007, NASA Earth Science program: NNX08AT52G, NNG04GN19G, NNG04GN19G, JPL 1265252, 1283220, NSF's CMG Program (EAR0327633, and OCE-0620885), Hydrology Program (EAR-044007), and by NGA NURI Program HM1582-07-1-2024.

ACKNOWLEDGMENTS

I wish to express my sincere gratitude to my adviser Dr. C. K. Shum for his professional guidance, encouragement, and support during my graduate studies.

My gratitude and appreciation also go to my dissertation committee, Profs. Doug Alsdorf, Michael Bevis, and Patrick Wu for their fruitful advice and comments during the reviews of this manuscript.

I am also indebted to Dr. Yuchan Yi for helpful discussions during my graduate studies. I appreciate his valuable discussion and help on satellite radar altimeter processing.

I also thank my colleagues, Chung-Yen Kuo and Yiqun Chen for their practical help and discussion, and Wouter van der Wal and Justin Shum for their valuable suggestion and correction of the manuscript.

Finally, special thanks go to my wife, Mi-Young Moon and my son, Hahn-Bin. Without their dedication and patience, I would have not been able to accomplish this work.

TABLE OF CONTENTS

CHAPTER 1

INTRODUCTION

1.1 Satellite Radar Altimetry

Satellite radar altimetry is a revolutionary technology to measure the height and the shape of the sea surface globally from space. It has been used to observe global oceanic topography and its changes with unprecedented accuracy (several cm root-mean-square (RMS) in sea surface heights (SSH)) and resolutions (up to 50 km spatial scale and weekly temporal sampling) (Chelton et al., 2001; Shum et al., 2003). The observation principle of satellite altimetry is conceptually straightforward. It transmits an electromagnetic pulse to the sea surface and measures its two-way travel time when the return reflected from the instantaneous sea surface is received. The altimeter-observed time delay (t) can be converted to the range R from the satellite to the ocean surface as:

$$R = \frac{ct}{2} \tag{1.1}$$

where c is the free-space speed of light.

This instantaneous range measurement must be corrected for the instrument (e.g., oscillator drift, Doppler shift, range acceleration), the atmospheric propagation (e.g., wet and dry troposphere, ionosphere), and geophysical surface height variations (e.g., ocean tide, solid Earth tide, pole tide). With a precise orbital height (H) from the satellite to a reference ellipsoid, a sea surface height (h_{ssh}) relative to the specific reference ellipsoid can be computed as:

$$h_{ssh} = H - h_{alt} \tag{1.2}$$

where h_{alt} is the range after all of the corrections applied.

The altimeter measures the range using an on-board tracker which provides a time series of the received power distribution of the reflected pulses, which is called the

altimeter waveform. Figure 1.1 shows a schematic description of a pulse-limited radar altimeter obtained from a diffuse, horizontal and planar sea surface. The pulse-limited radar altimeter transmits a spherically expanding pulse of duration τ (for TOPEX/POSEIDON, 3.125 nsec), and thus the pulse width is $c\tau$, where c is the speed of light. When the leading edge of the pulse arrives at the sea surface at nadir $(t = t_0)$, the spherically expanding pulse starts to illuminate the sea surface at nadir, and the reflected signal begins to return to the altimeter. At a two-way travel time $t_0 < t < t_1$, the leading

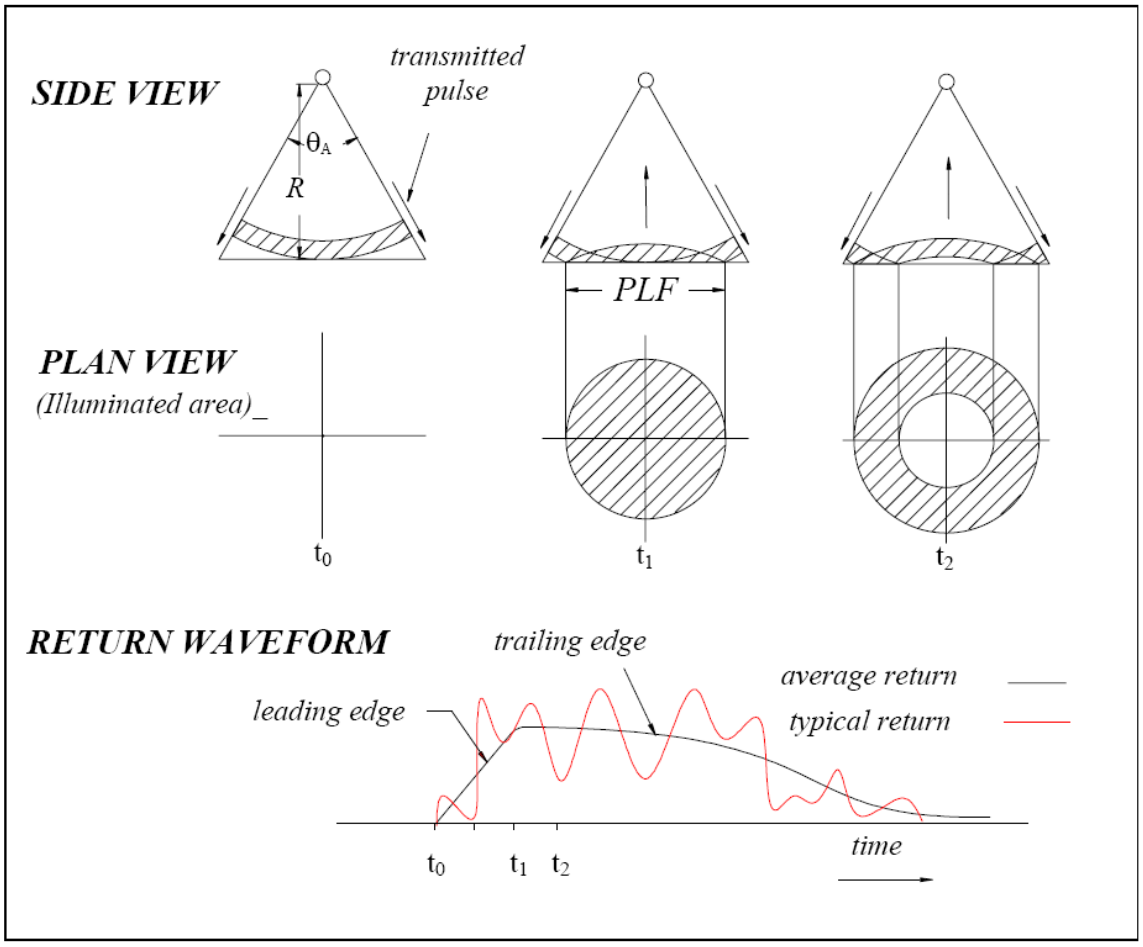

Figure 1.1: Interaction of a pulse and the scattering surface, and the developed returned waveform. PLF is the pulse-limited footprint, and θ_A is the antenna beam width [after Deng (2003)].

edge of the pulse continues to illuminate the planar sea surface further from the nadir point. Therefore, the illuminated area, which contributes to the radar return becomes an

expanding circle until the trailing edge of the pulse reaches the sea surface $(t = t_1)$. At this time, the backscattered energy to the altimeter reaches its maximum. Thereafter $(t > t_1)$, the footprint (or the illuminated area) becomes an annuls and the returned signal at the altimeter starts to decay due to the finite antenna beam width. Therefore, typical ocean waveforms have a rapidly rising leading edge and a slowly decaying trailing edge.

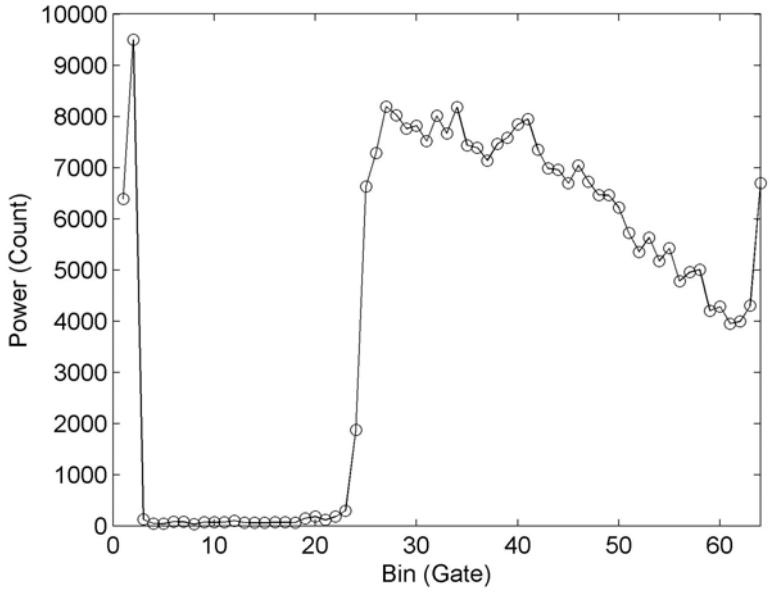

Figure 1.2: Example of TOPEX averaged return waveform over deep ocean.

Figure 1.2 shows an example of a TOPEX 64-sample waveform obtained over deep oceans. This waveform is obtained by averaging 480 successive returned pulses over a "track interval" spanning about 100 msec, which correspond to the interval of ten-per-frame (or 10 Hz) range measurements to reduce the "Rayleigh fading" of the radar signal (Chelton et al., 2001). The waveform obtained on-board has 128 samples, uniformly spaced at 3.125 nsec, which is combined (averaged) into the 64 samples and placed into the telemetry to the ground (Hayne et al., 1994).

The two-way travel time is defined as:

$$t_{1/2} \equiv \frac{t_0 + t_1}{2} = \frac{2R}{c} + \frac{\tau}{2} \tag{1.3}$$

The two-way travel time thus represents the time for the midpoint of the pulse to return from sea surface at nadir. Therefore, the altimeter determines the two-way travel time by identifying the half-power point on the leading edge of the waveform. Due to the inherent noise in the waveform as shown above, the on-board tracker is designed, based on a Brown (1977) model of the return waveform, to align the return spectral waveform so that the half-power point of the leading edge is at a specified frequency f_0. This tracking point corresponds to the gate 32.5 for 128-sample waveform or 24.5 for 64-sample waveform of TOPEX. The on-board tracker determines the offset between the half-power point on the leading edge of the waveform and the tracking point and realigns subsequent waveforms with the half-power point at the frequency f_0 (Chelton et al., 2001). This frequency shift corresponds to the two-way travel time from the altimeter to mean sea surface at satellite nadir.

The Brown model (1977) is the physical basis of the ocean waveform which is represented by the convolution of the instrument point target response (PTR), the flat surface response (FSR) and the probability density function of the specular points (particles on the surface which reflects the radar signal) (Brown, 1977; Hayne, 1980; Rodriguez, 1988) (see Chapter 2.3.1 for more details). Under the assumption that the distribution of the specular points is Gaussian, two-way travel time corresponds to the half-power point of the leading edge. However, this assumption is a primary limitation of the on-board tracker because the actual distribution of the specular points is skewed Gaussian. These effects may be corrected for in ground-based post processing, either by analyzing the waveform data, or by use of the look-up table correction (Chelton et al., 1989).

1.2 Applications of Altimeter Measurements over Non-Ocean Surfaces

Although satellite radar altimetry was initially designed for oceanographic applications such as sea level change, ocean circulation, and ocean tides, it has been demonstrated to be applicable to non-ocean surfaces as well. However, the performance of the radar altimeter over varying terrain differs significantly from that over ocean surface, and may lead the altimeter's on-board tracker to fail in precisely predicting the range. Therefore, the altimeter range measurements over non-ocean surfaces must be corrected for the deviation of the mid-point of the leading edge from the tracking gate of the onboard tracker (for TOPEX 64-sample waveform, 24.5). This procedure is known as retracking. It has been shown that radar altimetry is capable of measuring surface elevations and changes over ice sheets, including Antarctica and Greenland, and subsequently the ice sheet mass balance and its role in global sea level change (Zwally et al., 1989; Wingham et al., 1998; Davis et al., 2005). Furthermore, through the analysis of radar waveforms, the profile of backscattered power and the geophysical information related to the near-surface properties of the ice sheet such as the extinction coefficient (power lost from the incident energy due to scattering and absorption) can be derived

(Davis and Zwally, 1993). In addition, satellite radar altimetry has been used to measure inland water level variation for hydrologic studies (Birkett, 1998; Birkett et al., 2002; Frappart et al., 2006). Whereas these studies focused on large river basins such as the Amazon, attempts have been made to measure water level change over vegetated wetlands using TOPEX radar altimetry. Several studies (Brooks et al., 1997; Deng et al., 2002; Deng and Featherstone, 2006; Hwang et al., 2006) have also been conducted to improve the SSH estimates in coastal regions where altimetry-derived SSH are likely in error due to the complex nature of the return waveform from rapidly varying coastal topographic surfaces (Deng, 2003).

1.2.1 Ice Sheet Elevation Changes

The range accuracy and range-tracking capability of the pulse-limited altimetry deteriorates as the slope increases and fluctuates due to surface undulations. However, the relative accuracy for elevation change is about 5-10 times better than the absolute accuracy (Zwally and Brenner, 2001). Previous studies measured a thickening or thinning of the ice sheet by calculating elevation changes at orbital crossovers to avoid the surface gradient problem which is due to the deviation of the actual satellite ground track from the nominal ground track defined using a reference orbit model (see Chapter 2.4 for more details). Increases in the elevation of the Greenland Ice Sheet using Geosat and Seasat altimeter data was first reported by Zwally et al. (1989). Wingham et al. (1988) estimated the thinning of Antarctic Ice Sheet interior to be 0.9 ± 0.5 cm year^{-1} between 1992-1996 using European Remote Sensing 1/2 (ERS-1/2) satellite altimeter crossover measurements. More recently, Davis et al. (2005) reported the thickening of the East Antarctic Ice Sheet based on ERS-1/2 decadal (1992-2003) satellite radar altimetry observations.

In January 2003, NASA's ICESat (Ice, Cloud and land Elevation Satellite) carrying the Geoscience Laser Altimeter System (GLAS) was launched. The mission's primary goal is to detect elevation changes in the Antarctic and Greenland polar ice sheets. Having successfully obtained measurements spanning nearly five years to date, accurate change detection is now feasible (Gunter et al., 2008).

The go-ahead to build and launch the CryoSat-2 mission came in February 2006 after the loss of the first CryoSat in October 2005 due to a launch failure. CryoSat-2 is expected to launch in March 2009. CryoSat-2 will carry an interferometric radar altimeter called SIRAL (Synthetic Aperture Radar Interferometric Radar Altimeter) (Wingham et al., 2006b). SIRAL (over ice sheets) will have high-resolution (40-m pixels) measurements and a delay-Doppler technology to minimize the effect of steep slopes.

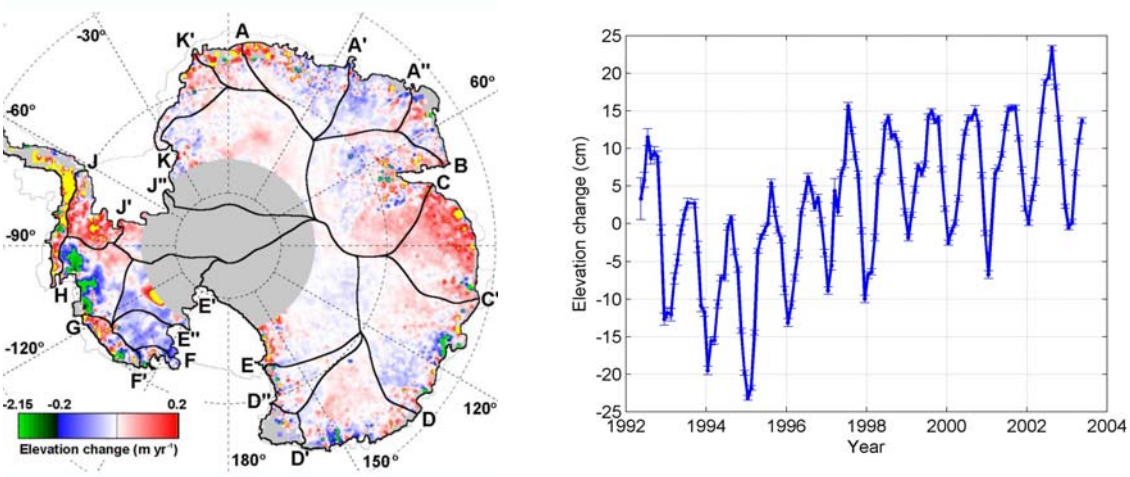

Figure 1.3: (Left) ERS-1/2 radar altimetry (1992–2003) determined Antarctic elevation change, *dH/dt* [after Wingham et al. (2006a)]. (Right) Elevation change time series from 1992 to 2003 for ~7.1 × 10^6 km^2 of the interior East Antarctic ice-sheet [Davis et al. (2005); data courtesy, C. Davis].

1.2.2 Digital Elevation Model Generation and Validation

Satellite altimetry has also been used for direct mapping of land topography. Although altimetry has collected radar echoes from land since the launch of Seasat and Geosat, the most useful dataset is that retrieved from ERS-1 Geodetic Mission. It provides dense spatial sampling with the capability to track over larger surface slopes at a reduced range resolution with a coarser ice mode. By combining these data with the best available ground truth, a global Digital Elevation Model (DEM), ACE has been created (Berry et al., 2000).

ERS-1 radar altimeter has also been used to validate regional DEM over Australia (Hilton et al., 2003) or global DEMs such as GLOBE_v1 and JGP95E (Berry et al., 2000). Recently, ERS-1 and Environmental Satellite (Envisat) radar altimeter data have been utilized to validate the 3 arc second Shuttle Radar Topography Mission (SRTM) DEM, and it has been shown that the global mean difference is 3 m with a standard deviation of 16 m (Berry et al., 2007).

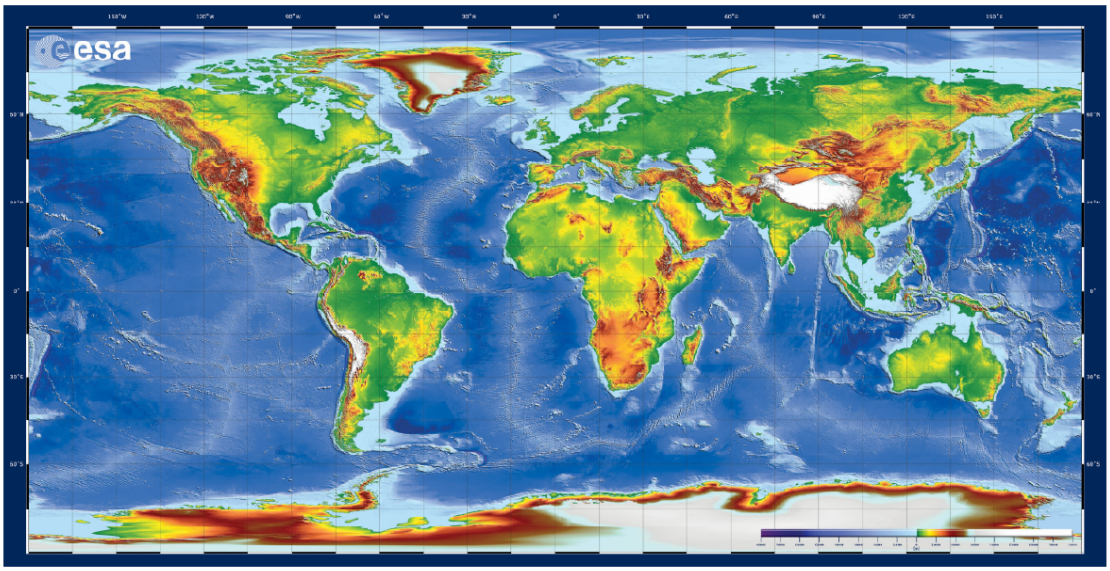

Figure 1.4: ACE (Altimeter Corrected Elevations) GDEM at 30-arcmin resolution. (http://www.cse.dmu.ac.uk/EAPRS/iag/ace.html)

1.2.3 Inland Water Level Monitoring

Over the past few years, satellite radar altimetry has been successfully used for inland water level monitoring. Initial work with Seasat altimeter showed that it maintained lock (i.e., obtained good surface height data) over 32% of the Earth's land surface, especially observed well over relatively flat wetlands (Rapley et al., 1987). It was followed by several studies using decadal (1992-2002) time series of inland water level from TOPEX measurements (Cazenave et al., 1997; Birkett, 1995; Kouraev et al., 2004). However, these studies directly used 10-Hz (i.e. ten-per-frame) high-rate range measurements contained in Geophysical Data Record (GDR) (Callahan, 1992). These measurements are obtained from the process which assumes that each waveform is an ocean-like return, which is based on the Brown model. Therefore, only large inland water bodies such as the Great Lakes (Morris and Gill, 1994; Birkett, 1995) or the largest rivers such as the Amazon and Congo (Birkett 1998; Birkett el al., 2002) have higher chances to be processed as ocean-like return. However, significant amount of data loss can occur during the periods of stage minima (lowest water level) due to the interruptions to the water surface by the surrounding topography. This limitation can be overcome by retracking individual return waveform (Berry et al., 2005; Frappart et al., 2006). The Envisat radar altimeter (RA-2) uses a dynamic mode-switching algorithm which enables collecting data over inland water in high-resolution mode instead of the ice mode implemented in ERS-1 and ERS-2 which sacrifices the vertical accuracy of measurement (Berry et al., 2005). The Envisat GDR contains 18-Hz retracked measurements, corresponding to a ground spacing of approximately 350 m, using four different

retrackers, which are OCEAN, ICE-1, ICE-2, and SEA ICE retrackers (Benveniste et al., 2002).

Figure 1.5 shows the Envisat 1-Hz nominal ground tracks (ascending pass 163 and descending pass 980; satellite groundtracks can be separated into ascending and descending passes which fly from south to north and from north to south, respectively) over Poyang Lake, which is the largest freshwater lake in China.. Retracked water level measurements along each of two Envisat passes using ICE-1 retracker (Bamber, 1994) are compared with *in situ* water level measurements in Figure 1.6.

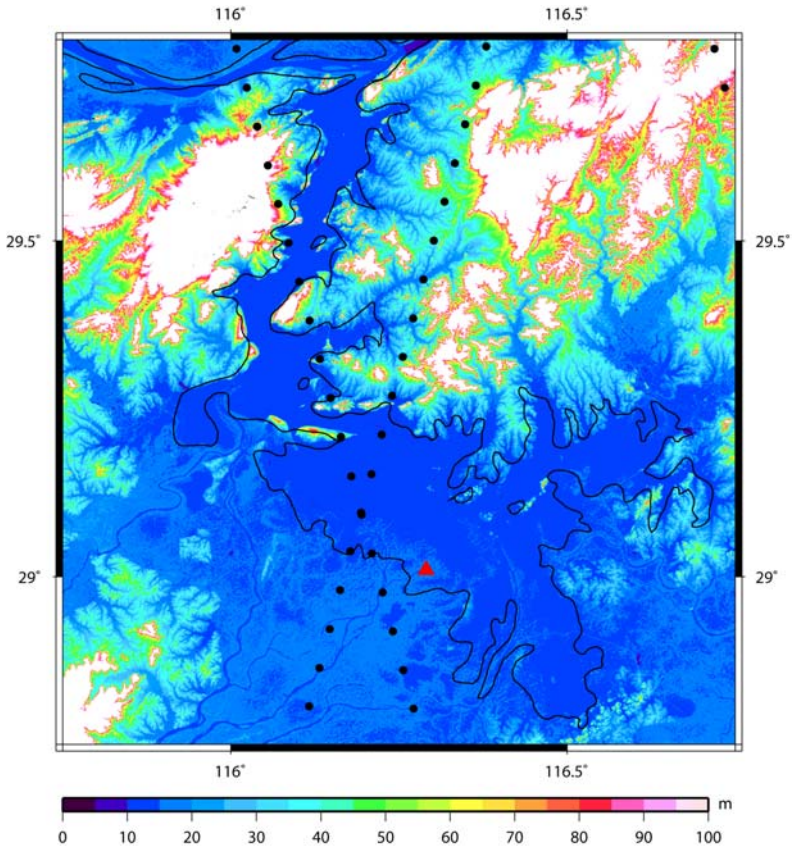

Figure 1.5: Envisat 1-Hz nominal tracks (black circles) with SRTM C-band DEM as background. The red triangle indicates the location of the water level gauge (or tide gauge) at Long Kou. Black lines show the lake boundary from the Generic Mapping Tool (GMT) of Wessel and Smith (2001).

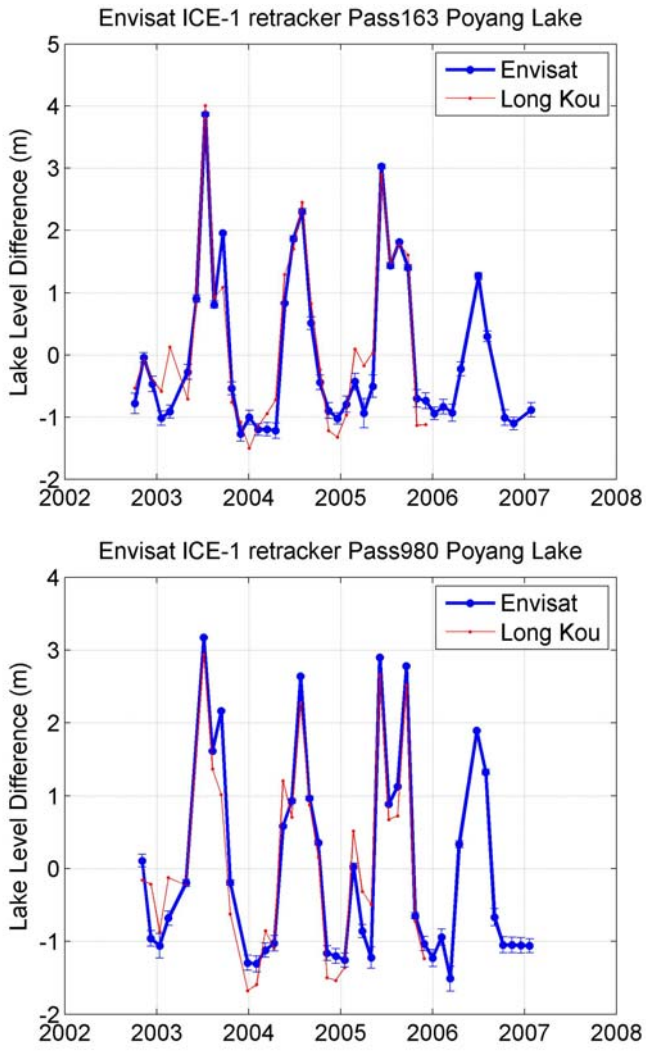

Figure 1.6: ICE-1 retracked lake level changes compared with *in situ* water level changes along Envisat pass 163 (top) and 980 (bottom).

1.2.4 Improving SSH in Coastal Regions

The SSH measurements from satellite radar altimetry in coastal region is hindered not only by less reliable geophysical and environmental corrections (Chelton et al., 2001), but also by the noisier radar returns from the generally rougher coastal sea states and simultaneous returns from reflective land and inland water (Brooks et al., 1997; Deng and Featherstone, 2006). Brooks et al. (1997) found that the land return influences TOPEX waveforms within distances of 4.1 – 34.8 km from coasts with the maximum near the East China Sea. Deng et al. (2002) observed that the waveforms from ERS-2 and TOPEX/POSEIDON (T/P) can be affected up to a maximum distance of 22 km off the

Australian coast. Waveforms reflected from these affected coastal oceans do not conform to those over open oceans so that the on-board satellite tracking algorithm cannot accurately compute the range between the satellite and nadir surface, thus producing the poorly estimated SSHs.

In recent years, the waveform retracking techniques have been developed and used to reprocess altimeter waveform data to improve these poorly estimated altimeter-derived SSHs in the well-known problematic coastal regions (e.g., Brooks et al., 1997; Anzenhofer et al., 1999; Deng and Featherstone, 2006; Hwang et al., 2006). Deng et al. (2001) studied the coastal region of the Taiwan Straits to determine how the gravity field could be improved by retracking the ERS-1 waveforms. The resulting retracked gravity anomalies compared to ship gravity data to within 9.92 mGal while the difference was 13.93 mGal before retracking.

Here, a T/P pass (ascending Pass 117 into the vicinity of Peveto Woods Sanctuaries, Louisiana) in the Gulf of Mexico for the potential to improve coastal sea surface height topography data has been examined.

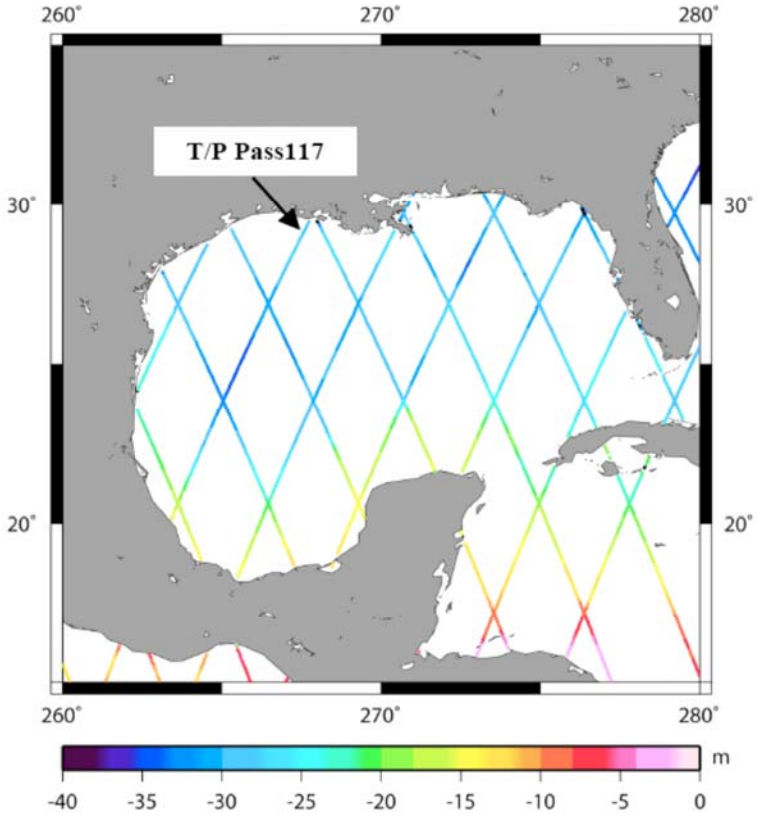

Figure 1.7: SSH with respect to a reference ellipsoid over the Gulf of Mexico from T/P cycle 328. T/P Pass 117 moves from water to land.

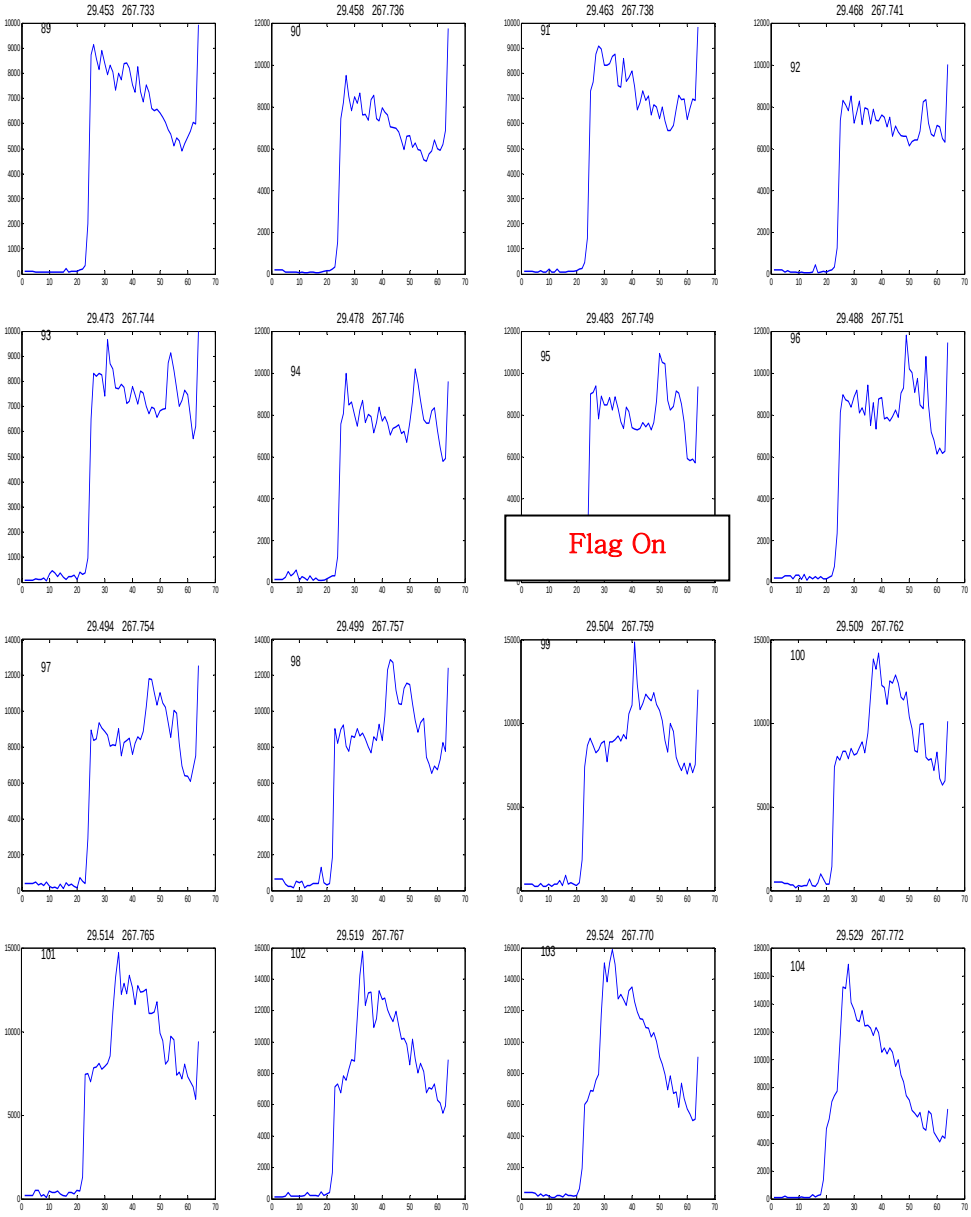

Figure 1.8: TOPEX waveform along Pass 117 (cycle 328) from water to land over the Gulf of Mexico. The x- and y-axis represent the waveform bin and returned power, respectively. The corresponding latitude and longitude are shown at the top of each waveform. The numbers at the upper left of each waveform represent the sequence of waveform along the pass. The waveforms from #95 to #104 are flagged by bit2 of the Alt_Bad1 in TOPEX GDR as 'bad' data.

The waveforms from #95 to #104 are flagged by bit2 of the Alt_Bad1 in TOPEX GDR as 'bad' data. The flag is set for an entire frame even though only a part of that frame's waveforms may have been corrupted by land return. Therefore, the measurements can be flagged at a distance beyond the presence of land returns in the waveforms (Brooks et al., 1997). It can be seen from Figure 1.8 that the waveforms from #95 to #102 are retrackable. They show the sea surface return around gates 21 through 23 while the land returns are dominant at the later gates of the waveform. Figure 1.9 shows the results of SSHs along Pass 117 estimated using three different retrackers which are the Offset Center Of Gravity (OCOG) (Bamber, 1994), 50% threshold retracker (Davis, 1997), and the modified 50% threshold retracker (Lee et al., 2008b), compared with the non-retracked SSH and the EGM96 geoid. The retracking algorithms are described in more detail in Chapter 2. As can be seen from Table 1.1, the modified 50% threshold retracker provided the best agreement with the geoid model.

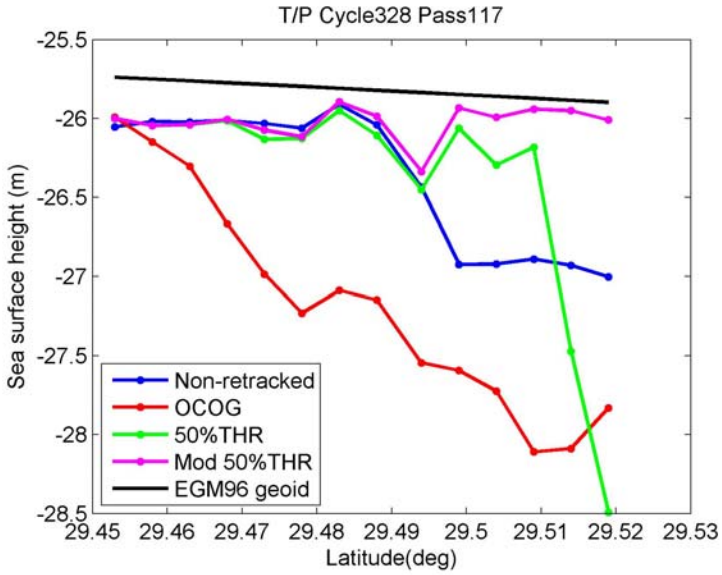

Figure 1.9: SSHs from different retrackers compared with EGM96 geoid.

Retracker	RMS difference (cm)
Non-retracked	68
OCOG	149
50% threshold	87
Modified 50% threshold	24

Table 1.1 Root-mean-square (RMS) differences between the SSHs and EGM96 geoid.

1.3 Motivation for This Study

The performance of the radar altimeter over land surfaces is significantly different from that over ocean surface primarily due to different surface roughness and elevation variability. Due to these limitations, previous applications of radar altimetry over land surfaces were limited to the generation of averaged height information or quality assessment of global or regional DEMs (Hilton et al., 20003; Berry et al., 2007), or classifying the land surface properties using backscattering coefficients obtained from satellite altimetry (Papa et al., 2002, 2003). Whereas the previous land altimetry studies focus on static height determination, there has been no prior attempt to map the temporal change of the land surface, due primarily to the inhomogeneous radar scatter due to different surface properties, as compared to the deep ocean. In addition, it may be also limited by another critical error caused by the deviation of the actual ground track from the nominal ground track, especially if the repeat-track analysis (or collinear analysis, using altimeter-derived surface heights obtained along identical ground tracks at different time) is to be used. This is the so-called surface gradient error. The generated time series of height changes from radar altimeter cannot represent the height change over the same geographic location without this correction because the actual track of each satellite pass can deviate ±1 km from the nominal ground track. Therefore, mainly crossover analysis has been used over ice sheets to circumvent this difficulty. In this dissertation, high-resolution DEMs are utilized to solve the surface gradient problem. Furthermore, the principles used to build the Ohio State University (OSU) 1-Hz stackfiles system (Yi, 2000), which is designed for deep ocean, is expanded toward regional 10-Hz TOPEX stackfiles over land surfaces. Decadal time series have been constructed and the observed vertical crustal motion, which is primarily due to Glacial Isostatic Adjustment (GIA) resulting from the viscoelastic rebound of the solid Earth in response to the deglaciation of the Laurentia ice-sheet since the Pleistocene ice age, can be potentially used for better constraining of Earth rheology and thus improving GIA models.

Interferometric synthetic aperture radar (InSAR) has been proven to be useful to measure centimeter-scale water level changes over Amazon flood plain (Alsdorf et al., 2000, 2001) and Everglades wetland (Wdowinski et al., 2004) using L-band SAR imagery. This is based on the fact that flooded forests permit double-bounce returns, which allow InSAR coherence to be maintained. Furthermore, ERS-1/2 C-band InSAR data have been used to demonstrate its feasibility to monitor water level changes over Louisiana wetlands (Lu et al., 2005). In addition, satellite radar altimetry has been used to measure inland water level variation over large river basins (Birkett, 1998; Birkett et al., 2002; Maheu et al., 2003; Frappart et al., 2006) as mentioned above. In this dissertation, decadal (1992-2002) TOPEX data has been used to measure water level fluctuations over Louisiana wetlands. Unlike the previous studies, which spatially average 10-Hz data (or 18-Hz for Envisat) over a distance corresponding to the intersection between the satellite ground track and water body, the 10-Hz regional stackfiles technique over Louisiana wetland is employed. As a result, for the first time, measuring water level change over each 10-Hz stackfile bin, which has along-track ground spacing of ~660 m, will take

place.

Satellite radar altimetry has been used to directly measure the ice sheet elevation changes (Zwally et al., 1989; Wingham et al., 1998; Davis et al., 2005; Helsen et al., 2008). The previous studies computed the ice sheet elevation changes (dH) at satellite crossover points in order to minimize the topographic induced errors, i.e., to circumvent the surface gradient problem. However, the crossover analysis limits the number of measurements. The collinear analysis can provide as many as 100 times more individual measurements over Antarctica, and enhance the spatial resolution to study local scale phenomena (Legresy et al., 2006). Furthermore, in case of European Space Agency (ESA) altimeters such as ERS-1/2 and Envisat which are equipped with linearly polarized antenna, a systematic difference as large as a few meters at crossover points exists (Wingham et al., 1998), which causes difficulties and limitations for the crossover analysis. Clearly, this complex and little understood error can be accounted for by employing the collinear analysis. Therefore, in this study, 18-Hz Envisat stackfile is developed to estimate the rate of the ice sheet elevation changes over the Amundsen Sea sector, West Antarctica, which is under dynamic thinning due to the recent acceleration of coastal glaciers.

In summary, this study developed the method to examine the application of satellite altimetry over non-ocean surfaces focusing on, for the first time, detecting temporal change of topographic surface and high-resolution monitoring of hydrologic change using collinear analysis.

1.4 Summary of Chapters

Chapter 2 reviews the basis of radar altimeter data processing over land surfaces including various retracking algorithms.

Chapter 3 deals with the estimation of the vertical crustal motion using TOPEX dual-frequency radar altimeter data. The procedure to construct the time series over each 10-Hz land stackfile bin is described along with an explanation about the 10-Hz land stackfiles and the surface gradient correction using C-band SRTM DEM. Furthermore, a modified threshold retracker is developed and used in this study. The resulting decadal vertical motion time series is compared with several contemporary GIA models, and GIA signals observed by GRACE spaceborne gravimetry mission.

Chapter 4 is devoted to monitoring Louisiana wetland water level over each of 10-Hz stackfiles bin with along-track spacing of ~660 meter using TOPEX satellite radar altimetry measurements. The feasibility of applying retracking by investigating the statistics of the estimated retracked gate positions is studied.

Chapter 5 examines the ice sheet elevation changes (September 2002 – May 2007) using 18-Hz Envisat stackfile technique over the Amundsen Sea sector, West Antarctica with 1-km resolution Antarctic DEM. The estimates ice mass loss is compared with previous altimeter results and GRACE-derive ice mass change.

Chapter 6 concludes with a recommendation on future studies.

CHAPTER 2

SATELLITE RADAR ALTIMETER DATA PROCESSING

2.1 TOPEX/POSEIDON and Envisat Altimeter Data

TOPEX/POSEIDON (T/P) carries the first dual-frequency (Ku- and C-band) radar altimeter space mission designed to accurately measure global ocean topography with an unprecedented accuracy. T/P satellite was launched on August 10, 1992, on a near-circular orbit repeating every 9.9 days. The orbit inclination is 66˚ that enables the global observation of the ocean within 66˚ latitude bounds. The POSEIDON altimeter, which shared the antenna on-board the satellite and was operated for about 10 percent of the mission time, is not used in this study. The TOPEX altimeter has redundant Sides A and B hardware. The signals from Side A altimeter began to show performance degradation in 1999, and it has been switched to Side B on 10 February 1999 (Hayne and Hancock, 2000). In December 2001, T/P and Jason-1 were placed in the same orbit forming a so-called tandem phase where they are separated by only about 70 seconds. The tandem phase lasted about 7 months and T/P has been moved to the orbit with the ground tracks in between its old ones on August 2002.

In this study, TOPEX GDRs and Sensor Data Records (SDRs) for cycle 9-364 and Envisat were used. The TOPEX GDRs and SDRs are available from the NASA/JPL Physical Oceanography Distributed Active Archive Center (PO.DAAC). The Ku-band 10-Hz range data contained in GDRs are utilized, and their 10-Hz geodetic coordinates per each cycle can be computed from the Precise Orbit Ephemeris (POE) data provided by NASA Goddard Space Flight Center (GSFC) (N. Zelensky, personal communication) using the 10-Hz time tags calculated from the 20-Hz range measurements contained in SDRs (see Appendix A). Detailed description of the SDR data records can be found in Algiers et al. (1993). The SDRs also contain 10-Hz 64-bin waveform measurements, which are used for retracking. The waveform anomalies such as zero-leakage and the offset leakage effects are mitigated by employing the sets of multiplicative and additive waveform factors (Hayne et al., 1994). These factors are originally developed for the TOPEX Side A altimeter, but also applicable to Side B (D. Hancock, personal communication, 2006). Geophysical corrections such as dry troposphere, solid Earth tide

and pole tide corrections have been applied using the values provided in the GDR. Although T/P is equipped with a three-channel (18, 23, and 37 GHz) microwave radiometer for measuring integrated water vapor contents, interpolated wet troposphere correction based on the European Center for Medium Range Weather Forecasting (ECMWF) atmospheric model is used in this study since the wet radiometric observations at these frequencies are overwhelmed by the opaqueness of the land surface, rendering them not usable. The ionosphere correction based on DORIS data is used instead of the dual-frequency ionosphere correction which is based on observing the range differences between the Ku- and C-band channels.

The Envisat RA-2 altimeter is designed to provide a global scale collection of radar echoes over ocean, land, and ice to measure ocean topography, water level variations over the large river basins, land surface elevation and to monitor sea ice and polar ice caps (Wehr and Attema, 2001; Frappart et al., 2006). RA-2 is also a dual-frequency radar altimeter: 13.575 GHz in Ku-band and 3.2 GHz in S-band. Specifically, four different retrackers are operationally applied to RA-2 raw data to provide accurate height estimates, which are included in Envisat RA-2 GDR. Each retracker has been developed for a specific radar return: one for ocean (OCEAN), two for ice sheets (ICE-1 and ICE-2), and one for sea ice (SEA ICE).

2.2 Convolution Models for Ocean Waveforms

The radar altimeter waveforms are the basic measurement for observing the Earth's surfaces. They provide the range between the satellite and the surface at nadir via two-way travel time of the transmitted pulse, the Significant Wave Height (SWH) via the slope of the waveform leading edge, and the backscattering coefficients which represent the surface roughness and characteristics via the returned power. The shape of the waveform from incoherent surface scattering has been based on physical optics theory, which treats the surface as a set of specular points with a given height and slope probability density distribution. The time series of the mean returned power, i.e., the waveform, $P(t)$, is represented by the convolution of the instrument point target response (PTR) $\chi(t)$, the impulse response from a smooth sphere (the mean Earth) $S(t)$, and the probability density function (PDF) of the specular points $f_{sp}(t)$ (Brown, 1977; Hayne, 1980; Barrick and Lipa, 1985; Rodriguez, 1988):

$$P(t) = S(t) \otimes \chi(t) \otimes f_{sp}(t) \tag{2.1}$$

The time t is the time measured at the satellite such that $t = 0$ corresponds to the first arrival time of an impulse from the mean ocean surface. To provide a simplified analytical expression, Brown (1977) proceeded with the assumptions that are inherent in the convolution model of near normal incidence rough surface backscatter. These assumptions are generally satisfied over ocean surface, but not for land scatter.

The radar impulse response from a smooth sphere is given by (Hayne, 1980; Barrick and Lipa, 1985; Rodriguez, 1988):

$$\begin{aligned} S(t) &= A\exp(-\alpha t) I_0\left(\beta t^{1/2}\right) U(t) \\ \alpha &= \frac{\ln 4}{\sin^2(\theta/2)} \frac{c}{h} \frac{1}{1+h/R} \cos(2\xi) \\ \beta &= \frac{\ln 4}{\sin^2(\theta/2)} \left[\frac{c}{h} \frac{1}{(1+h/R)}\right]^{1/2} \sin(2\xi) \end{aligned} \tag{2.2}$$

with:

A : scaling constant;

I_0 : modified Bessel function of the second kind;

$U(t)$: unit step function;

h : altimeter height above the mean ocean surface;

R : radius of the Earth;

c : speed of light;

θ : antenna half-power beamwidth (≈ 0.38˚ for T/P);

ξ : off-nadir pointing angle.

The derivation of Equation (2.2) assumes that the antenna gain can be approximated by a Gaussian and includes effects due to the Earth's curvature.

The specular point PDF in spatial domain can be expressed as (Rodriguez, 1988):

$$f_{sp}(z) = \frac{1}{(2\pi)^{1/2}\sigma}\exp\left(-\eta^2/2\right)\left[1+\frac{\lambda}{6}\left(\eta^3-3\eta\right)\right]$$
$$\eta = \frac{z - z_T}{\sigma} \qquad (2.3)$$

with:

continued

Equation (2.3) continued

σ : ocean surface standard deviation;

λ : ocean surface skewness;

z : height above mean ocean surface ($z = 0$);

z_T : tracker bias, which represents the altimeter height estimation error.

The radar system PTR is primarily the transmitted radar pulse shape. For an idealized, linear, frequency-modulated altimeter radar pulse, the radar system PTR is given by (Ulaby et al., 1982; Rodriguez, 1988):

$$\chi(t) \sim \frac{\sin^2\left[(at/2)(T-|t|)\right]}{(at/2)^2} \qquad -T \le t \le T \qquad (2.4)$$

where $2T$ is the radar pulse length and a is a constant which depends on the radar bandwidth.

Figure 2.1 shows the PTR using TOPEX bandwidth $B = 320\,\text{MHz}$, the surface impulse response using TOPEX orbit configurations, the specular point PDF using parameters $z_T = 0, \sigma = 1m, \lambda = 0.4$, and the convolved power which is computed using the convolution theorem.

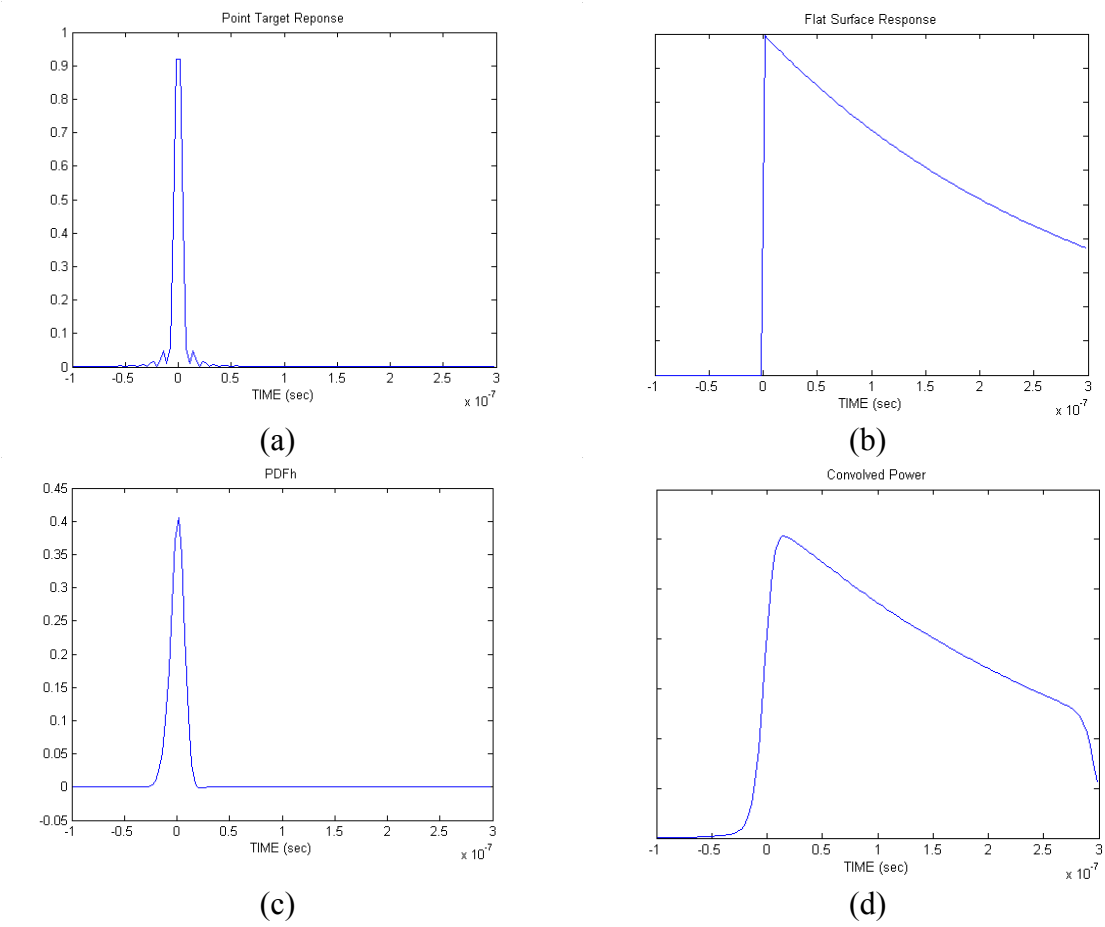

Figure 2.1: Example of (a) PTR, (b) surface impulse response, (c) specular point PDF ($z_T = 0, \sigma = 1m, \lambda = 0.4$), and (d) convolved power using TOPEX specifications.

2.3 Waveform Retracking Methods

2.3.1 Ocean Waveform Retracking – Deconvolution Method

Over ocean surfaces, altimeter retracking algorithms aim to retrieve more accurate estimates of the range and the SWH, as well as additional parameters such as the antenna off-nadir angle and the skewness of the surface elevation distribution. Ocean waveform retracking is based upon the convolution representation of the waveform. Therefore, one can recover the specular point PDF by performing a deconvolution of the return radar waveform (Barrick and Lipa, 1985; Rodriguez and Chapman, 1989). Due to the fact that the specular point PDF is a function of the SWH, the ocean surface skewness, and the

altimeter tracker error, one can estimate these parameters by performing a functional fit to the deconvolved PDF (Rodriguez and Chapman, 1989). Equation (2.1) can be expressed as a matrix equation $y = Mx$, where M is $S(t) \otimes \chi(t)$ and x is $f_{sp}(t)$. However, this equation is effectively singular, and Rodriguez and Chapman (1989) suggested a modified convolution model, which is called the "corrected slopes convolution model". It starts with a simpler $S(t)$ where the Bessel function $I_0\left(\beta t^{1/2}\right)$ is replaced by $\exp\left(\beta^2 t/4\right)$ such as:

$$S(t) = A\exp\left[-\left(\alpha - \frac{\beta^2}{4}\right)t\right]U(t) \tag{2.5}$$

Then, the derivative of the return power can be expressed as:

$$\begin{aligned} P'(t) &= \left[\chi(t) \otimes f_{sp}(t)\right] \otimes S'(t) \\ &= \left[\chi(t) \otimes f_{sp}(t)\right] \otimes \left[A\delta(t) - \left(\alpha - \frac{\beta^2}{4}\right)S(t)\right] \\ &= A\left[\chi(t) \otimes f_{sp}(t)\right] - \left(\alpha - \frac{\beta^2}{4}\right)P(t) \end{aligned} \tag{2.6}$$

$$\Rightarrow$$

$$\chi(t) \otimes f_{sp}(t) = \frac{1}{A}\left[P'(t) + \left(\alpha - \frac{\beta^2}{4}\right)P(t)\right]$$

where $\delta(t)$ is a Dirac delta function.

After approximation of the convolution integral using numerical quadrature rule, the specular point PDF can be solved by least squares algorithm.

$$x = \left[M^T M\right]^{-1} M^T y \tag{2.7}$$

Due to the fact that this equation is unstable, i.e., sensitive to noise, Twomey's regularization method (1962) for solving Equation (2.6), which is Fredholm integral equation of the first kind, is used. Once the deconvolved PDF is obtained, the unknown parameters z_T, λ, σ and A are solved by linearizing the specular PDF (Lipa and Barrick, 1981; Rodriguez 1988) or applying the more robust Levenberg-Marquardt method (Rodriguez and Chapman, 1989).

2.3.2 NASA V4 (β-) Retracker

The β-retracker is the first retracking algorithm developed to obtain corrected ranges from SEASAT-1 radar altimeter over the Antarctic and Greenland continental ice sheets (Martin et al., 1983). This algorithm uses 5- or 9-parameter functions to fit a single- or double-ramped waveform, respectively. The double-ramped waveforms can be found when two distinct surfaces at different elevations exist within the range window. The Ice Altimetry Group of NASA's Goddard Space Flight Center (GSFC) has developed algorithms for retracking polar ice altimetry based on Martin's functions. There have been four versions of the GSFC retracking algorithms (Zwally, 1996), and Version 4 employs an exponential function instead of a linear function to fit a fast-decaying trailing edge which is caused by the beam attenuation over sea ice or ice sheets:

$$y(t) = \beta_1 + \beta_2 e^{-\beta_5 Q} P\left(\frac{t-\beta_3}{\beta_4}\right) \tag{2.8}$$

where

$$Q = \begin{cases} 0 & \text{if } t < \beta_3 - 2\beta_4 \\ t - (\beta_3 - 2\beta_4) & \text{if } t \geq \beta_3 - 2\beta_4 \end{cases}$$

$$P(z) = \frac{1}{\sqrt{2\pi}} \int_{-\infty}^{z} e^{-\frac{q^2}{2}} dq \quad \text{with } q = \frac{t-\beta_3}{\beta_4}$$

The unknown parameters are as follows:

- β_1 : the thermal noise (or DC level) of the waveform.
- β_2 : waveform amplitude.
- β_3 : mid-point of the leading edge which marks the correct time delay.
- β_4 : slope of the leading edge which is related to SWH.
- β_5 : slope of the trailing edge which is related to the scattering at the footprint.

The range correction from the retracking algorithm is obtained by the difference between the estimated mid-point of the leading edge and the on-board tracking gate (23.5 for TOPEX, 32.5 for ERS-1/2) multiplied by the distance which is related to a single gate such as:

$$\Delta R = (\beta_3 - \text{tracking gate}) \times \Delta s \tag{2.9}$$

where

$$\Delta s = \tau \times c / 2 = 0.4684 \ m$$

where τ is pulse width (3.125 nsec for TOPEX) and c is speed of light.

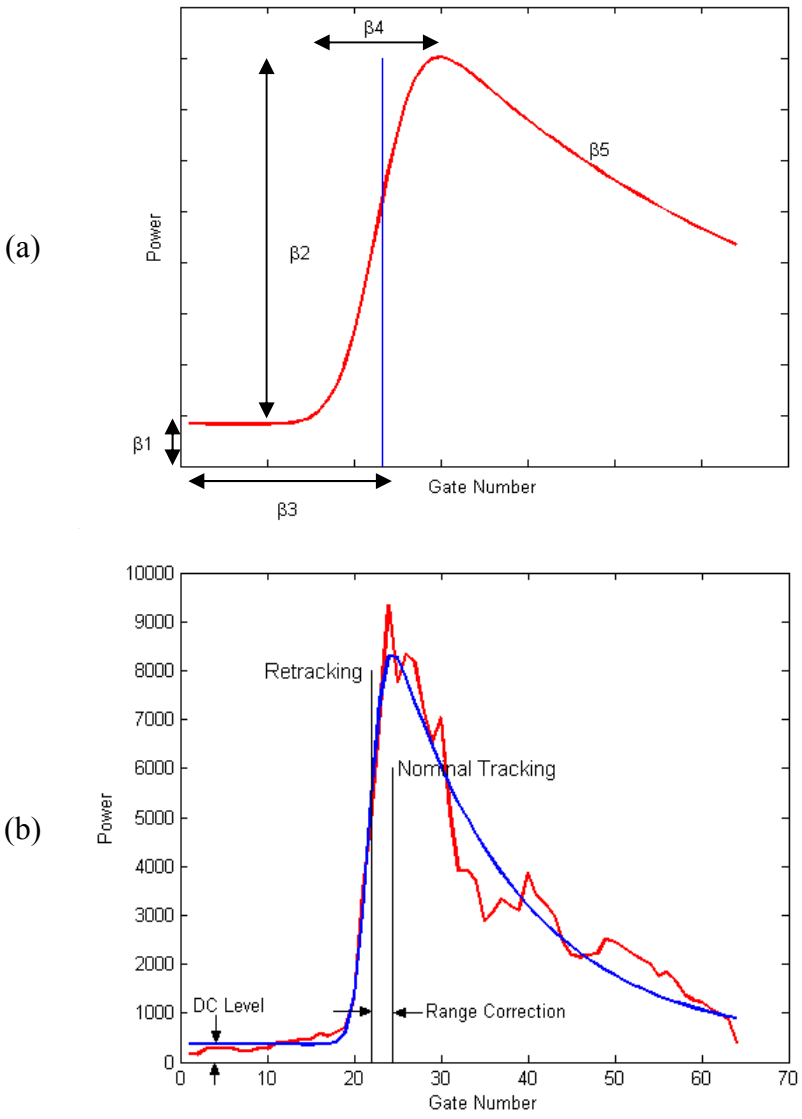

Figure 2.2: (a) 5-parameter retracker model, (b) An example of a land-returned waveform and the fitted 5-parameter single ramp function.

It should be noted that the on-board 128-sample TOPEX waveform, which has uniform gate interval of 3.125 nsec with its tracking point at sample (or gate) 32.5, is averaged in multiples of 1, 2, and 4 to form the 64-sample telemetry waveform which is summarized in Table 2.1. Waveform samples 17-48 in 128-sample waveform are not combined (averaged) to preserve the original sampling rate (3.125 nsec) across the leading edge of the waveform. Therefore, Equation (2.9) is valid when the retracked gate lies between 9 and 40.

128-sample waveform	64-sample waveform		sampling rate
1-16	1-8	averaged by two	6.25 nsec
17-48	9-40	one to one match	3.125 nsec
49-64	41-48	averaged by two	6.25 nsec
65-128	49-64	averaged by four	12.5 nsec

Table 2.1 TOPEX telemetry sample to waveform sample relationship (Hayne et al., 1994).

As mentioned above, some of the waveforms obtained from ice sheets may include the second ramp due to a distinct height change within the footprint, which can be fitted by 9-parameter model:

$$y = \beta_1 + \beta_2(1+\beta_9 Q_1)P\left(\frac{t-\beta_3}{\beta_4}\right) + \beta_5 e^{-\beta_8 Q_2} P\left(\frac{t-\beta_6}{\beta_7}\right) \tag{2.10}$$

where

$$Q_1 = \begin{cases} 0 & for\ t < \beta_3 + .5\beta_4 \\ t-(\beta_3 + .5\beta_4) & for\ t \geq \beta_3 + .5\beta_4 \end{cases}$$

$$Q_2 = \begin{cases} 0 & for\ t < \beta_6 + .5\beta_7 \\ t-(\beta_6 + .5\beta_7) & for\ t \geq \beta_6 + .5\beta_7 \end{cases}$$

$$P(z) = \int_{-\infty}^{z} \frac{1}{\sqrt{2\pi}} e^{(-q^2/2)} dq$$

As a result, there are two corrections each representing an independent range from the satellite to the surface such as (Martin et al., 1983):

$$\begin{aligned} \Delta R_1 &= (\beta_3 - tracking\ gate)\times \Delta s \\ \Delta R_2 &= (\beta_6 - tracking\ gate)\times \Delta s \end{aligned} \tag{2.11}$$

where β_3 and β_6 are the locations of the center of the first and second ramps, respectively.

The retracked gates are then

$$\begin{aligned} R_1 &= R_{observed} + \Delta R_1 \\ R_2 &= R_{observed} + \Delta R_2 \end{aligned} \tag{2.12}$$

(a)

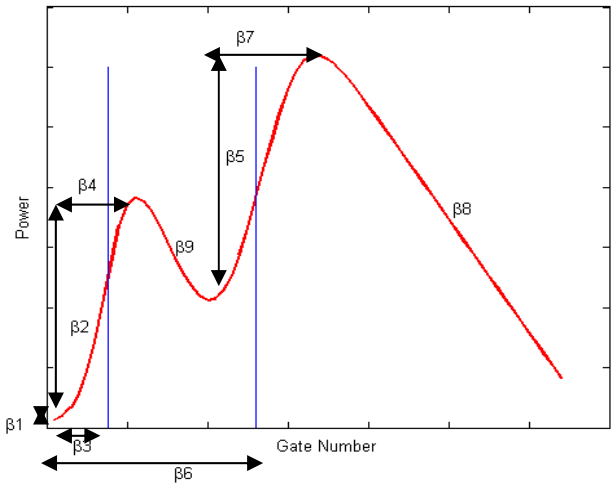

(b)

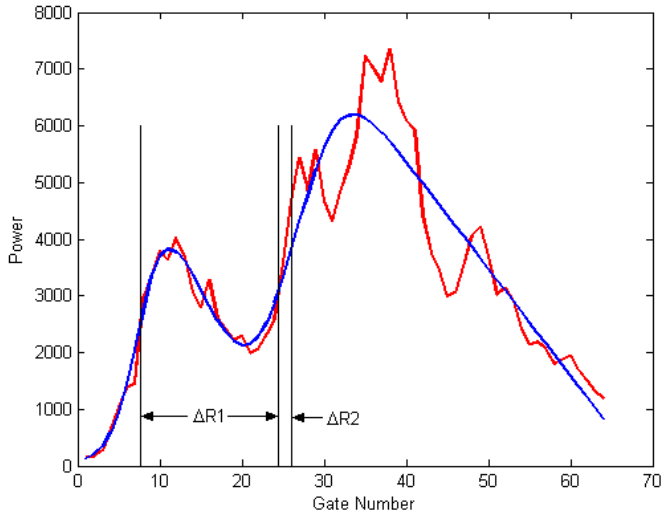

Figure 2.3: (a) 9-parameter retracker model, (b) example of a double-ramp waveform and the fitted 9-parameter waveform model.

2.3.3 Offset Center of Gravity (OCOG) Retracker

The OCOG algorithm was developed as an empirical technique to produce ice sheet data products from ERS-1/2 radar altimetry. It estimates an amplitude of the wavefrom and uses this to threshold retrack the leading edge (Bamber, 1994). It calculates the center of gravity of a rectangular box and the amplitude is twice the height of the center of gravity. The squares of the sample values are used to reduce the effect of low amplitude samples in front of the leading edge.

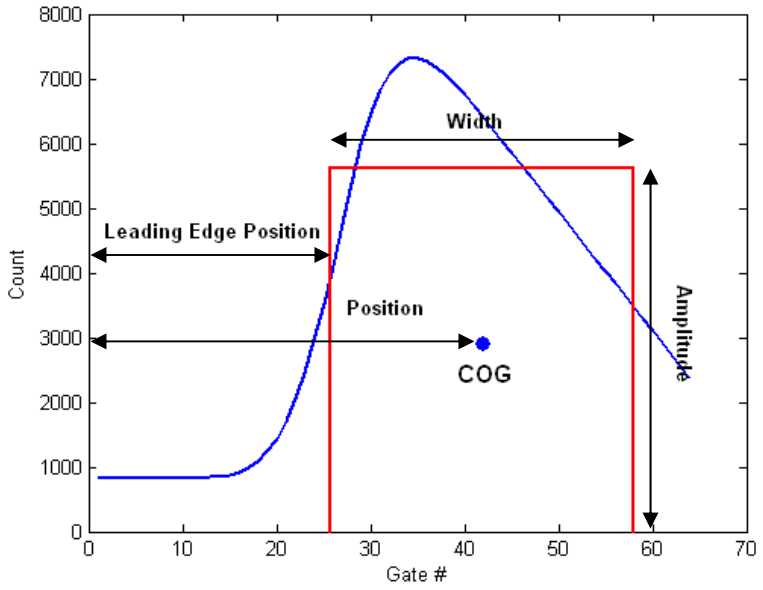

Figure 2.4: Schematic description of the OCOG retracker.

$$
\begin{aligned}
COG &= \sum_{i=1+n_a}^{64-n_a} iP^2(i) \Big/ \sum_{i=1+n_a}^{64-n_a} P^2(i) \\
Amplitude &= \sqrt{\sum_{i=1+n_a}^{64-n_a} P^4(i) \Big/ \sum_{i=1+n_a}^{64-n_a} P^2(i)} \\
Width &= \left(\sum_{i=1+n_a}^{64-n_a} P^2(i) \right)^2 \Big/ \sum_{i=1+n_a}^{64-n_a} P^4(i)
\end{aligned}
\tag{2.13}
$$

where $P(i)$ is the waveform sample value at the i^{th} bin, and n_a is the number of aliased sample ($n_a = 4$ for TOPEX). In addition, the waveform samples 45-50 are excluded to avoid the leakage effects of TOPEX waveforms (Hayne et al., 1994).

Finally, the leading edge position (LEP) is given by,

$$
LEP = COG - Width/2 \tag{2.14}
$$

2.3.4 Threshold Retracker

The threshold retracking algorithm was developed primarily to measure ice sheet elevation change (Davis, 1997). The leading edge position is determined by locating the

first waveform sample to exceed the percentage (i.e., threshold level) of the maximum waveform sample amplitude. The pre-leading edge DC level (or thermal noise) is computed by averaging the waveform sample 5 to 7, and again, the samples from 1 to 4, 45 to 50, and 61 to 64 are excluded for TOPEX Ku-band waveform. Davis (1997) suggests the 50% threshold for surface-scattering dominated waveforms, and 10% or 20% threshold level for volume-scattering surface.

$$\begin{aligned} A_{\max} &= \max\left(P(i)\right) \\ DC &= \frac{1}{3}\sum_{i=5}^{7} P(i) \\ TL &= DC + T_{coeff}\left(A_{\max} - DC\right) \end{aligned} \tag{2.15}$$

with:

$A_{\max}$: maximum waveform amplitude;

DC : thermal noise or DC level;

T_{coeff} : threshold level;

TL : retracked gate.

2.4 Surface Gradient Error

One issue that must be considered is the effect of the surface gradient in generating a time series of the surface height differences from the repeat-orbit altimeter data as the horizontal location of each observation point changes from cycle to cycle. If we select relatively flat land surfaces (standard deviation of the height variation < 40 cm) around land regions near Hudson Bay as in Lee et al. (2008a), we can model the surface as a plane and the surface gradient can be computed from the satellite observations, i.e., the retracked surface heights. The detailed gradient estimation algorithm can be found in Guman (1997). It should be emphasized that this approach is valid only over reasonably flat surfaces. The local mean land surface in a study region (say, bin) can be modeled with along- and cross-track gradients as:

$$LSH = a + b \cdot dx + c \cdot dy \tag{2.16}$$

with:

LSH : mean land surface height;

a : height of the plane at the bin center;

b : along-track land surface gradient;

c : cross-track land surface gradient;

dx : along-track displacement of a data point from the bin center;

dy : cross-track displacement of a data point from the bin center.

The parameters a, b and c can be estimated by the least squares adjustment. However, in addition to the spatial variation, the land surface height may also exhibit temporal changes from cycle to cycle. Thus, a model with six parameters that includes linear, annual, and semi-annual variations is adopted:

$$LSH = A + B \cdot (t - t_0) + c1 \cdot \cos[\omega(t - t_0)] + s1 \cdot \sin[\omega(t - t_0)] + c2 \cdot \cos[2\omega(t - t_0)] + s2 \cdot \sin[2\omega(t - t_0)] \quad (2.17)$$

with:

A : offset or bias;

B : linear slope;

$c1, c2$: amplitudes of the cosine term;

$s1, s2$: amplitudes of the sine term;

ω : annual frequency.

To reduce the effect of the terrain surface gradient on the estimate of the annual/semi-annual variations, Equations (2.16) and (2.17) are implemented in an iterative scheme. First, a preliminary annual/semi-annual variability is estimated using Equation (2.17), and then the preliminary land surface gradient using the annual/semi-annual variation-removed surface height is estimated. This procedure is iterated to yield a gradient-corrected surface height. However, this approach would be no longer available over rougher surfaces, and the surface gradient correction employed in this study using a high-resolution DEM will be presented in Chapter 3.5.

CHAPTER 3

LAURENTIA VERTICAL MOTION OBSERVATION

3.1 Introduction

The viscoelastic solid Earth response that is referred to as the Post-Glacial Rebound (PGR) or the Glacial Isostatic Adjustment (GIA) process, originates from the deglaciation of the large ice sheets culminated during the Pleistocene Ice Age, 18,000 to 25,000 years before present (ka BP). When the load of the ice sheets with 2–3 km thickness was removed during deglaciation, the solid Earth is responding as a viscoelastic body, primarily in the Earth's mantle, producing vertical and horizontal deformations and corresponding gravity changes towards isostatic equilibrium (e.g., Peltier, 1994). The GIA process is an ongoing global process, taking place at the location of past (Fennoscandia, Laurentia and possibly other) and current (Antarctica, Greenland, Patagonia) ice sheets and globally, well outside these areas. Modeling of the GIA process strongly depends on knowledge of the viscosity of the Earth's upper and lower mantle, lithospheric thickness, ice sheet thickness and its time-varying extent, Earth rotational feedback, ocean-ice/land boundary, and other geophysical parameters. The non-uniqueness and regional dependence of the problem leads to large uncertainty in the current GIA models. Conventional GIA models (e.g., Mitrovica et al., 1994a) are based on radially symmetric viscoelastic, spherical, self-gravitating, Maxwell Earth model with an arbitrary surface load coupled with the sea-level equation (Farell and Clarke, 1976) which can include Earth rotational feedback and realistic ocean-land boundaries (e.g. Johnston, 1993; Milne et al., 1999). Recent models use the finite-element approach to simulate a 3-D spherical self-gravitating Earth model, to consider laterally varying viscosity profiles and lithospheric thickness (Wu and van der Wal, 2003, Wu, 2004; Paulson et al., 2005; Latychev et al., 2005a, 2005b) .

Measurements of relative sea level change for the last century and present-day have relied on long-term records global tide gauges attached to fixed points on the Earth's crust (Douglas, 2001). At present, the only means to obtain accurate estimates of global sea level rise from tide gauges is to add the solid Earth vertical motion to the tide gauge record, which is indistinguishable from sea level change, using a robust GIA model (Mitrovica et al. 2001; Lambeck et al. 2002), or to correct the vertical motion with data

from co-located geodetic sensors such as GPS. Since not all the world's tide gauges are co-located with continuous and long-term GPS, the correction of tide gauge vertical motions still mainly relies on robust GIA models. Present GIA models predict global deformation patterns, but are inadequate for regional studies due primarily to poor understanding of the complex relationship between Earth rheology and Late Pleistocene ice sheet history. Uncertainties in GIA parameters further affect the accurate determination of ice sheet mass balance (Wahr et al., 2000). In particular, in addition to the perhaps inadequate data span, local tectonics and hydrologic effects, lack of knowledge in GIA process is most probably the largest error source in GRACE data processing to definitively observe Greenland and Antarctic ice sheet mass balance (Velicogna and Wahr, 2006a, 2006b).

The Post Glacial Rebound (PGR) over North America due to the glaciation/deglaciation cycles of the ancient Laurentide ice sheet has been studied recently by Dyke and Peltier (2000), Mitrovica et al. (2000) and Peltier (2002). The Laurentide ice sheet reached its maximum extent during the late Wisconsian, 19-22 ka BP, which is defined as the Last Glacial Maximum (LGM), with an average of 21 ka BP (Dyke et al., 2002). The last deglaciation ended ~6 ka BP and the Laurentide ice volume of 16–37 $\times$ 10^6 km^3, equivalent to 40–92 m of sea level rise, has been released to the ocean (Licciardi et al., 1998). It was the largest ice sheet during the LGM and had a strong impact on sea level and climate change. Dyke et al. (2002) provided a comprehensive review of the evolution of the Laurentide ice sheet. The Great Lakes are located at the former southern margin of the Laurentide ice sheet, near the so-called transition zone. The vertical crustal velocity in this region is more sensitive to the viscosity structure in the upper mantle, while the velocity in the center of the rebound or in the far-field is more sensitive to the viscosity in the lower mantle (Mitrovica et al., 1994a, Braun et al., 2008). The transition zone is the region at the Earth's surface close to the former ice sheet margin. It is characterized by a transition from continuous uplift near the center of rebound to continuous subsidence farther away. The differences in sensitivity between the transition zone and the center of the former Laurentide ice sheet indicate the importance of constraints over the entire region, not only from the source of the rebound, to provide more constraints of the GIA process.

GIA can be detected by several types of measurements, which are briefly discussed in the following. The relative vertical motion of the solid Earth's surface can be determined by means of historic sea level data (Larsen et al., 2003) and precise leveling (Mäkinen and Saaranen, 1998). The mass change that accompanies the uplift can be observed by means of absolute gravimeters (Lambert et al., 2001), relative gravity measurements (Pagiatakis et al., 2003), whereas that geocentric vertical and horizontal motion can be measured by Global Positioning System (GPS), and a combination of tide gauges and altimetry (Nerem and Mitchum, 2002; Kuo et al., 2004). Recently, 3-D crustal motion in Fennoscandia from the BIFROST GPS project (Milne et al., 2001; Johansson et al., 2002; Lidberg et al., 2007) and Laurentia (Calais et al., 2006; Sella et al., 2007) has been determined from continuous GPS observations. However, the spatial coverage of present-day GPS data over North America is still too sparse to resolve the uncertainties associated with the ice load history (Sella et al., 2007).

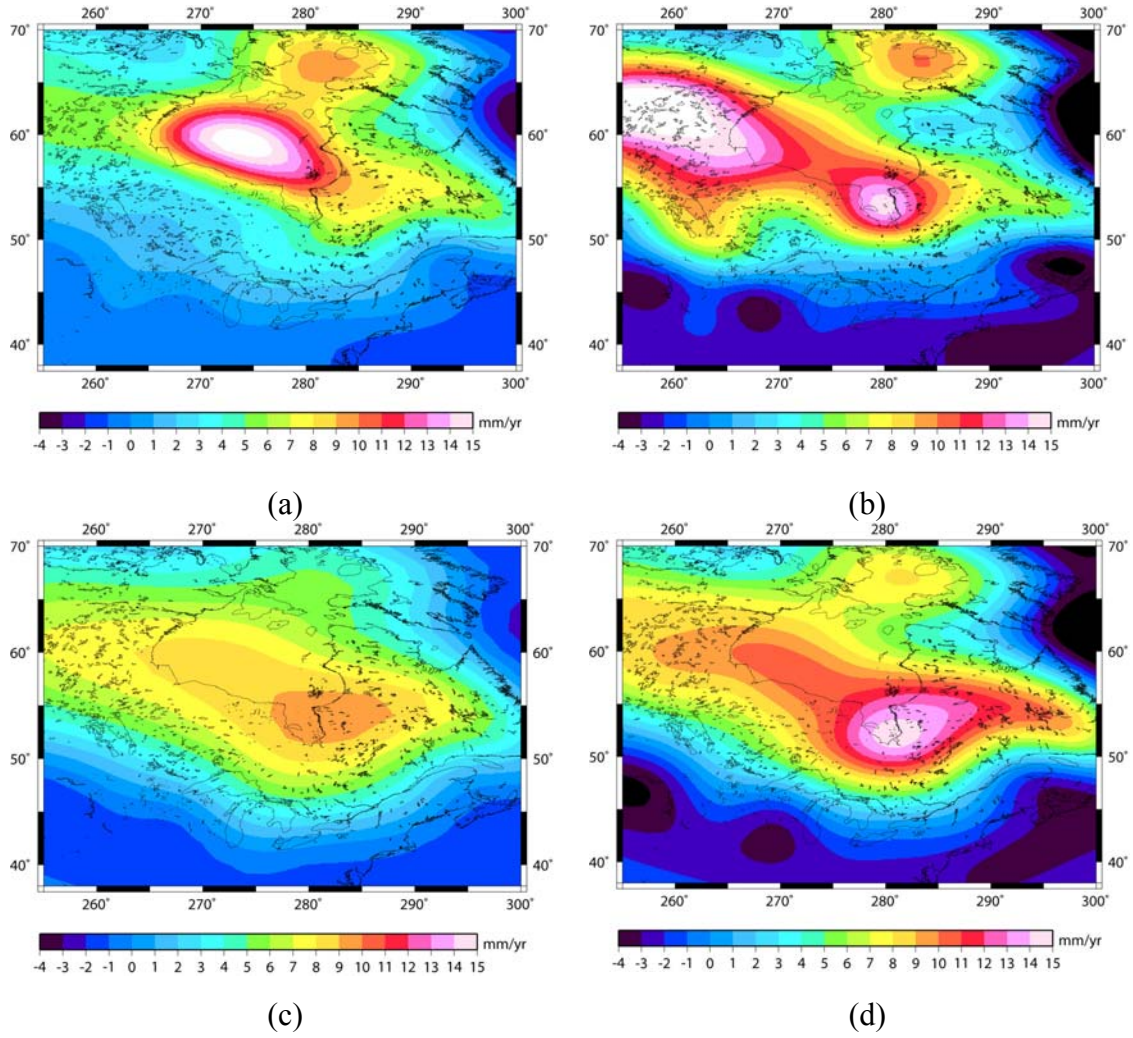

Figure 3.1: Predicted the present-day crustal vertical motion over Laurentia predicted by (a) ICE-4G (VM2) model (Peltier, 2002), (b) ICE-5G (VM2) model (Peltier, 2004), (c) RF3S20 $(\beta = 0.4)$ model (Wang et al., 2008) (d) the simple three-layer viscous model, used in BIFROST GPS/GIA study (Milne et al., 2001), with lithosphere thickness (LT) = 120 km, lower mantle viscosity (LMV) = 1×10^{21} Pa·s, upper mantle viscosity (UMV) = 3×10^{21} Pa·s.

A novel technique which combines the long-term (>40 years) tide gauge records and decadal TOPEX/POSEIDON altimetry in a network adjustment technique to estimate vertical motion at tide gauge locations has been demonstrated for the semi-enclosed Baltic sea (Kuo et al., 2004) and in the Great Lakes and elsewhere (Kuo et al., 2008; Braun et al, 2008). Recently, monthly geopotential spherical harmonic coefficients from GRACE gravimetry mission (Tapley et al., 2004) provided another observation of the GIA process with spatial resolution longer than 600 km half-wavelength. Tamisiea et al. (2007) estimated the GIA contribution to the static gravity field over Laurentia, and van

der Wal et al. (2008) investigated the limitation of GRACE data to constrain GIA in Laurentia by considering various effects including filtering of GRACE signal and leakage from water storage variations and present-day ice melt in Alaska and Greenland. It should be noted that all these measurements could measure more than the GIA signal. These other signals include crustal motion resulting from land subsidence, tectonics or mantle dynamics, atmospheric, ocean, hydrologic or snow loading, and other geophysical and anthropogenic processes.

Relative sea level change data is widely used to constrain GIA models (e.g., Tushingham and Peltier, 1991), but they are mostly located at the coast, and sometimes far from the former center of the former ice sheet. In this Chapter, the objective is to generate additional and accurate measurements of vertical crustal deformation from TOPEX radar altimetry over Laurentia land surfaces to help constrain the GIA process. Once the technique is demonstrated in this region the procedure can potentially be applied to other regions of the world that experience vertical uplift of the same magnitude due to GIA or other geodynamic processes (see Chapter 5).

(a)

(b)

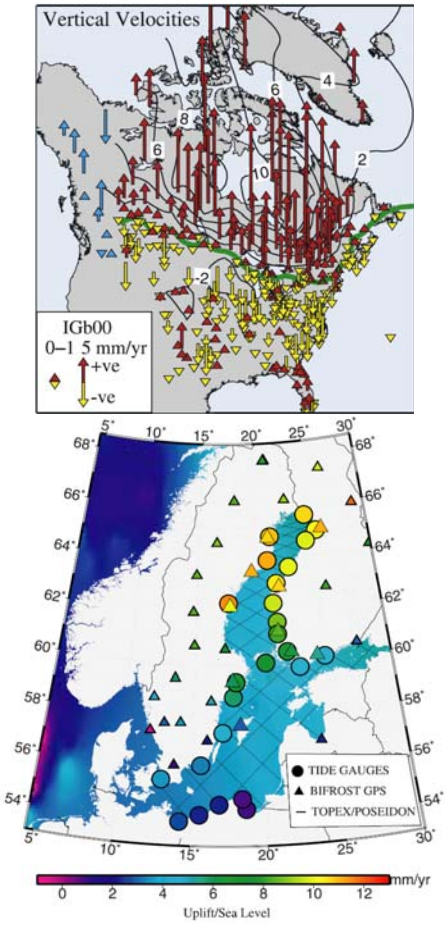

Figure 3.2: (a) Vertical GPS site motions (after Sella et al., 2007, Fig. 1) (b) estimates of absolute vertical motion (circles) at 25 tide gauge locations compared with 10 collocated BIFROST GPS vertical rates (triangles) (after Kuo et al., 2004, Fig. 1).

3.2 10-Hz Land Stackfile

The altimeter stackfile, a database structure, was first developed at the University of Texas at Austin, Center for Space Research (CSR) to efficiently store and access the massive spaceborne radar altimetry measurements over global ocean (Sandwell and Zhang, 1989; Shum et al., 1990). The stackfile can be viewed as a three-dimensional array. The three-dimensional parameters represent (1) the distance from the equator along an orbit (row number); (2) the specific orbit of a repeat cycle (column number, or an equator-crossing longitude); and (3) the repeat cycle. Data are stored into bins, whose along-track dimension approximately corresponds to 1 second of time along the satellite ground tracks. The distance of a bin is approximately 7.5 km because the spacecraft speed is approximately 7.5 km/sec. A bin contains all the information from various repeat cycles measured over a particular area of the Earth projected underneath the satellite groundtrack. The bins are addressed with row and column indices. Each column corresponds to a particular pass or orbit, and each row corresponds to a particular latitude value. More detailed information about the stackfile can be found in Kruizinga (1997). It should be noted that this original stackfile stores the 1-Hz range measurements in the bin even though the GDRs also contain 10-Hz ranage measurements.

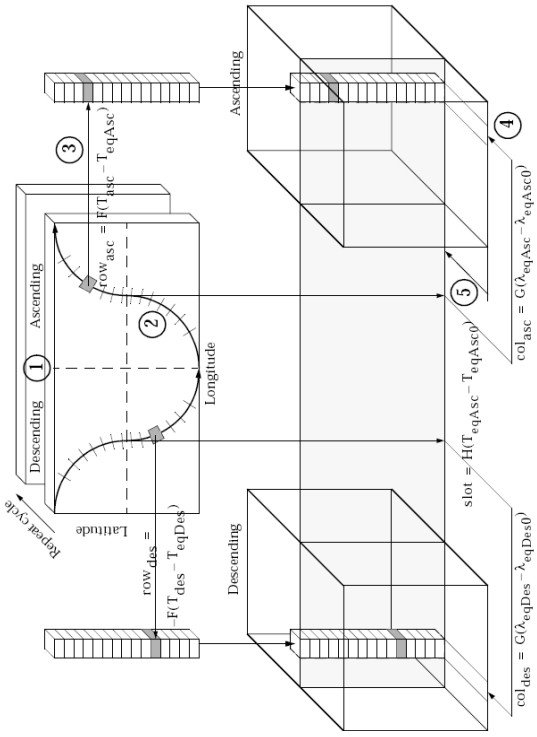

Figure 3.3: Conceptual illustration of altimeter stackfile database structure and its associated mapping (after Kruizinga, 1997).

In this study, 10-Hz regional land stackfile is developed by expanding the concept of the conventional 1-Hz ocean stackfile and applied to the land surfaces around Hudson Bay including northern Ontario, northeastern Manitoba and near the Great Lakes. The 10-Hz stackfile plays an important role in this study since each 10-Hz stackfile bin can serve as a nominal ground track point which the generated TOPEX time series refer to. Furthermore, the gradient corrections are computed using the actual and nominal 10-Hz ground track coordinates which refer to the same 10-Hz stackfile bin. Here, the TOPEX 10-Hz regional stackfile over Hudson Bay land surfaces is operated by an on-the-fly procedure instead of storing the data on each stackfile bin as the conventional 1-Hz ocean stackfile does. First, the skeleton of 1-Hz regional stackfile over Hudson Bay land surface is built based on the OSU stackfile software (Yi, 2000). In other words, an empty three-dimensional array is constructed, and each bin in the array can be assigned to a particular cycle, pass, and record of TOPEX GDRs (and SDRs) to perform the collinear analysis. For each GDR record from a given TOPEX cycle and pass, the corresponding row is predicted based on an equator crossing table which is computed by interpolating the precision orbit ephemeris (POE) of TOPEX. The equator crossing tables are the basis of mapping transformation between time tags in GDR record and row-column addresses of the 1-Hz stackfile bins as shown in Figure 3.3 (Kruizinga, 1997). If the predicted 1-Hz stackfile row-column address is equivalent to the given bin address of the empty stackfile array, then for each 1-Hz stackfile bin, 10-Hz stackfile bins (or 10-Hz nominal ground tracks), in which the surface heights are "stacked", are created. The latitudes of the 10-Hz bins are calculated by linearly interpolating two adjacent 1-Hz nominal ground track latitudes, which are stored in the OSU stackfile bin header, with respect to the corresponding 10-Hz time tags (or time at equator crossing). The 10-Hz time tags are calculated from the 1-Hz time tags as follows:

$$\begin{aligned} t_1^k &= \left(t_1 - \text{Dtim\_Mil} + 2(k-1)\cdot \text{Dtim\_Pac} + 0.5\cdot \text{Dtim\_Pac}\right)(\mu\text{sec}) \quad \text{k} = 6,7,\cdots,10 \\ t_2^k &= \left(t_2 - \text{Dtim\_Mil} + 2(k-1)\cdot \text{Dtim\_Pac} + 0.5\cdot \text{Dtim\_Pac}\right)(\mu\text{sec}) \quad \text{k} = 1,2,\cdots,5 \end{aligned} \tag{3.1}$$

where t_1, t_2 identify 1-Hz time tags of an arbitrary frame (say, frame 1) and the frame next to it (frame 2); t_1^k, t_2^k are 10-Hz time tags of the second half of frame 1 and the first half of frame 2; Dtim_Mil represents the time shift from the first 20-Hz (20-per-frame) height in a science data frame to the middle of the frame, and Dtim_Pac is the elapsed time between the 20-Hz ranges.

Dtim_Mil and Dtim_Pac, which increase as the absolute value of latitude increases, are provided in the GDR for each frame, and a 1st order polynomial is fitted to estimate the nominal value to be used. It should also be noted that for a prograde orbit, TOPEX has increasing time spacing between 1-Hz time tags as the latitude increases, and thus 1-Hz time tags are computed from a 10th order polynomial as a function of "row" of the stackfile. On the other hand, due to the fact that the satellite velocity in the longitude direction is nearly constant, 10-Hz nominal ground track longitudes λ_1^k and λ_2^k can be calculated using the nominal 1-Hz ground track longitudes, λ_1 and λ_2, using Equation

(3.2) which is based on the fact that the middle of the altimeter frame is located between the 10th and 11th 20-Hz measurements (or 5th and 6th 10-Hz measurements) as shown in Figure 3.4.

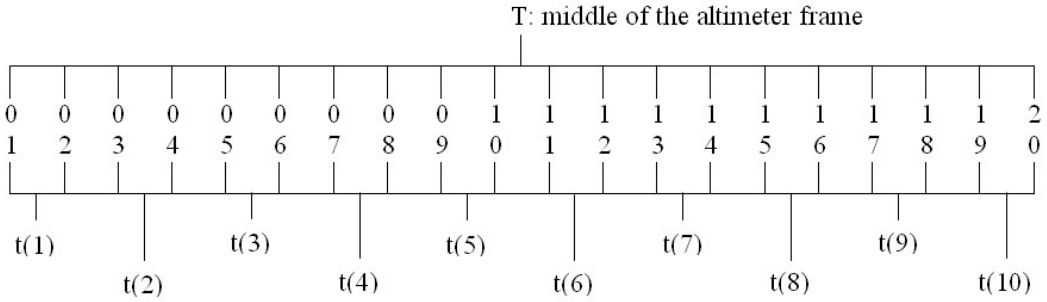

Figure 3.4: TOPEX altimeter frame with locations of the 20-per-frame and 10-per-frame measurements (averages of the 20-per-frame measurements). The location of the altimeter mid-frame is also shown.

$$\lambda_1^k = \lambda_1 + \frac{\lambda_2 - \lambda_1}{20} \times (2k - 11) \quad k = 6,7,\cdots,10$$
$$\lambda_2^k = \lambda_1 + \frac{\lambda_2 - \lambda_1}{20} \times (2k + 9) \quad k = 1,2,\cdots,5 \qquad (3.2)$$

where λ_1, λ_2 are the longitudes of the first and second 1-Hz stackfile bin; λ_1^k, λ_2^k are the longitudes of the10-Hz stackfile bins.

Next, each of 10-Hz range measurements contained in TOPEX GDRs can be assigned to each corresponding 10-Hz stackfile bin. The 10-Hz range measurements can be further corrected by applying retracking corrections using the waveform data contained in TOPEX SDRs. Finally, the time series of land surface height changes can be constructed over each 10-Hz stackfile bin or more than one 10-Hz stackfile bin by spatially averaging them. Figure 3.5 shows a diagram for the 10-Hz stackfile procedure used in this study. Furthermore, not only 10-Hz range measurements but also any 10-Hz observations such as Automatic Gain Control (AGC) or pulse peakiness (see Chapter 4.2) can be processed together.

Additionally, 90-m resolution C-band Shuttle Radar Topography Mission (SRTM) DEM, which meets a vertical accuracy of 16 m absolute error and 6 m relative error (Rabus et al, 2003), is selected to be a reference surface to choose an optimal retracker (Chapter 3.3) and to calculate land surface height anomaly (Chapter 3.4). Furthermore, it

is used to correct along- and cross-track land surface gradients caused by the satellite orbital drift (±1 km at equator) in the exact-repeat orbits (Chapter 3.4). Since the SRTM mission took place in February 2000, the influence of vegetation/forest canopies on the elevation should be minimal in the northern hemisphere study region (Bhang et al., 2007). The SRTM DEM is represented as orthometric heights with respect to the WGS-84 (or ITRF96) reference system and the EGM-96 geoid model (complete to degree or n_{max}=360). Hence, they have to be converted to ellipsoidal heights by adding geoid undulation from the EGM-96 model to be consistent with radar altimetry land surface height processing. Furthermore, due to the different semi-major axis of the WGS-84 ellipsoid and the TOPEX/POSEIDON ellipsoid, 70 cm difference are added to the ellipsoid heights with respect to the WGS-84 reference system. On the other hand, since the spatial coverage of SRTM DEM is from 55° S to 60° N, TOPEX data beyond the boundary of the SRTM DEM are excluded.

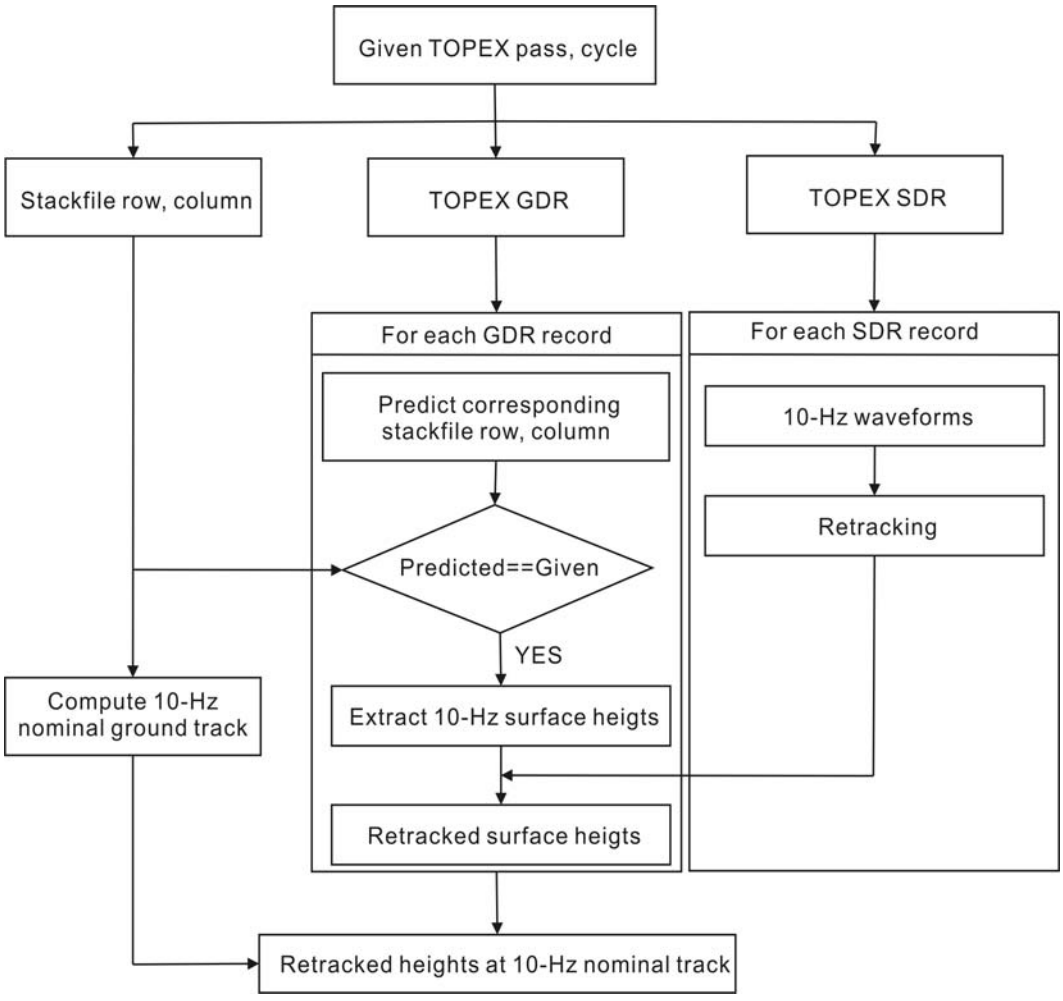

Figure 3.5: Flowchart for the TOPEX 10-Hz stackfile procedure.

3.3 Modified Threshold Retracker

In this study, several retracking algorithms including β-retracker (Martin et al., 1983), OCOG retracker (Bamber, 1994), and the 10%, 20%, and 50% threshold retracker (Davis, 1997) are evaluated to identify the optimal retracker. The threshold retracker estimates the noise level (or DC level) using the first few un-aliased waveform samples (see Chapter 2.3.2), and this may lead to erroneous results in the case of land waveforms since the pre-leading edge bumps might occur. Furthermore, the threshold retracker uses the maximum value of the waveform which may also lead to erroneous results because the maximum value of the waveform may not coincide with the maximum value of the leading edge in case of land waveforms, which consequently prevents the accurate estimation of the retracking gate. Here, an alternative method (hereinafter, modified threshold retracker) is developed to estimate the noise level and the maximum value of the leading edge of the land waveforms. First, two kinds of differenced waveforms are calculated. One is formed by taking the difference between two successive waveform samples (denoted by *difference I*), and the other by taking the difference between every other waveform sample (denoted by *difference II*). The noise level is selected to be the sample value of the first gate whose *difference I* value is negative and then becomes positive at the next gate. In this way, the pre-leading edge bumps can be avoided. To calculate the maximum value of the leading edge, first, the gate whose *difference II* value is the maximum is searched, which indicates the location of the apparent leading edge. From that gate, the first gate location, say *n*, whose *difference II* value becomes negative is searched. If *difference I* at gate *n* is also negative, then the waveform amplitude at gate *n* will be the maximum value of the leading edge. If *difference I* is positive at gate *n*, then the amplitude at *n+1* gate will be the maximum value of the leading edge. Finally, the retracking gate is estimated by the same method as the original threshold retracker. Figure 3.6 (a) shows an example of the land waveforms obtained over our study region. It is shown that the pre-leading edge bump in the waveform should have the least effect on the noise level computed by our alternative method. Moreover, it is apparent that the maximum value of the waveform occurs at gate 39, which is not the location of the maximum of the leading edge. The retracking gate obtained from original and modified 10% threshold retracker is shown as red solid and dashed lines, respectively in Figure 3.6 (a). The original 10% threshold retracker yields the retracking gate near the location of the pre-leading edge bump whereas the retracking gate from modified 10% threshold retracker selects the first return of the waveform above the pre-leading edge noise level (Davis, 1997).

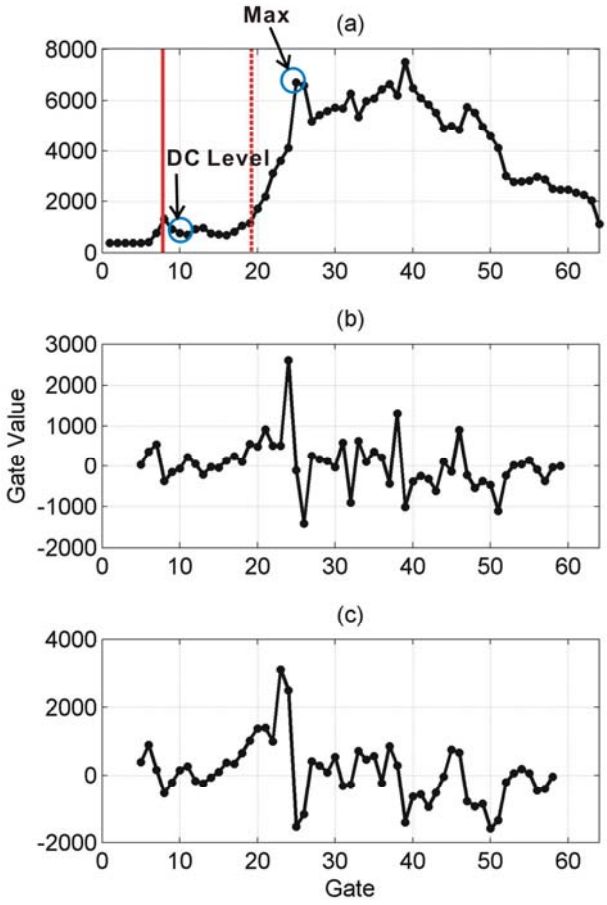

Figure 3.6: (a) Example of a land waveform near Hudson Bay. The red solid line indicates the retracking gate from original 10% threshold retracker and red dashed line shows the retracking gate from modified 10% threshold retracker. The pre-leading edge DC level and the maximum value of the leading edge obtained via modified 10% threshold retracker are indicated. (b) Differenced waveform by taking the difference between two successive waveform samples (*difference I*). (c) Differenced waveform by taking the difference between every other waveform sample (*difference II*).

To test and determine which retracking algorithm is optimal for each TOPEX pass, the 90-m resolution C-band SRTM DEM is used to compute the standard deviation of the difference between the retracked 10-Hz TOPEX surface height and the bilinearly interpolated SRTM elevation (converted to be referenced to the TOPEX/POSEIDON ellipsoid) at the 10-Hz TOPEX ground track coordinates. Since the SRTM mission took place in February 2000, TOPEX data from cycle 272 (starts on 1 February, 2000) was selected to be compared to minimize the possible seasonal height differences between them. The optimal retracker, which yields the minimum standard deviation of the

difference, is chosen for each altimeter pass, and the results are shown in Table 3.1, where the total number of waveforms to be retracked, the number of successfully retracked waveforms, the ratio between these two numbers, and the standard deviation of the differences between retracked altimeter surface heights and SRTM heights for each retracker are listed. Besides, the reduced variance after retracking is also calculated. It should be noted that the standard deviation and the reduced variance are calculated using the same number of processed waveforms per each pass. Here, the retracking is considered to be successful if the estimated retracked gate lies inside the Automatic Gain Control (AGC) gate (9 to 40 for 64-sample TOPEX waveform). This "AGC gate" consists of the average of 16 waveform samples on each side of the tracking point, and it is relatively insensitive to noise in the waveform and to misalignment of the waveform (Chelton et al., 2001). While OCOG retracker provides the smallest standard deviation of the difference for passes 126, 43, 67 and 143, all other passes show that modified 10% threshold retracker is the best choice. The modified 20% and 50% threshold retrackers are also tested, but not included in the Table as they provided worse agreement with the SRTM heights. Due to the fact that the original and modified threshold retrackers differ only in estimating the noise level and the maximum value of the waveform, this result, in terms of the threshold level, agrees with Davis (1997), who concluded that 10% threshold level produced the most repeatable ice-sheet surface elevations in terms of standard deviation from crossover analysis using Seasat and Geosat altimetry data. This result could be anticipated since 10% threshold level yields the only unambiguous point on the waveform (*ibid*) whereas other threshold levels may provide a false retracked gate due to the complexity of the waveform obtained over rough surfaces. Figure 3.7 illustrates the variations (in terms of standard deviation) of retracked surface heights calculated using TOPEX data from cycle 49 to 85 (January 1994 to January 1995) over every 10-Hz stackfile bin. Variations only from 0 to 10 m are plotted for clear comparison, and it can be seen that the most repeatable surface heights, which may indicate relatively smoother topographic surfaces, are concentrated at southern part of the Hudson Bay.

Retracker	Total No.	Processed No.	Ratio (%)	Standard deviation of difference (m)	Reduced variance (m^2)
(1) Pass 50					
Non-retracked	2370			6.01	
OCOG	2370	2311	97.5	5.78	2.71
10% Threshold	2370	2022	85.3	5.75	2.97
20% Threshold	2370	2206	93.1	5.88	1.56
50% Threshold	2370	2302	97.1	5.99	0.19
Modified 10% Threshold	2370	2220	93.7	**5.75**	**3.00**
(2) Pass 126					
Non-retracked	1642			5.00	
OCOG	1642	1601	97.5	**4.70**	**2.85**
10% Threshold	1642	1482	90.3	4.83	1.64
20% Threshold	1642	1561	95.1	4.84	1.52
50% Threshold	1642	1618	98.5	4.97	0.29
Modified 10% Threshold	1642	1587	96.7	4.81	1.86
(3) Pass 43					
Non-retracked	489			8.49	
OCOG	489	473	96.7	**8.13**	**6.03**
10% Threshold	489	395	80.8	8.15	5.66
20% Threshold	489	442	90.4	8.24	4.11
50% Threshold	489	469	95.9	8.42	1.11
Modified 10% Threshold	489	441	90.2	8.14	5.86
(4) Pass 119					
Non-retracked	768			8.85	
OCOG	768	757	98.6	8.58	4.67

Continued

Table 3.1: Statistics of TOPEX waveform retracking over Hudson Bay land region.

Table 3.1 continued

10% Threshold	2147	1805	84.1	7.98	2.99
20% Threshold	2147	1979	92.2	8.00	2.69
50% Threshold	2147	2079	96.8	8.15	0.14
Modified 10% Threshold	2147	1945	90.6	**7.88**	**4.57**
(10) Pass 67					
Non-retracked	2039			8.39	
OCOG	2039	1990	97.6	**8.28**	**1.91**
10% Threshold	2039	1766	86.6	8.38	0.17
20% Threshold	2039	1913	93.8	8.37	0.28
50% Threshold	2039	1990	97.6	8.47	-1.40
Modified 10% Threshold	2039	1877	92.1	8.40	-0.15
(11) Pass 143					
Non-retracked	1459			9.58	
OCOG	1459	1398	95.8	**9.24**	**6.41**
10% Threshold	1459	1120	76.8	9.49	1.78
20% Threshold	1459	1268	86.9	9.54	0.87
50% Threshold	1459	1381	94.7	9.57	0.26
Modified 10% Threshold	1459	1248	85.5	9.40	3.50
(12) Pass 178					
Non-retracked	1677			7.72	
OCOG	1677	1608	95.9	7.46	3.92
10% Threshold	1677	1351	80.6	7.42	4.52
20% Threshold	1677	1521	90.7	7.55	2.59
50% Threshold	1677	1607	95.8	7.73	-0.20
Modified 10% Threshold	1677	1494	89.1	**7.37**	**5.31**

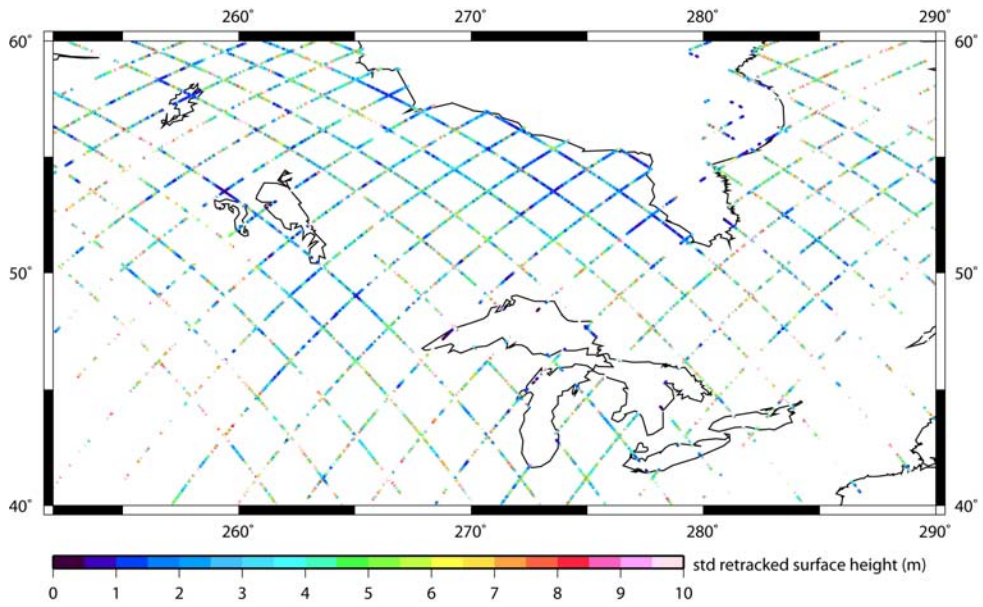

Figure 3.7: Standard deviations of retracked surface heights calculated from TOPEX cycle 49 to 85 over every 10-Hz nominal ground track location. Only variation between 0 to 10 m are shown for easier comparison.

3.4 Surface Gradient Error

Despite the exact-repeat orbit design of the satellite altimeter, the actual track of each repeated satellite visit deviates from the nominal ground track although it is a mission criterion to conduct orbital maneuver to be within a distance of ±1 km perpendicular to the nominal ground track at the equator. In the case of ocean stackfile, the along- and cross-track sea surface gradients are estimated in the bin with a planar approximation after the removal of the annual and semi-annual signals (Kruizinga, 1997). The similar approach has been used for relatively flat land surfaces around Hudson Bay in Lee et al. (2008a) (see Chapter 2.4), which is no longer applicable to the rough surfaces. In this study, the SRTM elevations at the 10-Hz stackfile bin center locations (or 10-Hz nominal ground track coordinates) and the actual 10-Hz ground track coordinates per each cycle are evaluated using bilinear interpolation. The differences between them are added back to the retracked surface height such as:

$$LSH_{nom,i}^{corr} = LSH_{cyc,i}^{uncorr} + \left(SRTM_{nom,i} - SRTM_{cyc,i}\right) \tag{3.3}$$

where $LSH_{nom,i}^{corr}$ represents the gradient-corrected retracked land surface height at 10-Hz nominal ground track (or 10-Hz stackfile bin, computed from Equation (3.1) and

(3.2)) for i th ($i = 1, \cdots, 10$) measurement; $LSH_{cyc,i}^{uncorr}$ is the uncorrected retracked land surface height at 10-Hz ground track of a specific cycle; $SRTM_{nom,i}$ is the SRTM elevation at the 10-Hz nominal ground track; $SRTM_{cyc,i}$ is the SRTM elevation at the 10-Hz ground track of the specific cycle. The SRTM elevations are converted to be with respect to the T/P reference ellipsoid to be consistent.

In this way, the real elevation differences between the nominal and the actual ground track of each cycle are estimated and removed. Finally, the retracked and surface gradient-corrected surface heights per cycle are stored in the 10-Hz stackfile bin. Figure 3.8 shows a part of SRTM DEM used in this study over Hudson Bay land region. The wiggle plot represents the calculated surface gradient correction along the nominal ground tracks of pass 245 and 50. Figure 3.8 (b) shows an example of a TOPEX time series over the circled area in Figure 3.8 (a) before and after the gradient correction. We can clearly see that the amplitude of the time series has decreased after the gradient correction. Figure 3.9 shows histograms of surface height variations of each 10-Hz stackfile bin calculated using data from cycle 9 to 364. The upper and lower panels are for pass 93 and 119, respectively. The left-most figures show histograms using raw surface heights with standard deviations < 10m. The middle histograms are generated using retracked surface heights, and it can be seen that the count values in y-axis has increased for < 2 m histogram bins. The right-most histograms are generated from retracked and gradient corrected surface heights, and it is clear that the gradient correction further decreases the spurious height variations. These results again validate the robustness of our retracking and surface gradient correction method. However, it is also noted that retracking and surface gradient correction may produce more noise to the raw surface heights with standard deviation larger than 5 m. In this study, 10-Hz stackfile bins with height variation smaller than 2 m are used.

Finally, land surface anomalies are calculated using the SRTM elevation along the 10-Hz nominal ground track as a reference surface. The anomalies within a circle of an empirically chosen 0.5 degree radius are spatially averaged for each cycle to reduce the random noise, and the crustal uplift rates, assigned to the 1-Hz stackfile bin locations, are estimated along with annual and semi-annual variations using least-squares adjustment:

$$\begin{aligned} LSA = A + B \cdot (t - t_0) + c1 \cdot \cos[\omega(t - t_0)] + s1 \cdot \sin[\omega(t - t_0)] + \\ c2 \cdot \cos[2\omega(t - t_0)] + s2 \cdot \sin[2\omega(t - t_0)] \end{aligned} \tag{3.4}$$

with:

LSA : land surface anomaly;

A : offset or bias;

B : crustal uplift rate;

$c1, c2$: amplitudes of the cosine term;

$s1, s2$: amplitudes of the sine term;

ω : annual frequency.

An example of the generated TOPEX time series is given in Figure 3.10 with its estimated vertical motion, and physical sources of the seasonal variation in the time series will be further examined in Chapter 3.5.

(a)

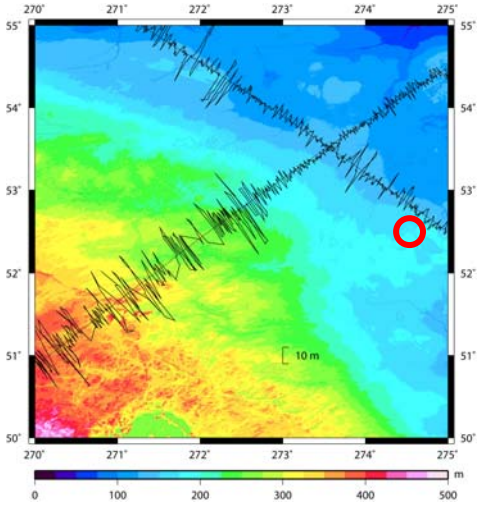

(b)

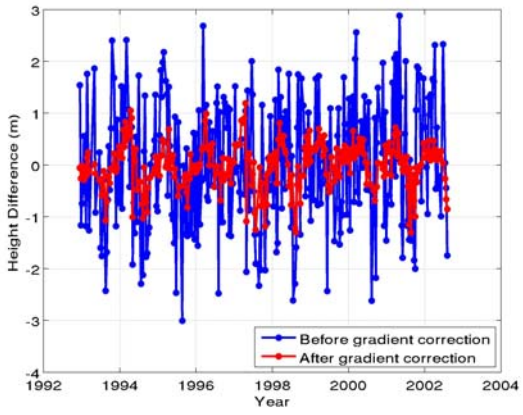

Figure 3.8: (a) An example of the calculated gradient correction using SRTM C-band DEM (background) along TOPEX passes 245 and 50. (b) An example of a TOPEX time series over the red circled area before and after applying the gradient correction. Standard deviation of the time series is reduced from 1.23 m to 0.43 m. The causes of the remaining variations will be discussed in Chapter 3.5.

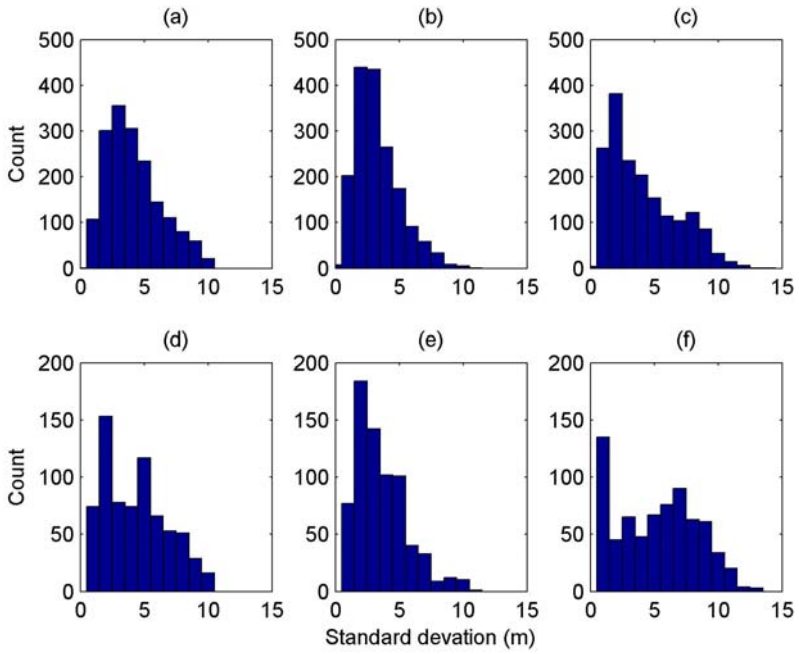

Figure 3.9: Histograms of surface height variations of each 10-Hz stackfile bin over pass 94 and pass 119 for upper and lower panels, respectively: (a and d) histograms using surface heights without any corrections; (b and e) histograms from retracked surface heights using the modified 10% threshold retracker; (c and f) histograms generated from retracked and surface gradient corrected heights using the SRTM DEM.

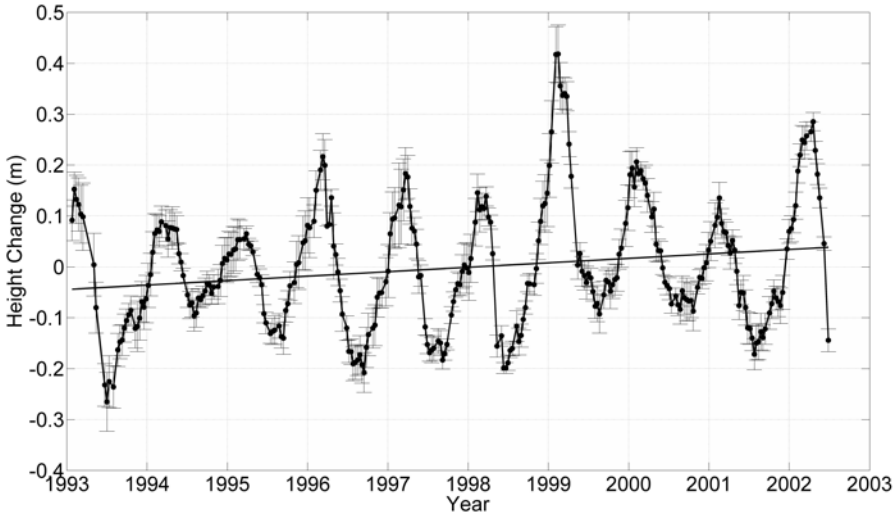

Figure 3.10: Example of the generated TOPEX time series over pass 50 (50.43˚N, 80.78˚W). The estimated vertical motion is 8.7 ± 1.4 mm/year.

3.5 Results

All of the constructed time series from land altimetry show increasing heights during winter season and decreasing heights during summer season with amplitudes up to several decimeters (e.g. Figure 3.10). This agrees with the seasonal changes in the Northern Hemisphere because the surface of our study area, Hudson Bay land region, will be covered by snow/ice in winter/spring, and by vegetation/soil in summer/fall. A recent study by Davis et al. (2005), who performed crossover analysis over Antarctica using ERS data, reveals similar amplitude and phase of seasonal signals for the basin-averaged ice sheet height change time series. It shows that the ice sheet heights increase as austral winter begins, and start to decrease as austral summer begins with different amplitudes up to several decimeters from basin to basin. Braun and Fotopoulos (2007) have shown using ICESat laser altimetry that the measured land surface elevations over Canada increase significantly in winter due to snow cover. Relative to SRTM, the determined elevations decrease in summer, which is also associated with changing vegetation. Although the findings of the both studies generally agree, laser and radar altimetry have different penetration depths because the radar can penetrate into snow while laser signals bounce off the snow surface. Therefore, we can speculate that the physical causes of the phase and amplitude of the TOPEX time series are the variation of the snow depth on the ground in combination with vegetation cover changes. During winter, snow covers vegetation and likely raises the reflective surface for TOPEX radar.

It is well known that the penetration depth of radar into dry snow may vary from a few centimeters to tens of meters depending on the particle size, the snow density, and the microwave frequency (Ulaby et al., 1986). Specifically, at 13.5 GHz frequency, which is of primary interest because TOPEX Ku-band altimeter operates at this frequency, the depth of penetration into the continental ice sheets can be ranged from 6.7 to 9.2 m depending on the magnitude of the scattering coefficient of the polar snow (Davis, 1992). The penetration depth for a medium of constant extinction coefficient can be expressed as:

$$d_p = \frac{1}{\kappa_e} \tag{3.5}$$

where κ_e is the extinction coefficient.

The extinction coefficient is the sum of the absorption and the scattering coefficient, and both absorption and scattering losses can contribute to the total extinction at 13.5 GHz frequency. Specifically, the magnitude of the scattering coefficient is very sensitive to the grain size. Figure 3.11 shows the penetration depth in (dry) snow as a function of frequency and snow grain size with assumed snow density and temperature. It can be seen that the penetration depth decreases rapidly as the grain size increases at a given frequency. Due to the fact that the snow in Hudson Bay land region mainly consists of ‘depth hoar’ as it is be classified as either ‘tundra’ or ‘taiga’ (Sturm et al., 1995), the snow

grain size in the study area is in the range of 2 to 5 mm in radius, but some can be much larger than this (Paterson, 1994). According to Figure 3.11, the penetration depth can range approximately from 2 cm to 15 cm as the grain size varies from 2 mm to 5 mm in radius. When the snow contains small amounts of liquid water, the penetration depth becomes much less because water increases the absorption loss by several orders of magnitude (Hallikainen et al., 1986; Davis, 1992). This can be seen from Figure 3.12, which illustrates the penetration depth as a function of frequency and liquid water content with given snow density and temperature. In conclusion, we may expect the penetration depth to be several centimeters or less, which may lead to a negligible amount of penetration, and thus the time series from land altimetry may represent snow depth variation. It should also be noted that the collinear analysis technique can potentially diminish "common" Ku-ban radar penetration over altimetry repeat passes.

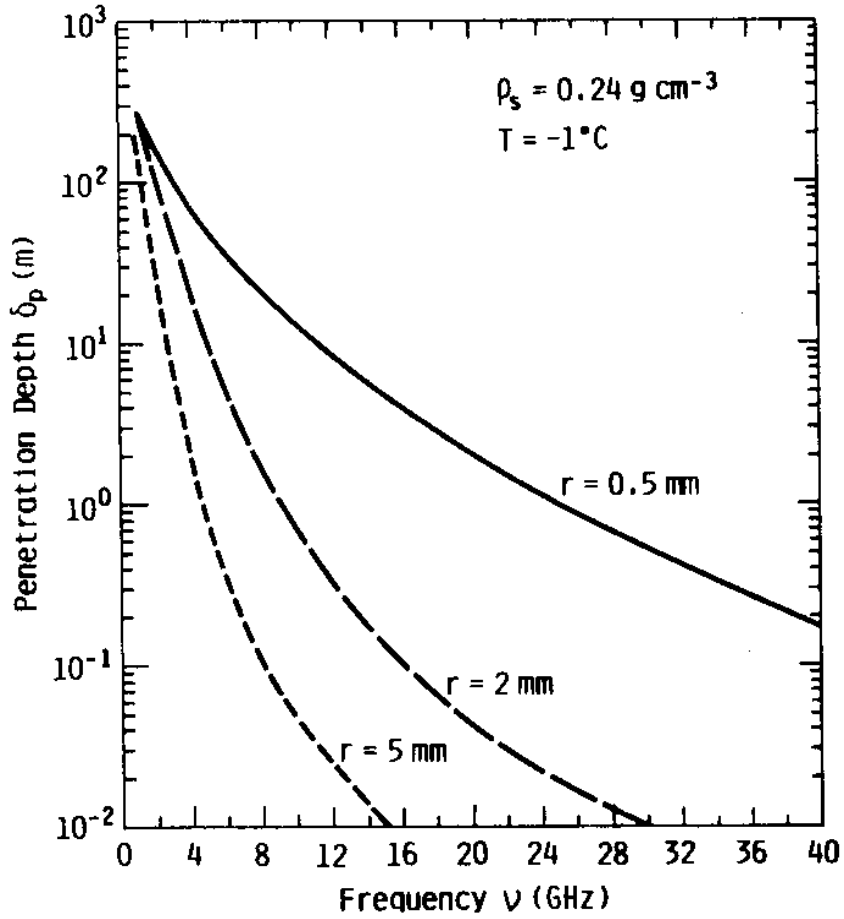

Figure 3.11: Penetration depth of snow as a function of snow grain size and microwave frequency with given snow density and temperature (after Ulaby et al., 1986).

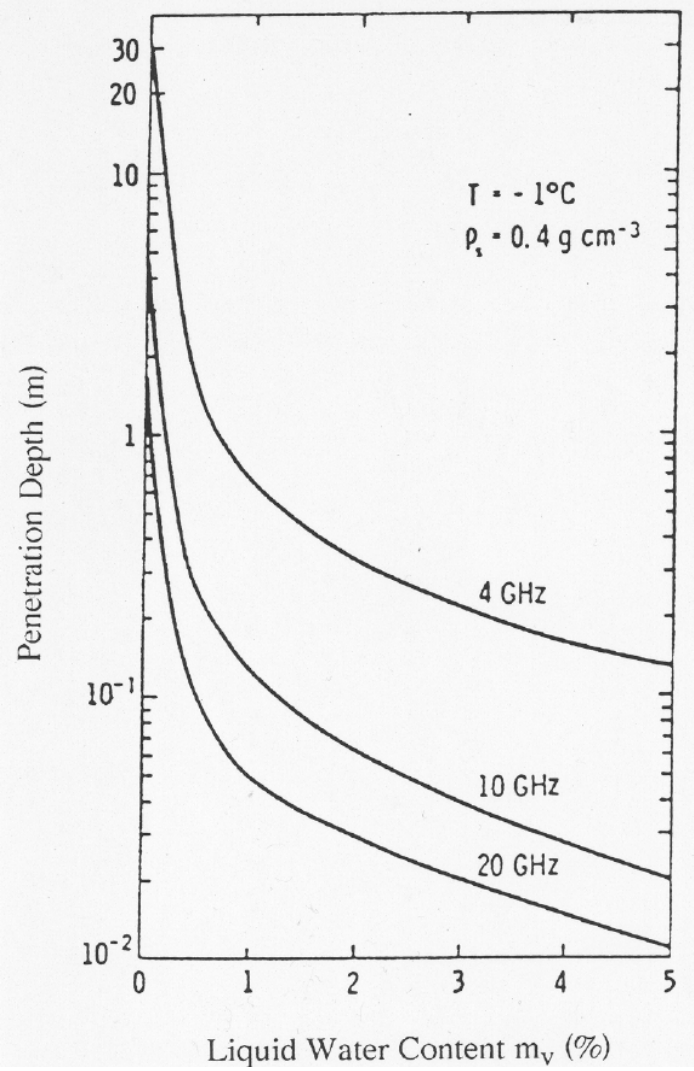

Figure 3.12: Penetration depth of snow decreases rapidly with increasing liquid water content (after Ulaby et al., 1982).

To validate the speculation, *in situ* snow depth data contained in Canadian Daily Climate Data CD are compared with TOPEX time series. The red diamonds with number 1, 2 and 3 in Figure 3.14 (b) indicate the location of the *in situ* sites and the black diamonds with number 1, 2, and 3 show the nearby TOPEX sites to be compared. It can be seen from Figure 3.13 (a), (b), and (c) that the phase and amplitude of the land altimetry and *in situ* snow depth time series show excellent correlation which validates the assumption. To reinforce our physical interpretation of land altimetry time series, we also investigated the seasonal variation of Ku-band backscattering coefficient obtained from TOPEX which are shown in Figure 3.13 (d), (e), and (f) corresponding to the sites 1, 2, and 3, respectively. As snow season starts around beginning of November, the backscattering coefficients start to decrease, and increase again as the snow season ends. These results agree with Papa et al. (2002), who compared backscattering coefficients

with *in situ* snow depths. In conclusion, the time series of land surface anomalies obtained from TOPEX altimetry over Hudson Bay land surfaces represent the snow depth variation, indicating that altimetry is measuring physical quantities and providing confidence of the approach to remove the snow depth seasonal variation to improve the vertical motion determination.

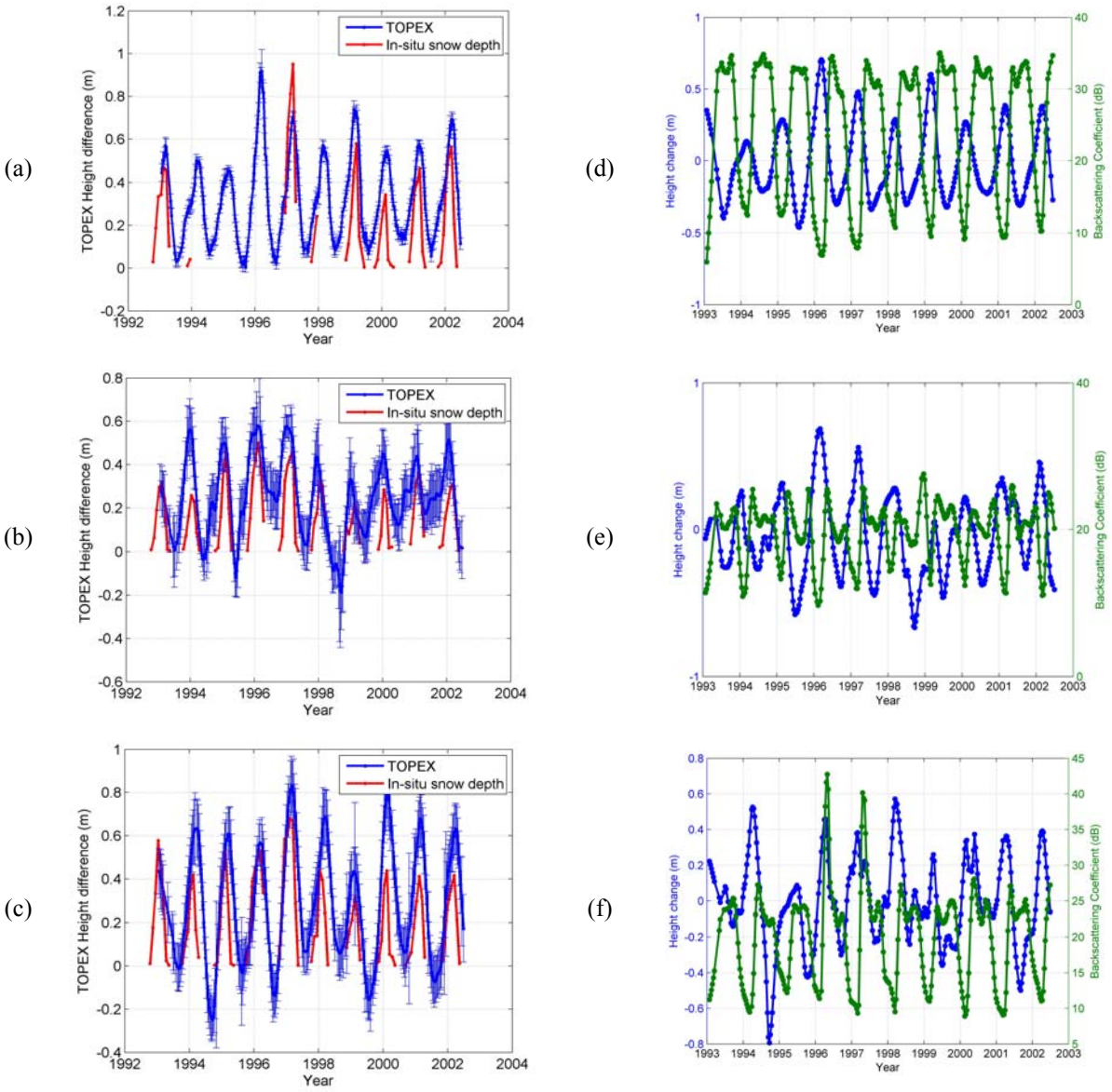

Figure 3.13: Examples of TOPEX time series (locations shown as black diamonds in Fig. 3.14 (b)) with nearby *in situ* snow depth time series (locations shown as red diamonds in Fig. 3.14 (b)). Sites 1, 2, and 3 correspond to (a), (b) and (c), respectively. (d), (e), and (f) show Ku-band backscattering coefficient change (green lines) obtained by TOPEX along with surface height change (blue lines).

In order to estimate the GIA trend, the seasonal signal due to the snow depth variation is removed while simultaneously estimating the trend of the time series to extract the GIA signal using Equation (3.4). The estimated linear trends from TOPEX altimetry time series are quantitatively compared with the predicted vertical motion from several GIA models and the crustal motion inferred from GRACE coefficients, and qualitatively compared with nearby GPS (Sella et al., 2007) and tide gauge/altimetry vertical motion (Kuo et al., 2008). Hence, it is assumed that the observed vertical motion from altimetry, GRACE, and GPS are predominately the result of the undergoing GIA process. One of the most established ice loading models is the ICE-3G model (Tushingham and Peltier, 1991), which describes the global deglaciation history following the LGM and has been updated by incorporating new observations and GIA modeling in the ICE-4G (Peltier, 2002) and the ICE-5G model (Peltier, 2004). While these are combined with two of the radially symmetric viscosity profiles, called VM2 and VM4, a number of studies have been conducted to incorporate lateral viscosity variations (Kaufmann et al., 1997; Wu and van der Wal, 2003; Wu 2005, 2006; Wang and Wu, 2006a, 2006b). The GIA models used for comparison in this study include RF3S20 (reference model RF3 with lateral viscosity perturbation from seismic tomography model S20) (Wang et al., 2008) which has lateral viscosity variation as well as radially symmetric ICE-4G (VM2), ICE-5G (VM2) (Peltier, 2002, 2004). RF3S20 has a laterally homogeneous lithosphere and a viscosity profile close to Peltier's VM2 model with the ICE-4G ice loading history. The lateral heterogeneity is inferred from seismic tomography model S20 by converting perturbations of seismic velocities into perturbations of viscosity using a scale factor β = 0.0, 0.2, 0.4, 0.6, and 1.0. The value of β = 0.0 means that the model is laterally homogeneous, and lateral viscosity contrast increases as β increases. If β = 1.0, velocity variations are considered completely due to thermal effects only. A detailed description of the RF3S20 model can be found in Wang et al. (2008), and it is also used by Braun et al. (2008) to be compared with various geodetic observations around the Great Lakes. In addition to the land altimetry solutions (land ALT, 202 sites), GPS (228 sites) rates and tide gauge/altimetry (TG/ALT, 51 sites) vertical motion estimates around the Great Lakes from Kuo et al. (2008) are compared with the GIA models by computing mean and standard deviation values of the differences between i) land ALT and GIA, ii) GPS and GIA, iii) TG/ALT and GIA, and iv) between a combination of all observations and GIA. It should be noted that these three observation types have different spatial distribution. Most of the land ALT sites are located in the southern part of the Hudson Bay whereas the TG/ALT sites are located around the Great Lakes (Braun et al., this issue), and the GPS sites are spread out in Canada and the United States as shown in Figure 3.14 (Sella et al., 2007). Figure 3.14 (a) shows the observed vertical motion from land ALT (color-coded circles), GPS (black arrows), and TG/ALT (red arrows) with a background from GIA model ICE-5G (VM2), and Figure 3.14 (b) illustrates their formal uncertainties. It should be noted that the correlation between the data points within a time series exists, and obtaining more realistic estimates of the formal uncertainties could be a topic for future research. Nonetheless, it is remarkable that the average uncertainty of the land ALT solution is 2.9 mm/year and comparable to the GPS solution, which is 2.1 mm/year. From Table 3.2, land ALT shows the smallest absolute mean value of -0.1 mm/year with respect to the GIA Model RF3S20 (β=0.4),

and a standard deviation of 2.2 mm/year with respect to RF3S20 (β=0.0) or RF3S20 (β=0.4). The GPS results show the smallest mean of 0.2 mm/year with respect to ICE-4G (VM2), but the smallest standard deviation of 2.3 mm/year with respect to RF3S20 (β=0.0) or RF3S20 (β=0.2). The smallest mean value for TG/ALT is 0.1 mm/year relative to ICE-4G (VM2) and the smallest standard deviation value is 0.6 mm/year with respect to RF3S20 (β=0.0) or RF3S20 (β=0.2). The combination of all of the datasets reveals the smallest mean value of 0.0 mm/year with respect to RF3S20 (β=0.0) or -0.1 mm/year to RF3S20 (β=0.2) while it shows the smallest standard deviation of 2.3 mm/year relative to RF3S20 (β=0.0), RF3S20 (β=0.2), and RF3S20 (β=0.4). It must be noted that the density of the data is still too coarse to evaluate the model performance over entire ancient Laurentia ice sheet, but it can be concluded that the new land ALT results as well as other types of observations agree well with different GIA model predictions.

(a)

(b)

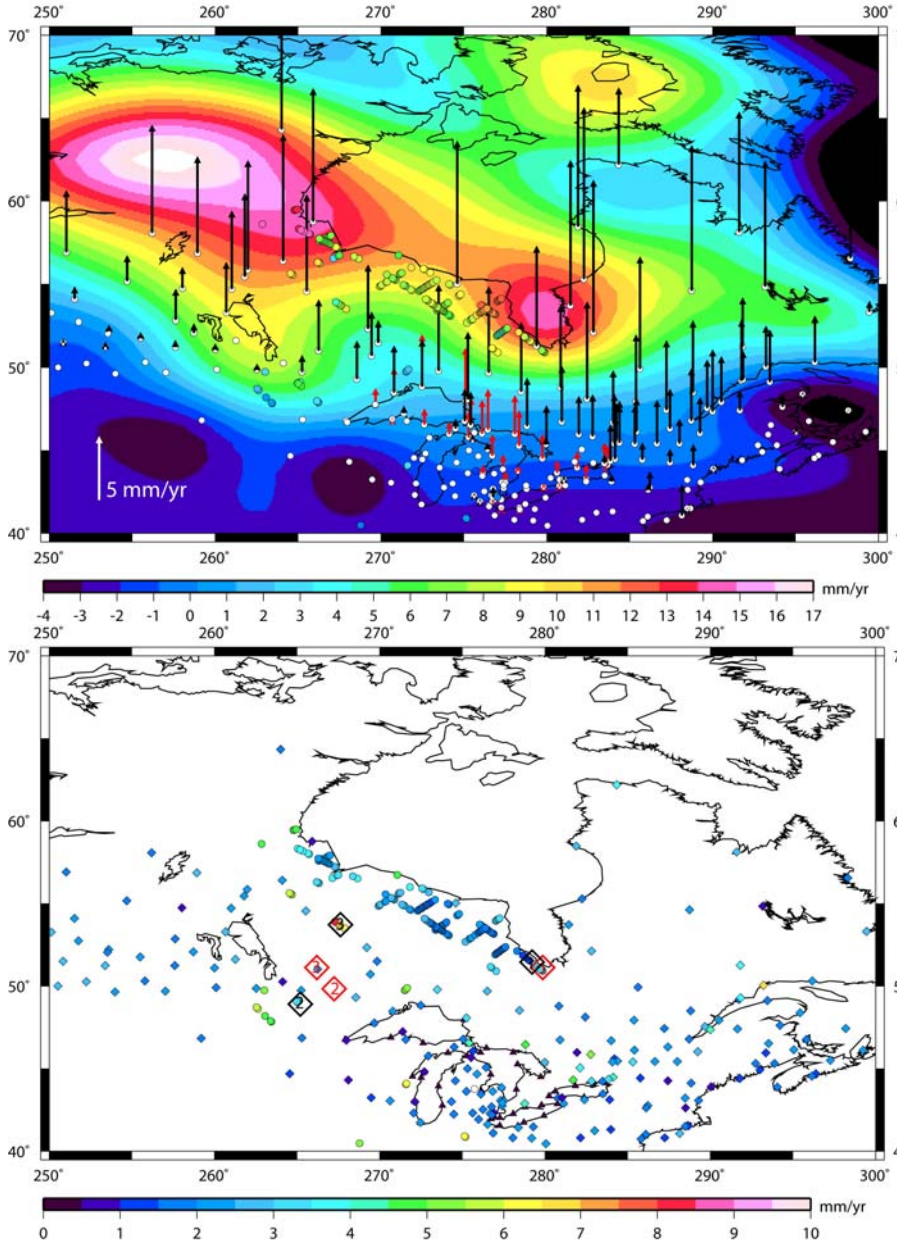

Figure 3.14: (a) Vertical deformation rates observed from land ALT as color-coded circles, GPS (Sella et al., 2007) as black arrows, and TG/ALT (Kuo et al., 2008) as red arrows. White circles indicate the locations of GPS and TG/ALT sites. Background is the predicted vertical crustal uplifts from ICE-5G (VM2); (b) Formal uncertainties of estimated vertical motion for land ALT (circle), GPS (diamonds), and TG/ALT (triangle). Red empty diamonds 1, 2 and 3 indicate the location of the *in situ* snow depth sites and black diamonds with the same number show the nearby land ALT sites used for their comparison (see Fig. 3.13).

The observed vertical motion from land ALT, GPS, and TG/ALT are further compared with the vertical motion inferred from the Gravity Recovery and Climate Experiment (GRACE) monthly spherical harmonic coefficients. The GRACE satellite was launched on 17 March 2002, with objectives including the mapping of the global gravity field and its temporal variation. It enables low-low satellite-to-satellite tracking (SST) using microwave intersatellite ranging, designed to map the global gravitational signal with a resolution of 250 km or longer, and a temporal resolution of a month for a time-span of 5 years (Tapley et al, 2004; Han et al., 2003). The detailed formula to convert the rates of change of the GRACE geoid coefficients to the vertical motion of the Earth's surface can be found in Wahr et al. (2000). The contribution of GIA to the secular rate of change in the geoid can be expressed as:

$$\dot{N}^{GIA}(\theta,\phi) = a\sum_{l=0}^{\infty}\sum_{m=0}^{l}\widetilde{P}_{lm}(\cos\theta)\left[\dot{C}_{lm}^{GIA}\cos(m\phi)+\dot{S}_{lm}^{GIA}\sin(m\phi)\right] \tag{3.6}$$

where θ and ϕ are co-latitude and longitude; $\widetilde{P}_{lm}$ are normalized associated Legendre functions; a is the mean equatorial radius of the Earth; $\dot{C}_{lm}^{PGR}$, $\dot{S}_{lm}^{PGR}$ represents the rates of change of the geoid coefficients, C_{lm}, S_{lm}, which are dimensionless geoid coefficients which GRACE delivers every month.

Similarly, the uplift rate of the Earth's surface caused by GIA can be expressed as:

$$\dot{U}^{GIA}(\theta,\phi) = a\sum_{l=0}^{\infty}\sum_{m=0}^{l}\widetilde{P}_{lm}(\cos\theta)\left[\dot{A}_{lm}^{GIA}\cos(m\phi)+\dot{B}_{lm}^{GIA}\sin(m\phi)\right] \tag{3.7}$$

where $\dot{A}_{lm}^{GIA}$ and $\dot{B}_{lm}^{GIA}$ are the Legendre expansion coefficients of $\dot{U}^{GIA}$.

Wahr et al. (2000) have found that

$$\begin{aligned}\dot{A}_{lm}^{GIA} &= \left(\frac{2l+1}{2}\right)\dot{C}_{lm}^{GIA}\\ \dot{B}_{lm}^{GIA} &= \left(\frac{2l+1}{2}\right)\dot{S}_{lm}^{GIA}\end{aligned} \tag{3.8}$$

However, it should be noted that they found Equation (3.8) works well if the Earth's viscosity profile is spherically symmetric.

The GRACE inter-satellite ranging measurements are inherently insensitive to degree-1 terms (or geocenter), and thus it is not included (as well as degree-0) in monthly GRACE gravity coefficients because the GRACE data processing defines the origin of the reference frame as the instantaneous center of mass of the Earth (CM) (Chambers et al., 2007; van der Wal et al., 2008). In this study, the improved degree-1 estimates from Lageos Satellite Laser Ranging (SLR) by estimating and removing the range biases for

each station (J. Ries, personal communication, 2008) are included in the monthly spherical harmonic coefficient sets.

$$\Delta C_{10}(t) = \frac{\Delta z(t)}{a\sqrt{3}}$$
$$\Delta C_{11}(t) = \frac{\Delta x(t)}{a\sqrt{3}} \qquad (3.9)$$
$$\Delta S_{11}(t) = \frac{\Delta y(t)}{a\sqrt{3}}$$

where $(\Delta x(t), \Delta y(t), \Delta z(t))$ is the position of the instantaneous mass center relative to the origin of the terrestrial reference frame obtained from the SLR measurements.

After the hydrological contamination is removed using monthly spherical coefficient data sets (Velicogna and Wahr, 2006a; data courtesy, J. Wahr) converted from the GLDAS/Noah global water storage fields (Rodell et al., 2004), a spatially comprehensive vertical motion based on the assumption that the residual represents GIA signal is inferred. It is obvious that the magnitude and location of the domes observed from GRACE are sensitive not only to various error sources, but also to the inadequate and short data time span, which can be seen from Figure 3.15 (d) which is derived from 36 month of GRACE data from April 2002 to July 2005. Although it still shows the multidomal Laurentide ice geometry, the vertical motion in the southern part of Hudson Bay shows subsidence, which seems unlikely. Furthermore, the feature of the transition zone around the Great Lakes is lost. All of the GRACE results are smoothed using 300 km by 600 km (half-wavelength, latitude and longitude filtering radii) non-isotropic filter (Han et al., 2005). The mean and standard deviation of the differences between GRACE and all of the other observations are also computed and shown in Table 3.2. It should be noted that spherical harmonic degrees only up to 70 are used for all of the GRACE results in Figure 3.15 and Table 3.2 because the hydrologic leakage data sets are provided only up to degree 70. It can be seen that the geocenter correction caused approximately 0.4 mm/year difference while the hydrologic leakage correction lead to about 1.1 mm/year difference overall. It is evident that GRACE-inferred vertical motion computed using shorter data span yields larger mean and standard deviation of the differences in all cases. Figure 3.16 illustrates the comparison of GRACE and altimetry solutions (land ALT and TG/ALT), which shows the general agreement between GRACE and land ALT with a bias of approximately 2.2 mm/year.

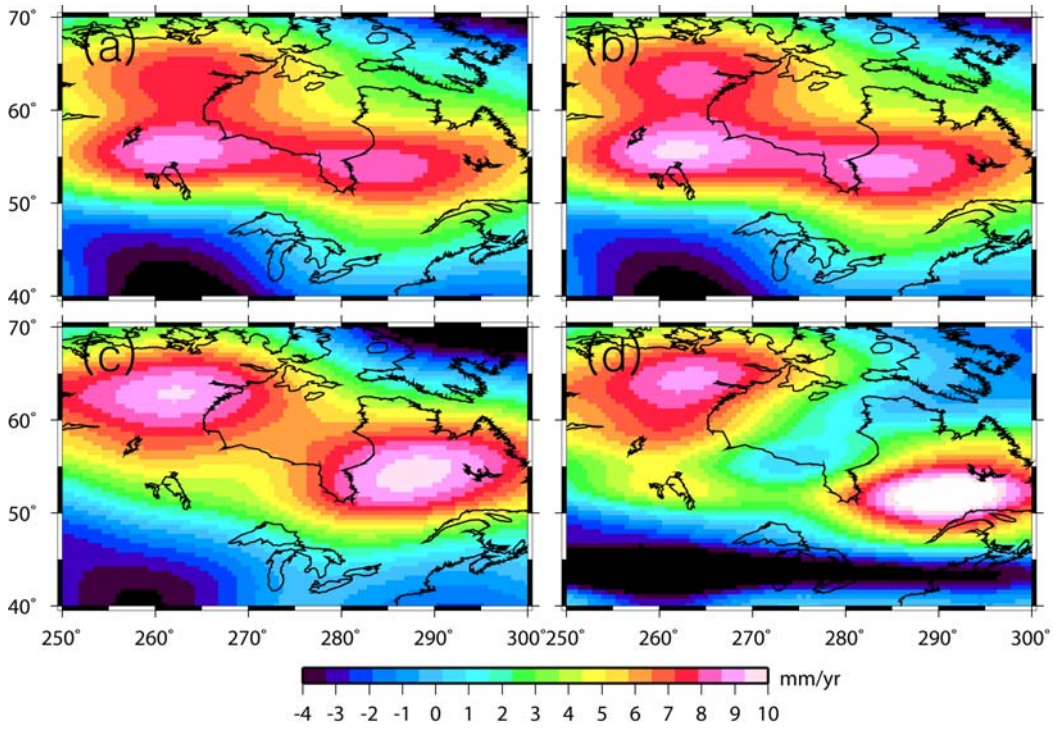

Figure 3.15: (a) GRACE-inferred vertical motion using JPL RL04 Level 2 products from April 2002 to December 2006 without any correction; (b) after geocenter correction; (c) after geocenter and hydrologic leakage corrections; (d) after applying the same corrections as (c), but with a shorter time span from April 2002 to July 2005.

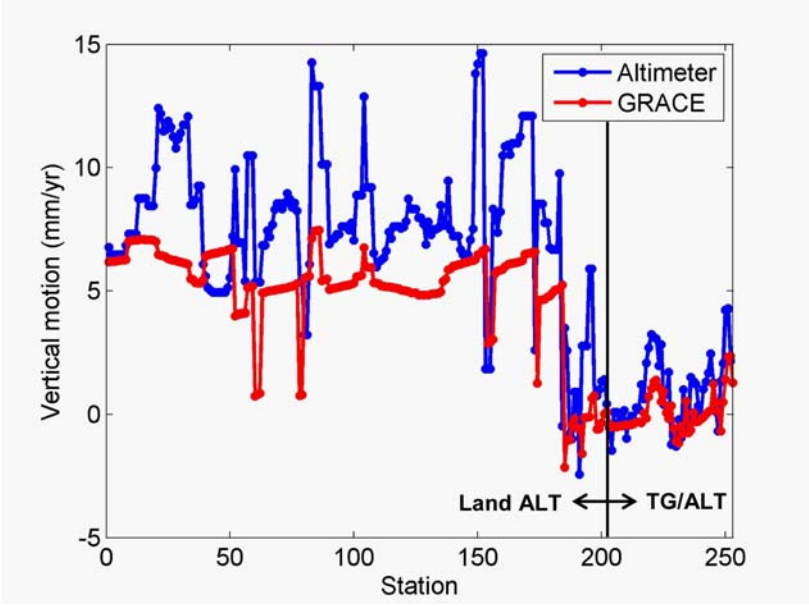

Figure 3.16: Comparison of GRACE and altimetry observed vertical motion. Altimetry solutions include land altimetry observation from this study and tide gauge/altimetry estimates from Kuo et al. (2008).

	Land ALT	GPS	TG/ALT	Land ALT + GPS + TG/ALT
ICE-4G (VM2)	-3.0 ± 2.4	-0.2 ± 2.5	0.1 ± 0.8	-1.3 ± 2.7
ICE-5G (VM2)	2.1 ± 2.5	-0.6 ± 3.0	-1.6 ± 1.1	0.4 ± 3.0
RF3S20 (β=0.0)	-0.8 ± 2.2	0.6 ± 2.3	0.8 ± 0.6	0.0 ± 2.3
RF3S20 (β=0.2)	-0.8 ± 2.3	0.4 ± 2.3	0.8 ± 0.6	-0.1 ± 2.3
RF3S20 (β=0.4)	-0.1 ± 2.2	0.8 ± 2.4	1.3 ± 0.7	0.5 ± 2.3
RF3S20 (β=0.6)	-0.5 ± 2.3	1.1 ± 2.6	1.6 ± 0.7	0.5 ± 2.5
RF3S20 (β=1.0)	-1.3 ± 2.3	1.1 ± 2.8	1.5 ± 0.9	0.1 ± 2.7
GRACE[a] (53 months)	-1.0 ± 2.3	0.8 ± 2.5	-0.6 ± 0.8	-0.2 ± 2.5
GRACE[b] (53 months)	-0.6 ± 2.3	1.2 ± 2.5	-0.2 ± 0.8	0.2 ± 2.5
GRACE[c] (53 months)	-2.2 ± 2.2	0.3 ± 2.1	-0.4 ± 0.7	-0.9 ± 2.4
GRACE[c] (36 months)	-5.3 ± 2.8	-1.3 ± 3.3	-4.0 ± 1.6	-3.4 ± 3.5

[a] Without any corrections
[b] After geocenter correction
[c] After geocenter and hydrologic leakage corrections

Table 3.2: Mean and standard deviation of the differences between the vertical motion from GIA models/GRACE and the estimated vertical motion from various geodetic observations (unit: mm/year).

3.6 Conclusion

An innovative technique to estimate geocentric vertical motion using satellite radar altimetry over land surfaces around Hudson Bay was presented. To obtain more data points than included in the previous study by Lee et al. (2008a), a 10-Hz North American regional stackfiles is built for an efficient processing of the height time series. An alternative modified threshold retracker for land waveforms was developed in this study. The use of 90-m C-band SRTM DEM played an important role as the reference for selecting an optimal retracker and to provide surface gradient corrections for the computation of land surface anomalies. As a result, it was demonstrated that crustal motion can be estimated even over rougher surfaces, where the standard deviation of the height variations is less than 2 m, with an average uncertainty of 2.9 mm/year which is comparable to 2.1 mm/year of GPS solution (Sella et al., 2007). Decadal vertical motion time series over a 1500 km by 1000 km region covering northern Ontario and northeastern Manitoba, and over the Great Lakes have been generated. The vertical motion estimates qualitatively agree well with other geodetic measurements from GPS (*ibid*) and tide gauge/altimetry combination (Kuo et al., 2008), which are primarily attributed to GIA. Another geodetic observation from GRACE was also used for comparison even though it was shown that the vertical motion inferred from GRACE Level 2 data are sensitive to various corrections and data time span. Land altimetry solutions were further compared with various GIA models and agreed well with the GIA model RF3S20 (β =0.4), whereas the combination of land ALT, GPS, and TG/ALT showed the best agreement with RF3S20 (β =0.0) and to a lesser extent, RF3S20 (β =0.2). Hence, although this study does not intend to assess the model performance in Laurentia, it can be concluded that the land altimetry solutions can be incorporated with other geodetic measurements to be used as additional constraints for GIA model improvements in the future.

The extension of the study region to Fennoscandia, where large GIA amplitudes up to ~10 mm/year can be observed (Milne et al., 2001), can be a future study. Other possible future studies include the use of other satellite radar altimeters, for example Envisat, by building 18-Hz stackfile to increase the spatial coverage and data time span. However, it is anticipated that the vertical motion from Envisat would be less accurate due to the shorter time span and than that of TOPEX.

CHAPTER 4

LOUISIANA VEGETATED WETLAND WATER LEVEL MONITORING

4.1 Introduction

Coastal estuaries, which connect coastal ocean, wetlands and coastal land region, play important roles in environments. Wetlands typically occur in low-lying areas on the edges of lakes, and rivers, or in coastal areas protected from waves. These wetlands are found in a variety of climates on every continent except Antarctica. Wetlands not only provide habitat for thousands of aquatic/terrestrial plant and animal species but also control floods by holding water like a sponge by absorbing and reducing the velocity of storm-water. Human activities have so many negative impacts on wetlands and they became main contributing factors to many wetland loss. Wetland loss is also caused by natural processes such as subsidence. Louisiana's wetland, one of the largest expanses of coastal wetland in the United States, has lost more than 100–150 km^2 of its area per year and the loss rate is increasing exponentially (Walker et al., 1987; Templet and Meyer-Arendt, 1988). The vertical crustal motion, subsidence in coastal Louisiana, is one of the primary reasons of the wetland loss. The geological subsidence is due to the loading inundation of ~130 meters of eustatic sea level rise at 21-5 kyr BP and Pleistocene sediment transport deposition to the Gulf of Mexico (Ivins et al., 2007). The equilibrium between the substrate surface and the relative sea level should be maintained to prevent the land loss and marine transgression, which are anticipated where aggradation is less than the relative sea level rise (Hatton et al., 1983). Therefore, the rising sea level together with the subsidence can accelerate the coastal erosion and wetland loss. Furthermore, it also accelerates the occurrence of flooding from the severe storm surges due to hurricanes such as the devastating Category 5 Hurricane Katrina which hit New Orleans on August 28, 2005.

The ability to quantitatively measure accurate wetland water level changes in Louisiana has impacts on ecology and natural hazards mitigation including improved storm surge modeling. Nevertheless, the water level gauging stations can be scarce or even absent in the floodplain/wetland due to the difficulty in physical accessibility. Hence,

satellite remote sensing can provide useful measurements to monitor the water level variation over those regions. InSAR has been proven to be useful to measure centimeter-scale water level changes over Amazon flood plain (Alsdorf et al., 2000, 2001) and Everglades wetland (Wdowinski et al., 2004) using L-band SAR imagery. This is based on the fact that flooded forests permit double-bounce returns, which allow InSAR coherence to be maintained. Furthermore, ERS-1/2 C-band InSAR data have been used to demonstrate its feasibility to monitor water level changes over Louisiana wetlands (Lu et al., 2005). In addition, satellite radar altimetry has been used to measure inland water level variation over large river basins (Birkett, 1998; Birkett et al., 2002; Maheu et al., 2003; Frappart et al., 2006). In this study, decadal (1992-2002) T/P data is used to measure water level changes over Louisiana wetlands. Unlike the previous studies, which spatially average 10-Hz data (or 18-Hz for Envisat) over a distance corresponding to the intersection between the satellite ground track and water body, the 10-Hz regional land stackfile technique is used over Louisiana wetlands. As a result, for the first time, measuring water level change over each 10-Hz stackfile bin, which has along-track ground spacing of ~660 m, will take place. The feasibility of applying retracking corrections is also demonstrated whereas previous studies (Birkett, 1998; Birkett et al., 2002; Maheu et al., 2003) considered radar returns from nominal tracking mode contained in TOPEX GDRs adequate.

4.2 Methodology

4.2.1 Target Selection

The study area includes the Teche/Vermillion Basin (Area1 and Area2), Barataria Basin (Area3), Lake Pontchartrain Basin (Area4), and Atchafalaya Basin (Area5) of coastal Louisiana (see Figure 4.2). Geographic boundaries of the study areas are selected using the land classification map from Louisiana Gap Analysis Program (GAP) by including only marsh regions which are intersected by the satellite passes and excluding agricultural cropland/grassland. The land cover classification map from GAP is given Figure 4.1. According to the land cover map from the Louisiana GAP project and other studies (Visser et al., 1998, 2000), the vegetation type of Area1 and Area2 is brackish marsh of which the measured mean mudline elevation is approximately 28 cm (Gammill et al., 2002). Area3 and Area4 are covered by saline marshes which are adjacent to the bays. Area5, upstream Atchafalaya Basin, is covered by swamp forest which is composed of moderately dense trees ranging from 10 to 25 m in height (Lu et al., 2005). Figure 4.2 illustrates the study areas with TOPEX tracks, and the detailed description is given in Table 4.1.

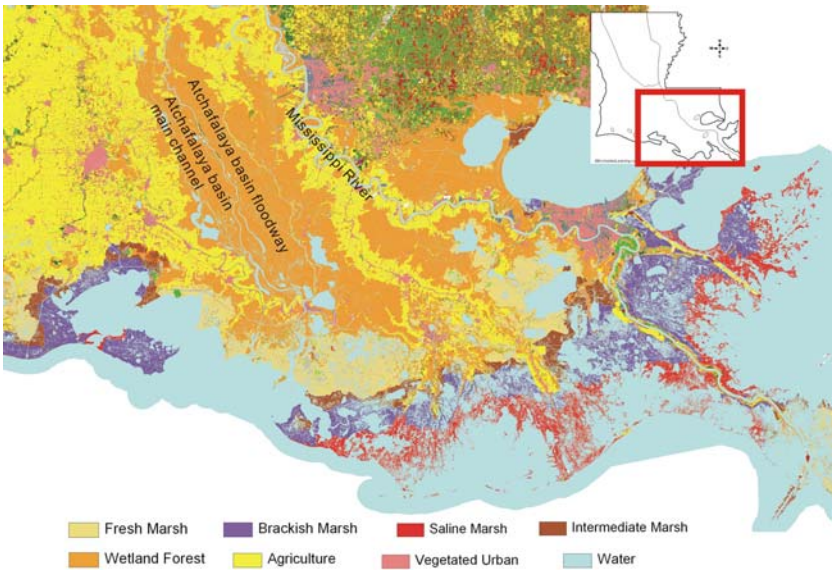

Figure 4.1: Classification map from GAP, showing major land cover classes of the study area (courtesy: Zhong Lu).

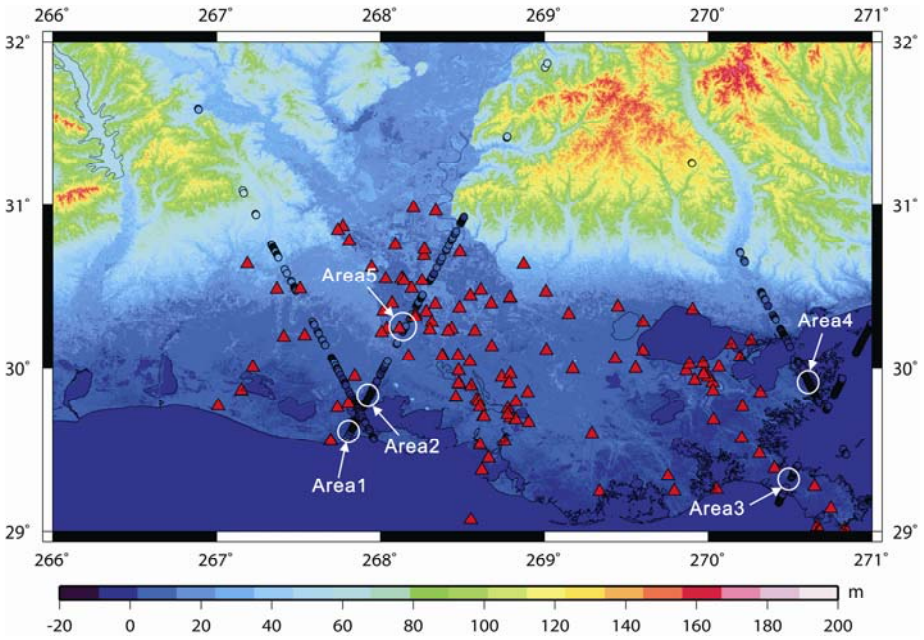

Figure 4.2: Map of Louisiana with TOPEX 10-Hz ground track of cycle 270. Background is SRTM C-band 90-meter resolution DEM, and red triangles represent river gauge stations, which can be accessed from the United States Army Corps of Engineers at http://www.mvn.usace.army.mil/eng/edhd/Wcontrol/wcmain.htm. In this study, historic water level data which are daily measured are used.

	Geographic Range, deg (lat,lon) to (lat,lon)		Pass	Gauge		Distance to gauge (km)	Vegetation
				ID	Name		
Area1	(29.574, -92.202)	(29.702, -92.136)	117	76592	Fresh Water North	16	Brackish Marsh
Area2	(29.732, -92.120)	(29.860, -92.054)	117	76720	Leland Bowman East	11	Brackish Marsh
Area3	(29.325, -89.495)	(29.386, -89.463)	193	01480	Venice	15	Saline Marsh
Area4	(29.853, -89.355)	(29.919, -89.389)	204	85800	Shell Beach	30	Saline Marsh
Area5	(30.373, -91.759)	(30.572, -91.681)	117	49255 03075	Bayou Fordoche Krotz Springs	9 7	Swamp Forest

Table 4.1: Details of the study areas in Louisiana wetland.

To identify “water-covered" surface, a test is performed based on pulse peakiness (PP) (Strawbridge and Laxon, 1994) computed from 10-Hz waveform, and 10-Hz Automatic Gain Control (AGC) parameter contained in TOPEX SDRs. The waveforms from water surface are usually defined by its high PP and AGC values (Birkett, 1998). The PP can be computed such as:

$$\text{Pulse Peakiness (PP)} = \frac{31.5 \times P_{\max}}{\sum_{i=1}^{64} P_i} \tag{4.1}$$

where $P_{\max}$ is the maximum power in the waveform, P_i, $i = 1, \cdots, 64$.

This is the similar procedure described in Birkett (1998) except that we utilized 10-Hz AGC assigned to each corresponding 10-Hz stackfile bin instead of 1-Hz backscattering coefficient (σ_0) because every 10-Hz range measurement of water surface from should be distinguished from that of vegetation. Because Area1, Area3, and Area4 are surrounded by the ocean, the PP and AGC values obtained over wetland are compared to those obtained over the ocean. On the other hand, Area2 and Area5 are located near agricultural cropland/grassland. Hence, the PP and AGC values are to be distinguished from those. Figure 4.3 illustrates the AGC versus PP values obtained from cycle 9 to 83 to include one year measurement along each study area, and a clear division can be observed between wetland and coastal ocean, or wetland and dry land. As a result, good wetland waveforms are defined according to the different PP and AGC thresholds (see Table 4.2), which have been determined differently from area to area.

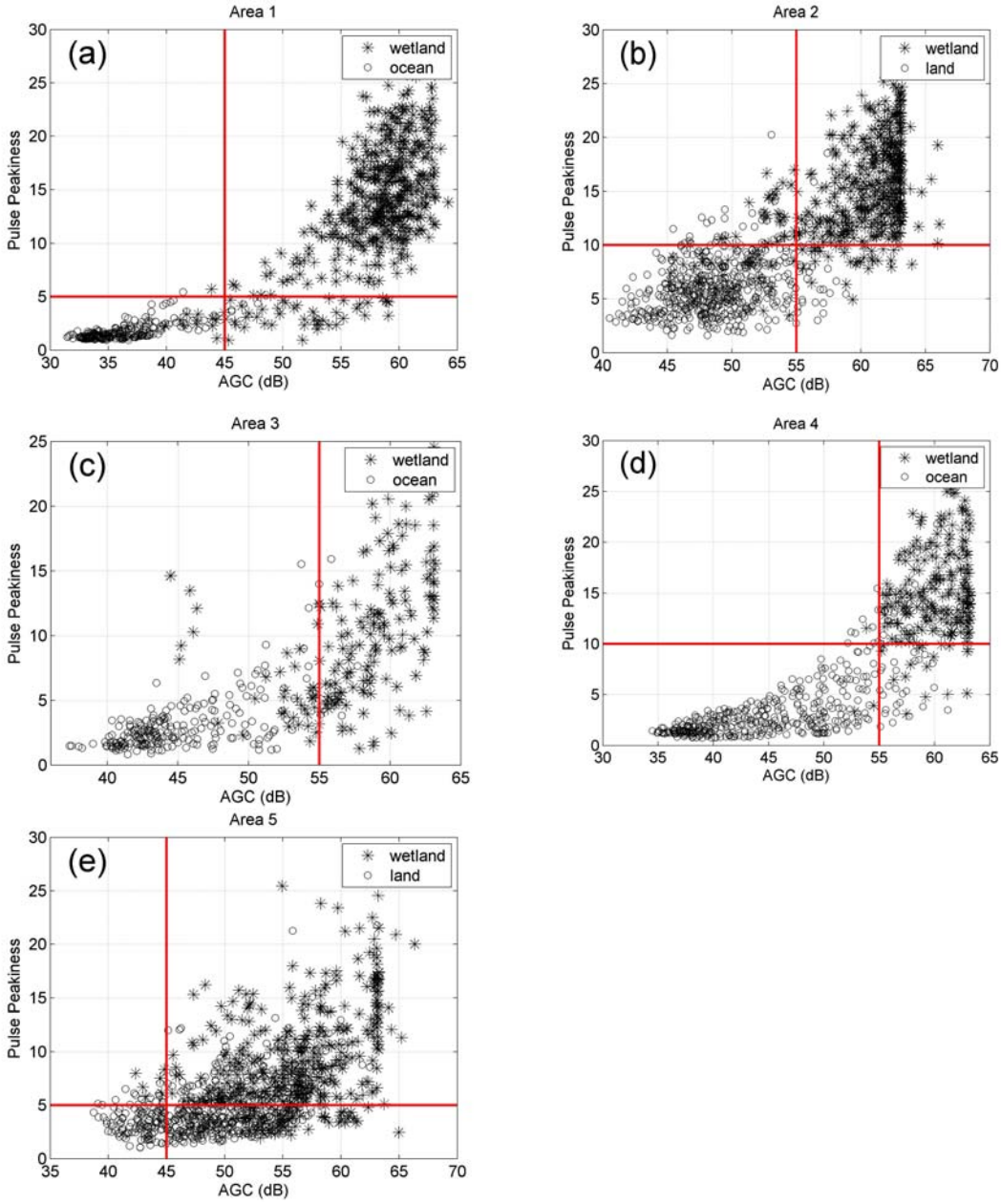

Figure 4.3: AGC versus PP plots over each study area. Thresholds of AGC and PP values to select possible water signals from the wetland are indicated as red straight lines.

	Area1	Area2	Area3	Area4	Area5
AGC	45	55	55	55	45
PP	5	10	-	10	5

Table 4.2 Thresholds of AGC and PP values used to define good wetland waveforms.

Figure 4.4 (i)s and (iii)s show the mean of AGC and PP values, computed from cycle 9 to 364, over each 10-Hz stackfile bin, and (ii)s and (iv)s illustrate the standard deviation of them. It is clear to see the spatial variation of the AGC and PP along the satellite track, which may represent the spatial variation of the surface characteristics, i.e., the variation of wetland water level or the vegetation canopy. Generally, the AGC and PP values show correlation between them, which can also be seen from Figure 4.3. It can be seen from Figure 4.4 (i)s and (iii)s of (a), (b), and (c) that the mean of AGC and PP values increase as the TOPEX ground track moves northward, which may indicate the presence of more water-covered wetland, and thus the radar return is dominated by surface water, not vegetation. It is also noted that, from Figure 4.4 (ii)s of (a), (b), (c), and (d), the standard deviation of AGC values decrease as the mean AGC values increase. It can also be seen from Figure 4.4 (i)s and (iii)s of (d), both ends of Area4, which may contain signal from the coastal ocean, show low AGC and PP values whereas the middle of the study area shows higher AGC and PP values. Over Area5, of which vegetation type is swamp forest, the AGC and PP values show smaller spatial variation compared to other study areas.

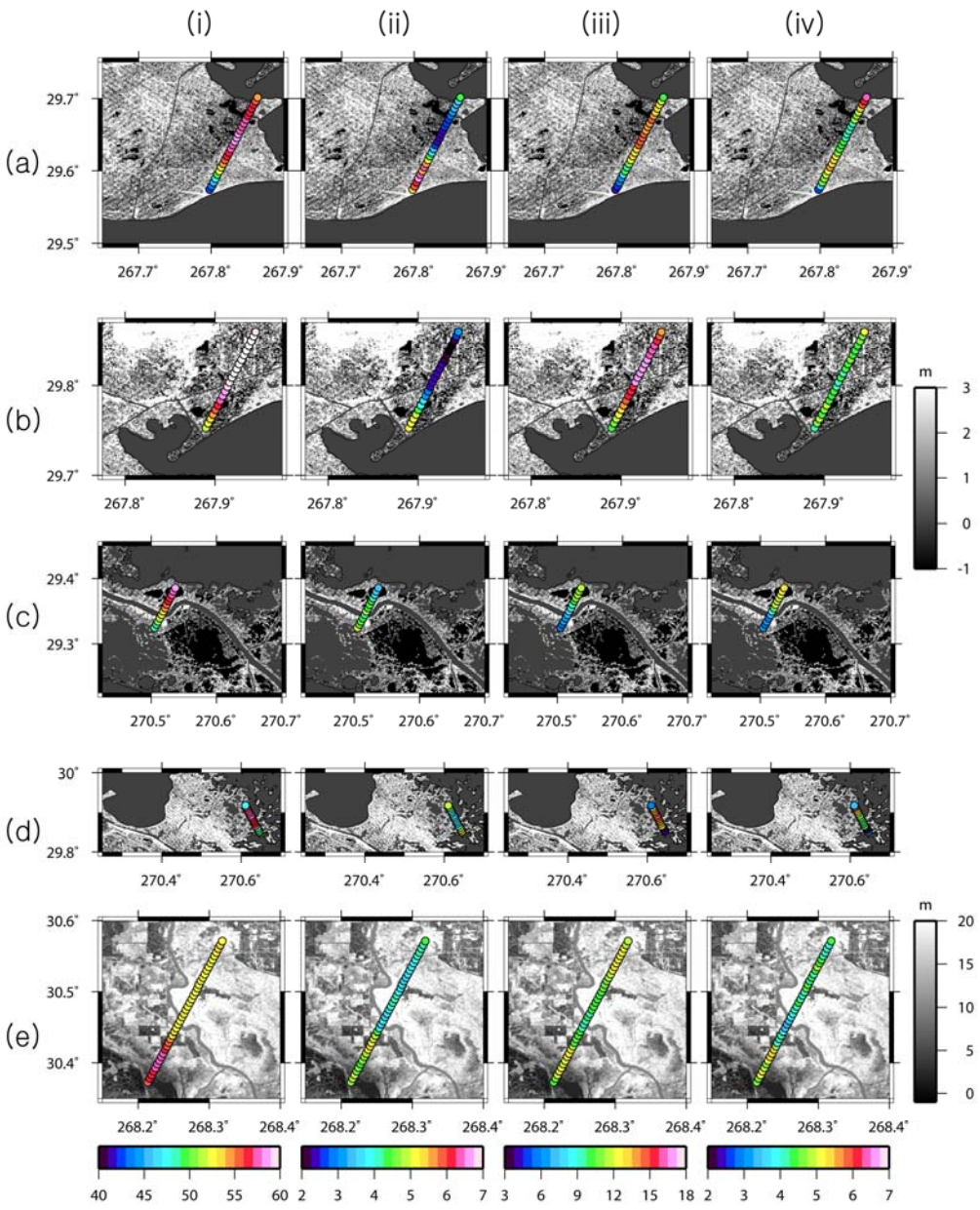

Figure 4.4: (i) Averages of AGC (dB), (ii) standard deviations of AGC (dB), (iii) averages of PP, (iv) standard deviations of PP over each 10-Hz stackfile bin of Area1 to Area5 ((a)~(e)). The background is SRTM DEM elevation (m) with its colour-bar on the right side. A common colour-bar is used for Area1 to Area4. The Mississippi River and the Atchafalaya River can be seen in Area3 and Area5, respectively.

4.2.2 Retracking

Over non-ocean surfaces, the altimeter measurements could be in error due to the complex nature of the signal obtained. Various waveform retracking techniques have been developed to correct the deviation of the waveform leading edge from the nominal predetermined tracking gate. The water surface in wetlands could be calm resulting in specular radar returns, or if the water surface is seasonally vegetated, irregular shape of radar waveforms will be obtained. These waveforms do not conform to the Brown (1977) model "standard" waveforms, hence the feasibility of retracking should be studied. Previous studies (Birkett, 1998; Birkett et al., 2002; Maheu et al., 2003) use 10-Hz range measurements contained in GDRs without applying retracking. Birkett (1998) concluded that retracking may cause unacceptable additional noise for constructing water level time series. It can be explained from the fact that the average positions of the waveform peak were close to the nominal tracking gate (for TOPEX, 24.5), which means the satellite is tracking the true water surface and retracking is not needed. However, this could be true only over large lake bodies such as the Great Lakes (Morris and Gill, 1994) or large river basins such as the Amazon (Birkett et al., 2002). In this study, the leading edge position of each 10-Hz waveform, using SDRs from cycle 9 to 364, along each 10-Hz stackfile bin using Offset Center of Gravity (OCOG) retracker (Bamber, 1994) is estimated and the variation of them is examined. Figure 4.5 shows an example of waveform shape variation along TOPEX ground tracks from cycle 49. Most of the waveforms over wetland regions are specular (or narrow-peaked) except the waveforms around the boundary between the ocean and wetland, which are very noisy (see Figure 4.5 (a)).

Although narrow-peaked waveforms may provide stable water height at times of level maxima (Birkett, 1998), the waveform shape over a 10-Hz stackfile bin may vary from cycle to cycle at times of level minima, which leads to the need of retracking. The variation of the retracked gate positions are shown in the boxplot of Figure 4.6 using the waveforms remained after the editing procedure using AGC and PP values. Area1_1 means the southernmost 10-Hz stackfile bin of Area1, Area1_2 means the next 10-Hz stackfile bin of Area1, and so on. Study sites of Area1_14, Area1_15, Area1_16, Area2_10, Area2_11, Area2_15, and Area4_11 are arbitrarily chosen among the study sites which show smaller variation in the position of retracked gate, and thus retracking may not be applied. Area3_6, Area3_9, Area5_15, Area5_17, Area5_18, Area5_19, and Area5_22 represent the study sites whose variation of the retracked gates are large, which may indicate the need of retracking.

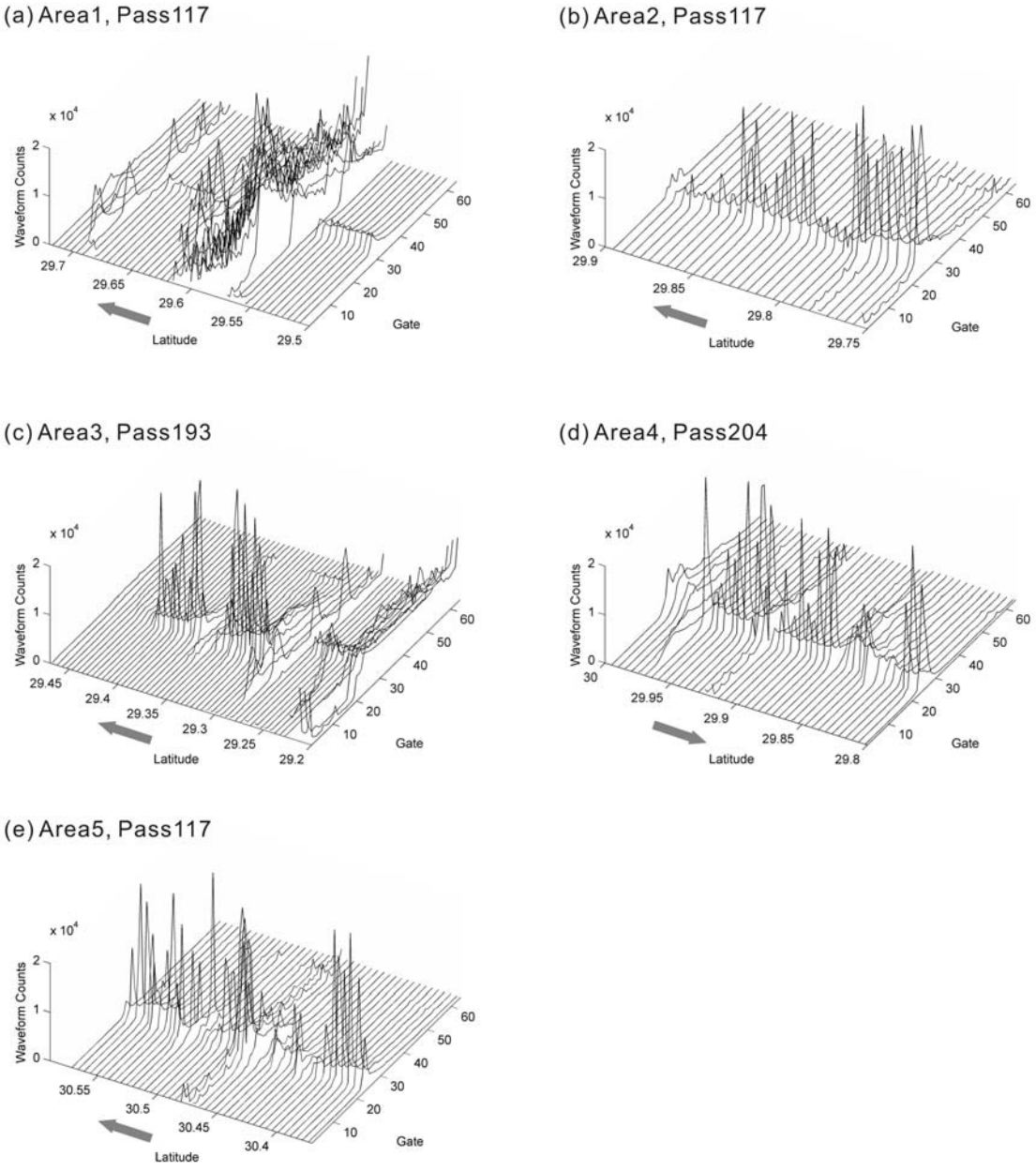

Figure 4.5: Variations of waveform shapes along satellite ground track from cycle 49. The high-peaked specular responses may indicate the presence of calm water in vegetated wetland. The arrow beside the axis of latitude indicates the direction of the satellite flight along the ground track.

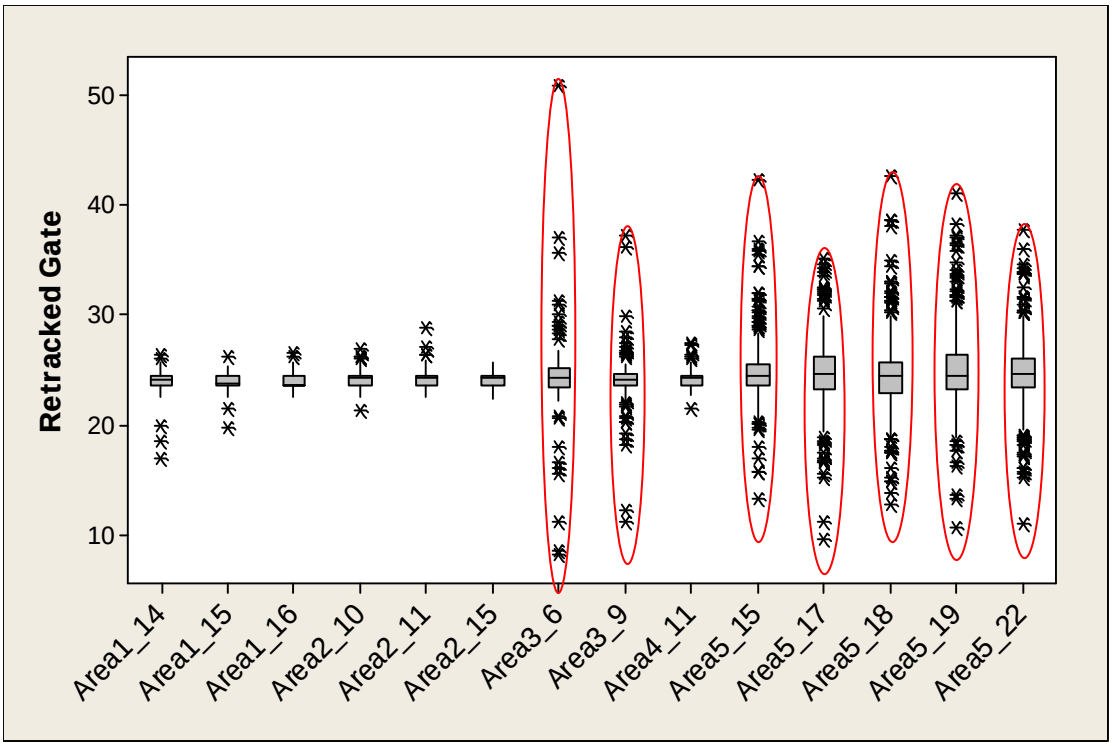

Figure 4.6: Boxplot of retracked gates obtained from OCOG retracker. Area1_1 means the southernmost 10-Hz stackfile bin of Area1, Area1_2 means the next 10-Hz stackfile bin of Area1, and so on. Area3_6, Area3_9, Area5_15, Area5_17, Area5_18, Area5_19, and Area5_22 (marked with red ellipses) show larger variation of retracked gates than other study sites. The study sites with larger variations of retracked gates showed higher correlation coefficient and smaller RMS differences between TOPEX and river gauge water level time series after applying retracking (see Figure 4.7).

To see the feasibility of retracking, the correlation coefficient (CC) and root-mean-square (RMS) difference between the water level time series from TOPEX and the nearby river gauge are examined. Original river gauge data is daily measurements whereas TOPEX data sampling interval is 10 days. Therefore, each river gauge measurement of which time tag is closest to that of the TOPEX 10-day repeat measurement is selected to compute CC and RMS differences. Figure 4.7 shows the comparison between the water level time series constructed from TOPEX and river gauge measurements over study sites Area3_6, Area3_9, Area5_15, Area5_17, Area5_18, Area5_19, and Area5_22 before and after applying retracking. As expected, while the study sites with smaller variation in the position of the retracked gate showed no significant improvement after applying retracking, the study sites with larger variation in the waveform leading edge position show higher correlation coefficients and smaller RMS differences after applying

retracking. Hence, it can be concluded that the possible need for retracking should be checked for inland hydrologic application of satellite radar altimetry, especially over vegetated wetlands. From Figure 4.8 (i)s, the spatial variation of CC can be observed, and it can be noted that CCs of the 10-Hz stackfile bins which are geographically close to the river gauge are not necessarily high, which may indicate the complex nature of the wetland water flow dynamics, as can be seen from Figure 4.8 (a)(i) and (b)(i). In Area3 (Figure 4.8 (c)(i)), the 10-Hz stackfile bin which is closest to the Mississippi River shows the highest CC after retracking. It is also interesting to note that Area5 (Figure 4.8 (e)(i)), whose vegetation type is swamp forest, show generally high correlation coefficients, which indicate the capability of Ku-band satellite radar altimeter to measure changes in water level beneath the tree cover. According to Lu et al. (2005), whose study area is located in downstream of the Atchafalaya River, the swamp forests are composed of moderately dense trees ranging from 10 to 25 m in height with a medium-low canopy closure. Due to the fact that the vegetation type of Area5 and the study area of Lu et al. (2005) are classified to be the same as “Wetland Forest Deciduous”, it can be concluded that Ku-ban altimetry can penetrate through 20-50% tree cover (see Figure 1 (c) of Lu et al..(2005)).

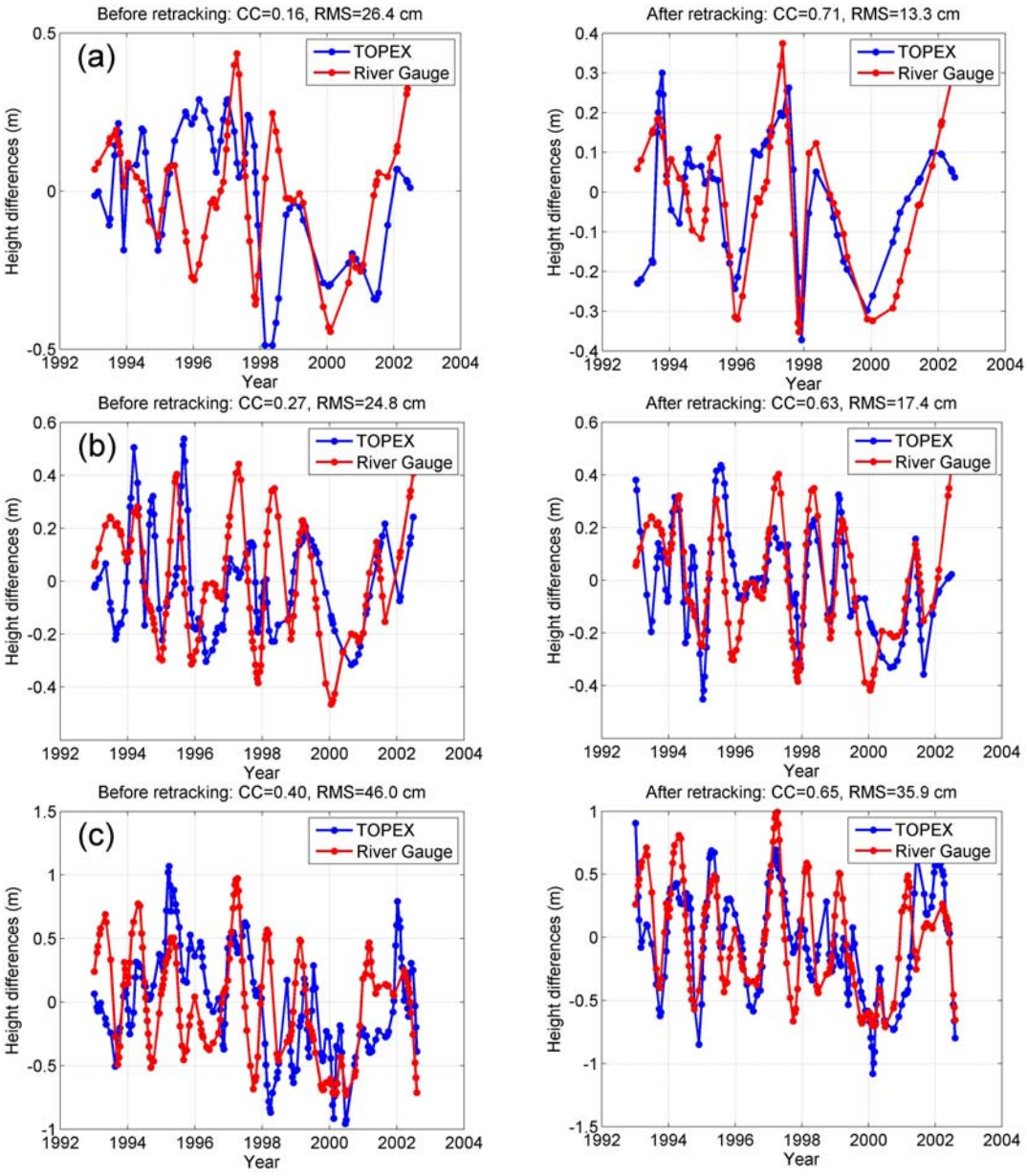

Continued

Figure 4.7: Comparison of TOPEX and nearby river gauge water level time series before and after retracking over (a) Area3_6, (b) Area3_9, (c) Area5_15, (d) Area5_17, (e) Area5_18, (f) Area5_19, and (g) Area5_22, respectively. Note that higher correlation coefficient and smaller RMS differences are obtained after retracking.
Figure 4.7 continued

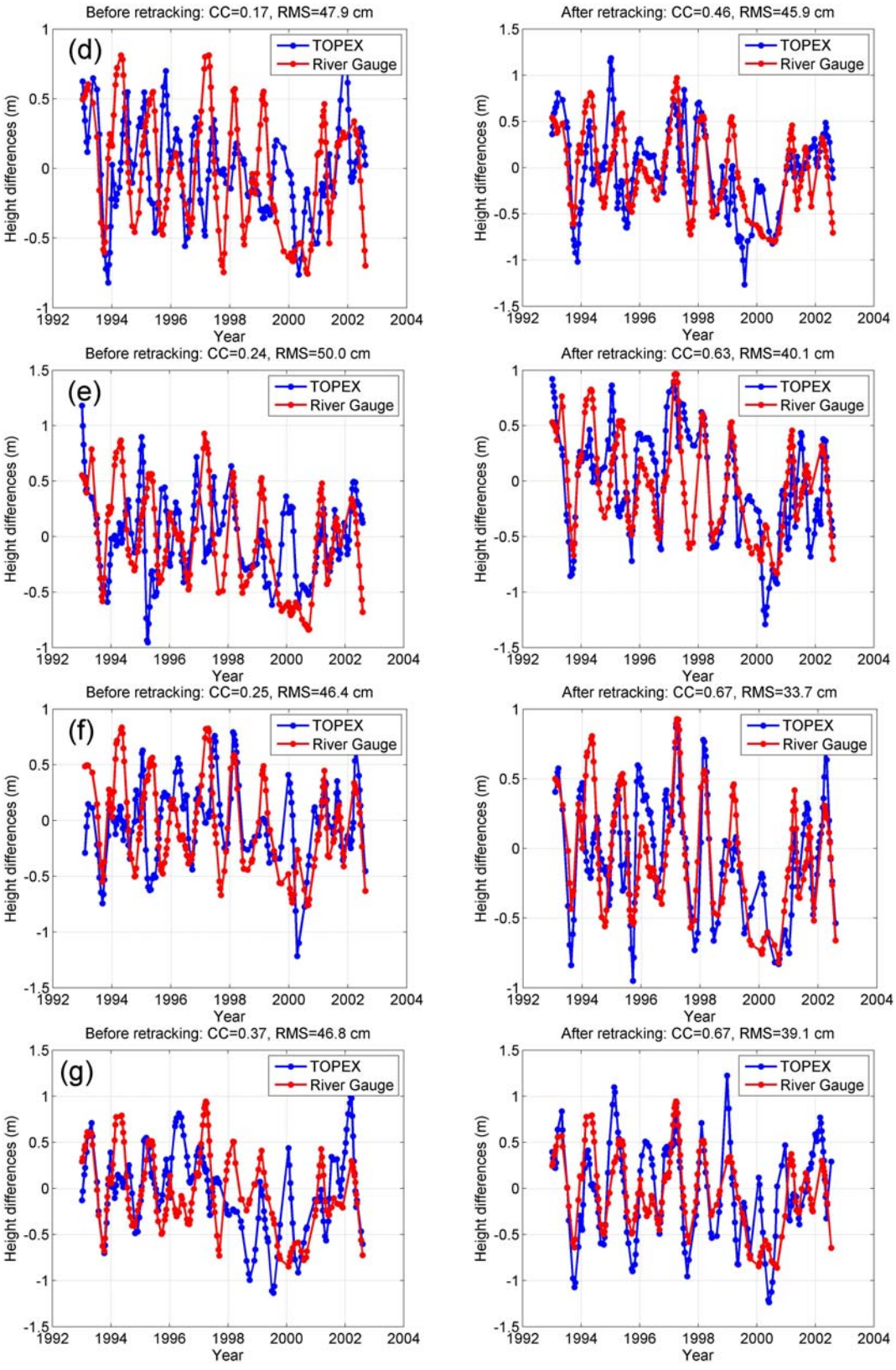
Before retracking: CC=0.17, RMS=47.9 cm
After retracking: CC=0.46, RMS=45.9 cm
(d)
Before retracking: CC=0.24, RMS=50.0 cm
After retracking: CC=0.63, RMS=40.1 cm
(e)
Before retracking: CC=0.25, RMS=46.4 cm
After retracking: CC=0.67, RMS=33.7 cm
(f)
Before retracking: CC=0.37, RMS=46.8 cm
After retracking: CC=0.67, RMS=39.1 cm
(g)
TOPEX
River Gauge
Height differences (m)
Year

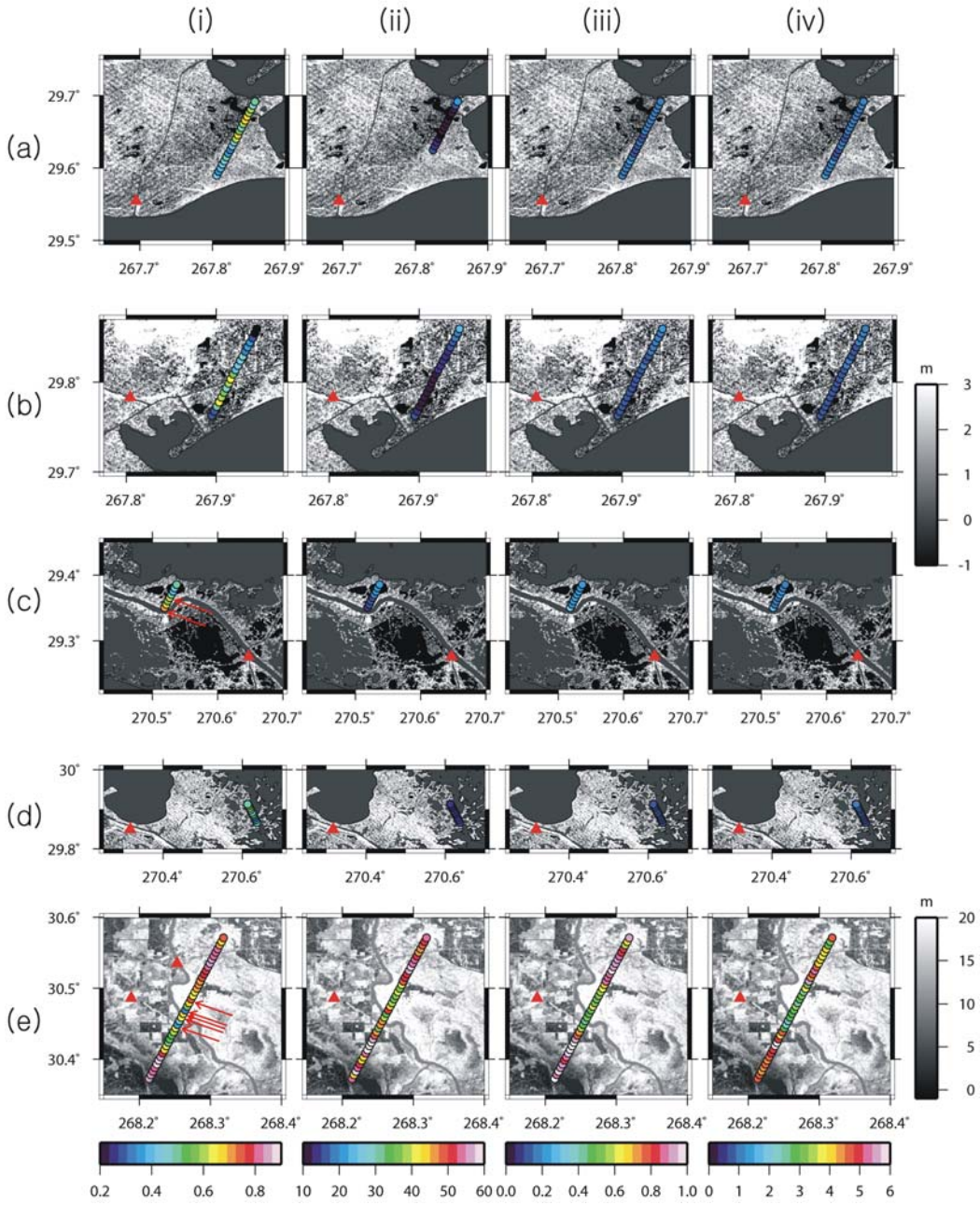

Figure 4.8: (i) Correlation coefficients and (ii) RMS differences (cm) between TOPEX and nearby river gauge (red triangle) water level time series, (iii) stand deviations (m) and (iv) peak-to-peak amplitudes (m) of the TOPEX water level time series over each 10-Hz stackfile bin. The stackfile bins, which showed improvement after retracking are indicated by red arrows. Background is the SRTM C-band DEM.

4.3 Results

In Area5, there are two river gauge stations which have records contemporary to those of TOPEX. The Krotz Spring is located directly at the Atchafalaya River channel, and Bayou Fordoche is located southwest of the Krotz Spring (Figure 4.8 (e)(i)). As can be seen from Figure 4.9, the amplitudes of the seasonal variation between the time series from Krotz Spring and Bayou Fordoche differ significantly and the amplitude of TOPEX time series is closer to but a little larger than that of Bayou Fordoche, for example, over study site Area5_1. The RMS differences between the time series from Krotz Spring and TOPEX, and Bayou Fordoche and TOPEX are 117.7 cm and 52.9 cm, respectively. On the other hand, it is also observed that the phase of the seasonal water level variation from Krotz Spring, Bayou Fordoche, and TOPEX agree very well. Correlation coefficients between Krotz Spring and TOPEX, and Bayou Fordoche and TOPEX are 0.83 and 0.85, respectively. Hence, the TOPEX time series obtained from each 10-Hz stackfile bin really follows the seasonal variation of the water level change, and the amplitude also agree well with the Bayou Fordoche, not Krotz Spring, which is located at the main stream of the Atchafalaya River.

The spatial variation of AGC and PP values over Area5 have been shown in Figure 4.4 (e)(i) and (e)(ii), respectively. It can be seen that the AGC values are higher over southern part of Area5, and then starts to decrease near the river channel and remain almost constant. On the other hand, the PP values are also higher over the southern part of Area5, and then decrease around the river channel. Unlike the AGC values, the PP values increase again around northern part of Area5. As discussed in Chapter 4.2.1, both the AGC and PP values can be used to detect “water-covered” surfaces, and thus higher AGC and/or PP values may represent more flooded surface condition. In other words, the water level fluctuation over the southern part of Area5 can be larger than that over the northern part.

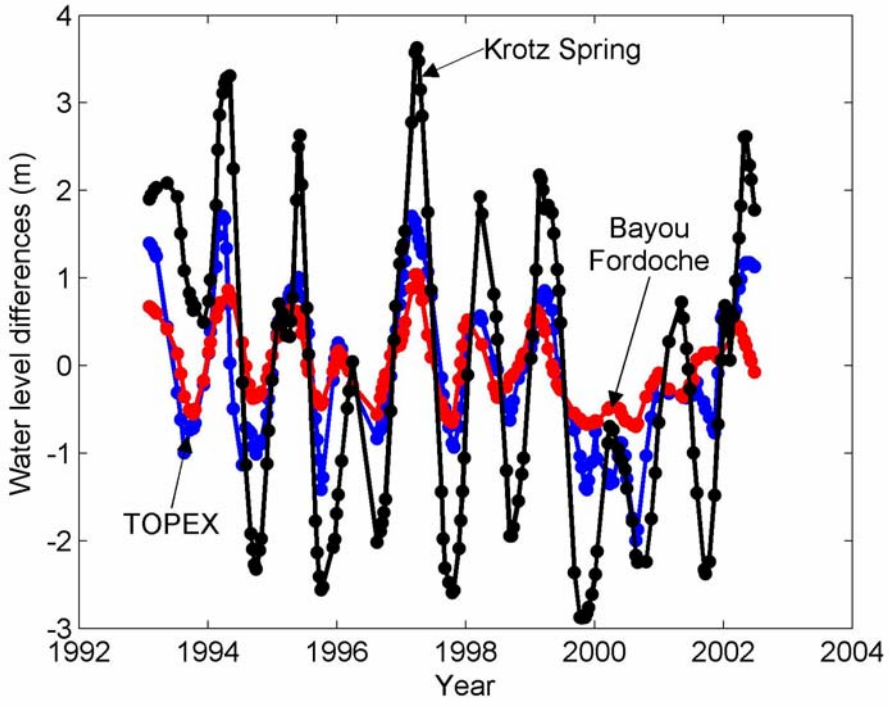

Figure 4.9: Water level time series obtained over the study site Area5_1 from Krotz Spring stage (black), Bayou Fordoche stage (red), and TOPEX (blue), respectively.

To validate the speculation, the SRTM C-band DEM elevation is plotted in Figure 4.10 along with the AGC and PP values over each 10-Hz stackfile bin from south to north. From the SRTM elevation, it is clear to see the higher river banks on both sides of the Atchafalaya River, and the southern part has lower elevation than the northern part. Therefore, more flooded water can be filled in southern part than the northern part, which resulted in higher AGC and PP values. Next, the standard deviations and the peak-to-peak amplitudes of decadal TOPEX water level time series, the indicators of water level fluctuation, over each 10-Hz stackfile bin are examined. As can be seen from Figure 4.11, both the standard deviations and the amplitudes of the 10-Hz TOPEX water level time series over the southern part are higher than those over the northern part. This demonstrates that the southern portion of Area5, which is located at the northern part of the swamp forest along the Atchafalaya River basin, is more flooded than the northern portion. However, it should be noted that this can be a local phenomenon only around Area5. This can be seen from the L-band Advanced Land Observing Satellite (ALOS) Synthetic Aperture Radar (SAR) geocoded intensity image, which is taken on Jan 29, 2007, shown in Figure 4.12. According to Hess et al. (2003), the higher values in the L-band SAR intensity image may represent more flooded surface characteristics. It can be seen that the red-circled part shows higher intensity value than the blue-circled part, which agrees with the conclusion above.

(a)

(b)

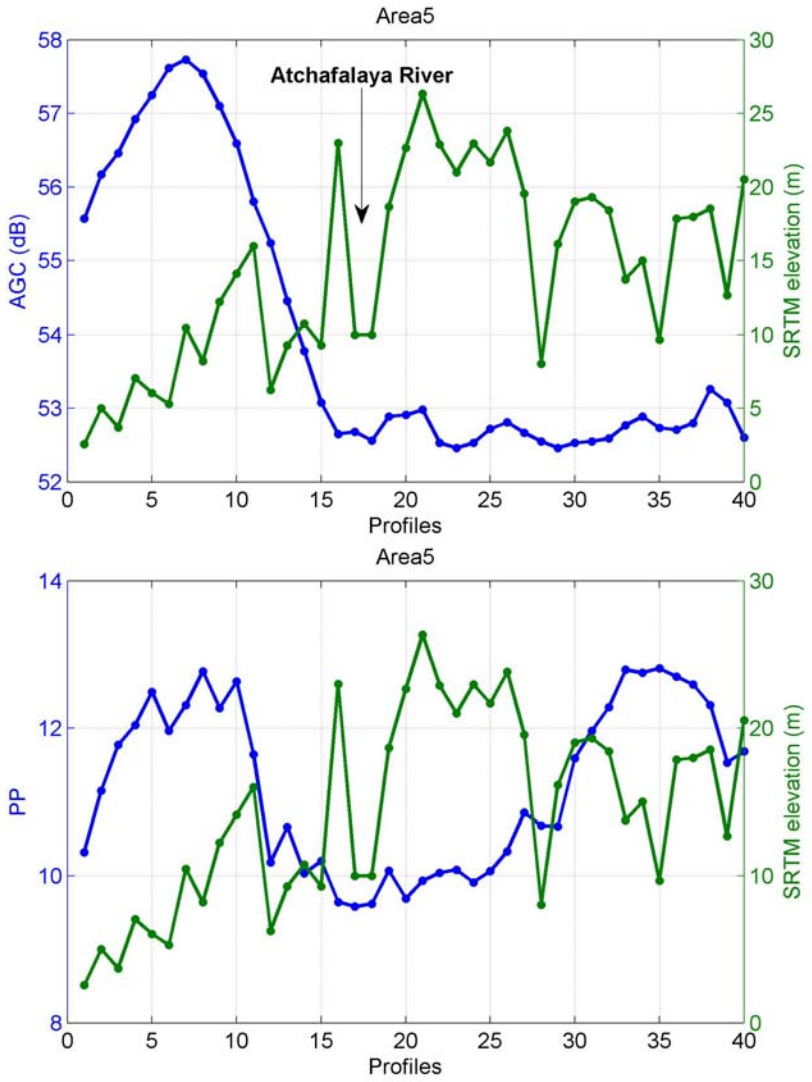

Figure 4.10: (a) AGC (dB), and (b) PP values and SRTM elevation along each 10-HZ stackfile bin over Area5, respectively.

(a)

(b)

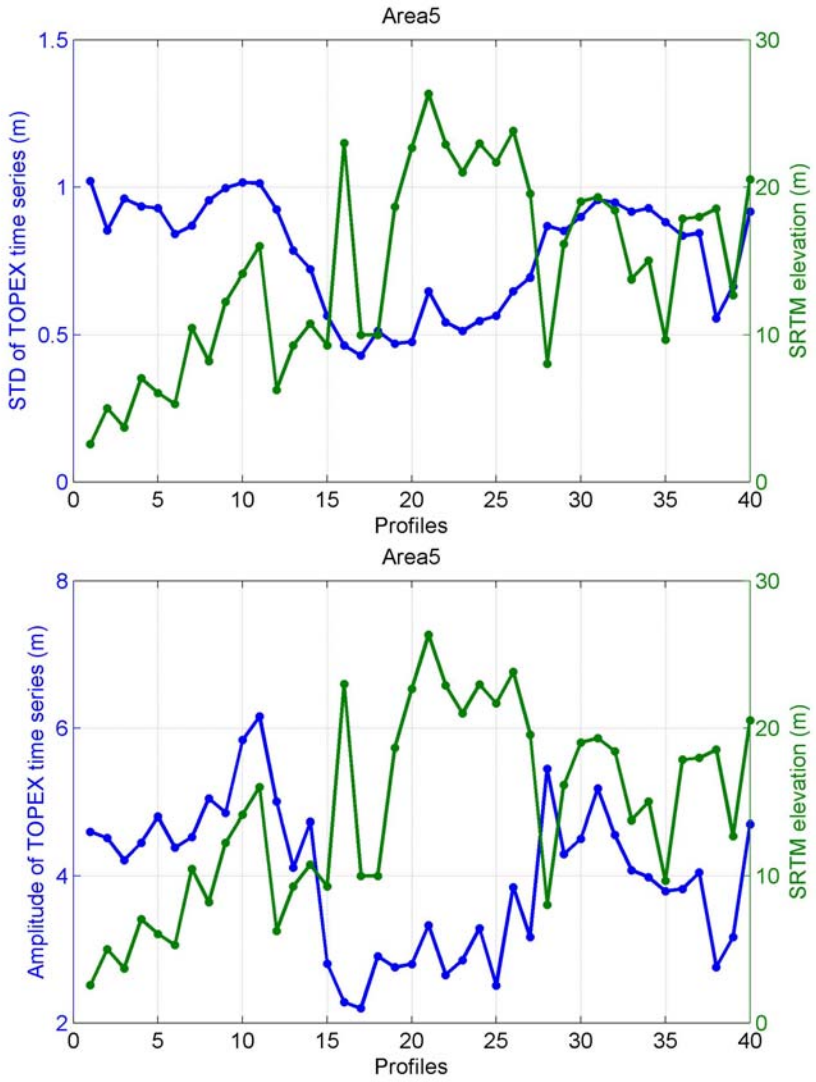

Figure 4.11: (a) standard deviation (m), and (b) peak-to-peak amplitude (m) of TOPEX (blue lines) time series and SRTM (green lines) elevation along each 10-HZ stackfile bin over Area5, respectively.

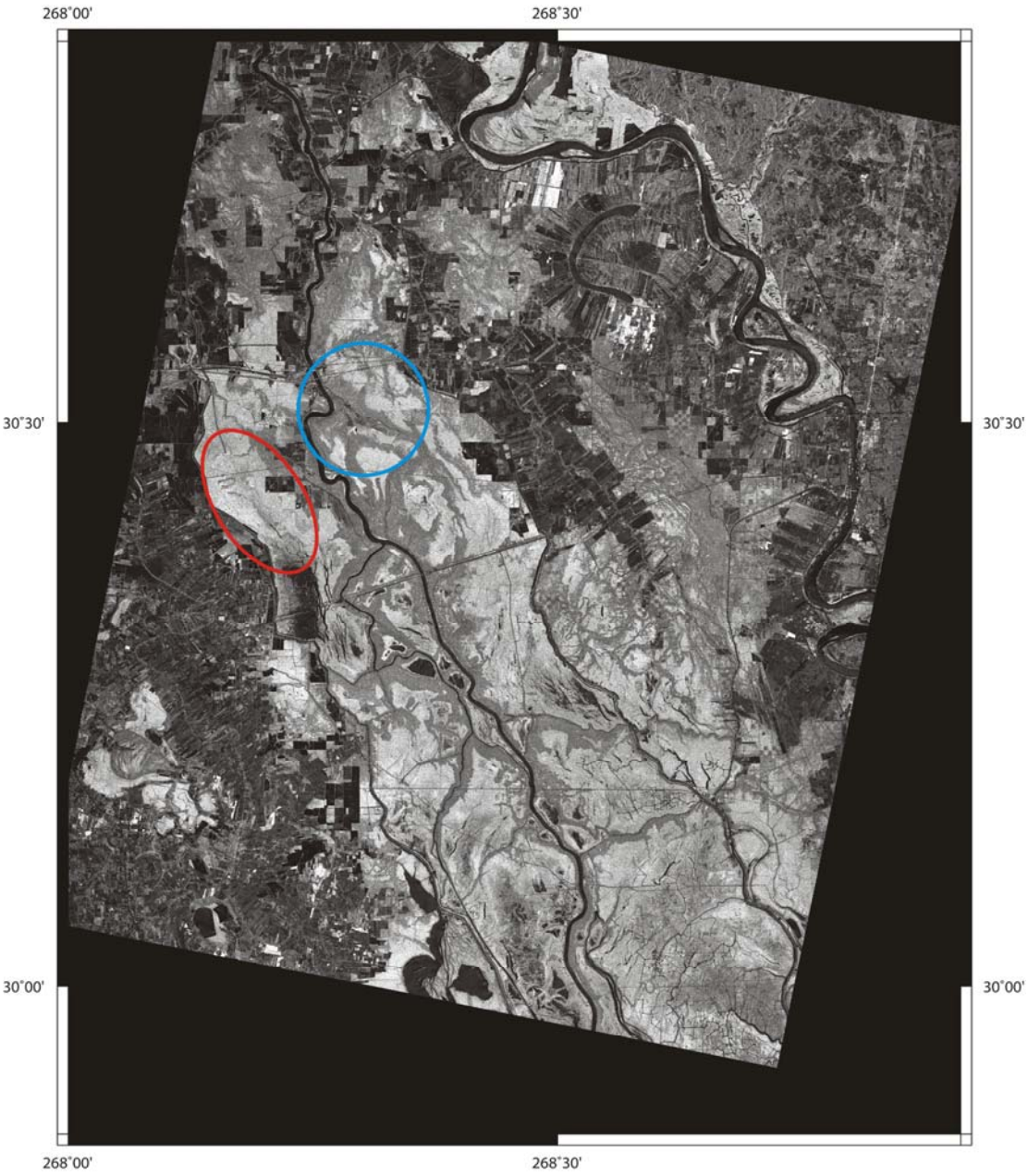

Figure 4.12: L-band ALOS SAR geocoded intensity image taken on Jan 29, 2007. The more flooded part in Area5 is marked as red circle, and the partially flooded part is marked as blue circle.

4.4 Conclusion

An innovative technique to estimate the water level variation using TOPEX radar altimetry in Louisiana wetlands is presented. The 10-Hz stackfile procedure is used to map the water level change over each of the 10-Hz stackfile bin with the highest spatial resolution (~660 m) achievable from TOPEX. This is different from the previous studies (Birkett, 1998; Birkett et al., 2002; Maheu et al., 2003) which spatially averaged the 10-Hz measurements along the satellite track and river/wetland intersections, allowing only one time series per intersection. Furthermore, the need for retracking over vegetated wetlands is examined by computing the retracked gates and comparing the water level time series from TOPEX and river gauge before and after applying retracking. Study sites, which showed better agreement with the nearby river gauges, are located near the Mississippi River delta (Area3_6 and Area3_9) and around the swamp forest (Area5_15, Area5_17, Area5_18, Area5_19, Area5_22). Most of the study sites, which did not show improvement after retracking, are distributed around the brakish marsh which has relatively low canopy.

None of the study areas showed higher correlation coefficient between the time series from TOPEX and river gauge as the 10-Hz stackfile bins become closer to the river gauge station, which may indicate the complex nature of the wetlands flow dynamics due to the levees, dredging, impoundment, etc. Furthermore, it has been shown that the flooding characteristics over the both sides of the Atchafalaya River in Area5 are different, and the cause has been explained using the SRTM DEM elevation.

These observations could help quantify the depletion or rise of water level in wetlands and the precise estimate of water storage over wetlands. These observations can also be used to improve the hydrological modeling by providing large-scale calibration data sets to precisely estimate hydrological parameters for numerical modeling. Improving hydrological modeling is a critical step to enhance prediction and assessment capabilities for future flood events over wetlands. On the other hand, the along-track gradient of water level from the 10-Hz TOPEX stackfile could potentially determine the direction of water flow.

For a possible future study, other satellite radar altimeters could be used to enhance the spatial coverage and data time span, for example, by constructing 18-Hz stackfile using Envisat GDRs although it has shorter time span from 2002 to present. Another possible study is to estimate the vertical crustal motions, the subsidence in Louisiana wetlands, at river gauge stations by combining the TOPEX-driven geocentric water level measurements and the long-term relative water level records from river gauges using a stochastic adjustment model (Kuo et al., 2004, 2008).

CHAPTER 5

ICE MASS BALANCE STUDIES OVER THE AMUNDSEN SEA SECTOR, WEST ANTARCTICA

5.1 Introduction

The current Antarctic ice sheet contains ~90% of the world's ice (or ~70% of the world's fresh water), thus by far the largest fresh water reservoir on Earth. Some 98% of Antarctica is covered by ice sheets of at least ~1.6 km thick, and complete melting of this ice would raise the global sea-level by 56.6 m. The present-day Antarctic ice sheet covers an area of ~12.3×10^6 km^2, with an ice volume of 24.7×10^6 km^3 (Lythe et al., 2001), representing approximately half of its size at the LGM (~21,000 years ago; e.g., Bentley, 2004). It is plausible that the ice sheets contributed little to sea-level rise during the 20th century (Cazenave et al., 2006; Wingham et al., 2006a); however, there exists evidence of accelerated thinning of the margins of the Greenland and West Antarctic ice sheets over the past decade, attributable to anthropogenic warming (Alley et al., 2005; Lemke et al., 2007; Shepherd and Wingham, 2007; Vaughan, 2005).

Satellites and airborne sensors provide most of the contemporary continent-wide observations for *recent* ice sheet mass balance estimates and their contributions to present-day sea level rise. However, large uncertainties exist in estimates of the Antarctic ice mass balance and its present-day contributions to global sea level rise. Estimates of the sea-level change attributed to melting of the Antarctic ice sheet range from –0.12 to 0.17 mm/year (Davis et al., 2005; Thomas et al., 2004; Wingham et al., 2006a; Zwally et al., 2005), based on InSAR and decadal satellite radar altimetry; estimates based on GRACE data range from 0.14 to 0.52 mm/year (Chen et al., 2006; Ramillien et al., 2006; Velicogna and Wahr, 2006a) (see Table 1 of Shum et al. (2008)). It should be noted that the GRACE data reported in the literature spans a period of only 3 years (2002–2005), and thus these estimates could be contaminated by interannual or longer periodic variations. The discrepancy between these estimates possibly reflects the fact that the satellite measurements used span a period of just 15 years. In addition to these possible measurement errors, plausible geophysical explanations include (1) the intrusion of warm water deep beneath the Antarctic floating ice shelves which may cause collapse of the ice shelves or the formation of polynas (Jacobs et al., 1992; Shepherd et al., 2004); (2)

potential ice-sheet instability due to the dynamics of large sub-glacial lakes resulting from faster flowing ice streams from accelerated melting (Bell et al., 2007; Fricker et al., 2007; Wingham et al., 2006a); (3) ice-shelf buttressing/sedimentation that acts to stabilize ice-sheet grounding lines (Alley et al., 2007; Anandakrishnan et al., 2007; Dupont and Alley, 2005); (4) glacial dynamics leading to ice-sheet instability (Shepherd and Wingham, 2007); and (5) geodynamic processes arising from interaction between ice and solid Earth due to GIA (Ivins and James, 2005) and due to present-day ice melting (elastic deformation), resulting in the deformation of the sub-glacial topography (Ivins et al., 2002).

The satellite radar altimetry has been used to directly measure the net mass change from the ice sheet elevation-change measurements (Zwally et al., 1989; Wingham et al., 1998; Davis et al., 2005; Helsen et al., 2008). While Wingham et al. (1998) analyzed the European Remote Sensing 1 and 2 (ERS-1/2) satellite altimetry data from 1992-1996 over Antarctica, and found the average elevation change to be -0.9 ± 0.5 cm/year, Davis et al. (2005) reported a slight thickening overall at a rate of 1.4 ± 0.3 cm/year due to the thickening of the East Antarctic ice sheet at the rate of 1.8 ± 0.3 cm/year based on decadal ERS-1/2 altimetry observations from 1992-2003. The previous studies computed the ice sheet elevation changes (dH) at satellite crossover points in order to minimize the topographic induced errors, i.e., to circumvent the surface gradient problem. However, the crossover analysis limits the number of measurements. The collinear analysis can provide as many as 100 times more individual measurements over Antarctica, and enhance the spatial resolution to study local scale phenomena (Legresy et al., 2006). Furthermore, in case of European Space Agency (ESA) altimeters such as ERS-1/2 and Envisat which are equipped with linearly polarized antenna, a systematic difference as large as a few meters at crossover points exists (Wingham et al., 1998), which causes difficulties and limitations for the crossover analysis. This is modulated by the angle between the antenna polarization and the direction of the anisotropy of the reflecting surface (Remy et al., 2006). Clearly, this complex and least understood errors could potentially be subtracted by employing the collinear analysis.

The West Antarctic ice sheet contains enough water to raise global sea level by several meters if the ice were to completely melt (Warwick et al., 1996; Shepherd et al., 2002). Much of the West Antarctic ice sheet is characterized as a “marine ice sheet” with its bed well below sea level (Rignot et al., 2002). Hence, glaciers flowing into the Amundsen Sea (Figure 5.1) would float free from the bedrock, potentially easing resistive forces acting on upstream ice and thus leading to further glacier acceleration (Thomas et al., 2004). Furthermore, it has been known that the ice shelf melting in the Amundsen Sea is driven by warm circumpolar deep water (CDW) intrusions onto the continental shelf (Rignot et al., 2008). The Amundsen Sea sector (or basin G-H), one of the three major West Antarctic ice sheet drainage systems, contains enough ice to raise sea level by 1.3 m (Rignot, 2001), and has been observed to be the place of the largest ice mass loss in Antarctica (Helsen et al., 2008; Rignot et al., 2008).

In this chapter, the ice sheet elevation change (dH/dt) has been estimated over the

Amundsen Sea sector using Envisat altimeter data from 2002-2008 using the collinear analysis which is developed to estimate the vertical motion over the Hudson Bay land region in Chapter 3. The estimated ice mass loss is then compared with that using gravity variations observed by the GRACE twin-satellite mission from April 2002 - December 2007 and with other studies.

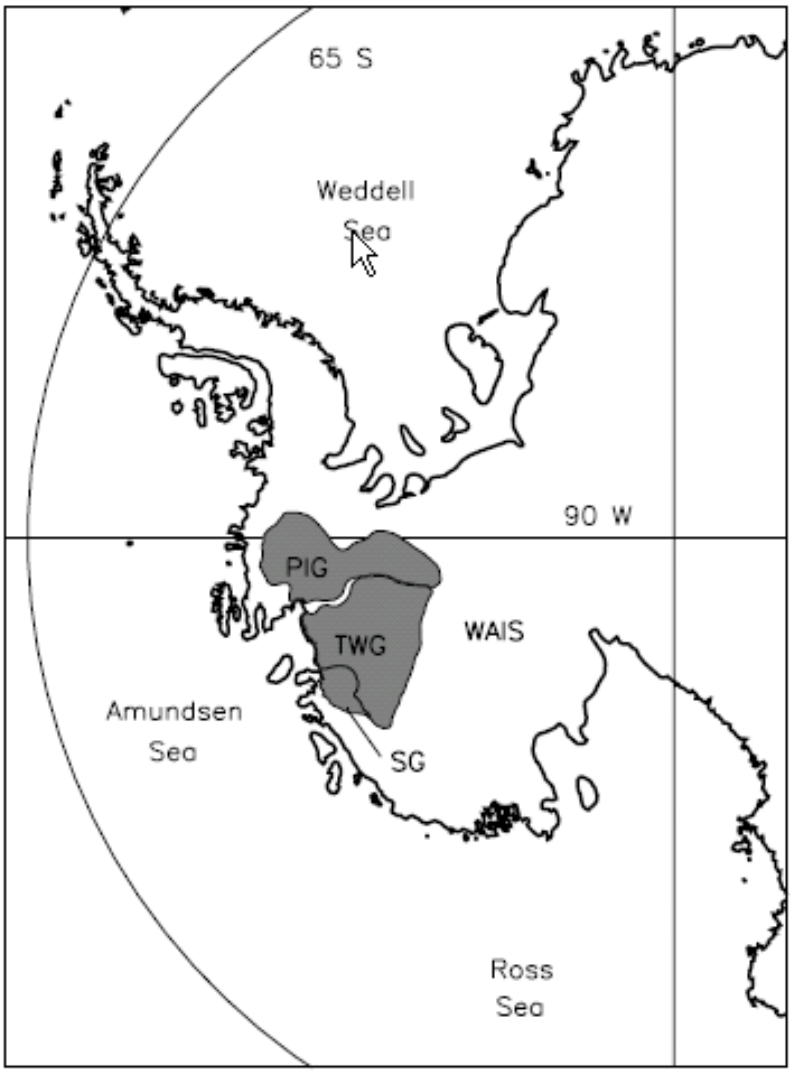

Figure 5.1: The location of the Pine Island, Thwaites, and Smith glacier drainage basins that form the Amundsen Sea sector (after Shepherd et al., 2002, Fig. 1).

5.2 Ice Sheet Elevation Change over the Amundsen Sea Sector

Envisat altimeter data used in this study are from the periods September 2002 to May 2007. This extends the previous Antarctic elevation change results from May 1992 to May 2003 using ERS-1/2 (Davis et al., 2005). The Envisat orbits on a 35-day repeat cycle with 98.5˚ inclination. The Envisat GDR data contain 18-Hz (twenty-per-frame), corresponding to a ground spacing of approximately 350 m, high-rate retracked range measurements using four different retracking algorithms. They are Ocean (Brown, 1977), Ice-1 (Bamber, 1994), Ice-2 (Legresy et al., 2005), and Sea ice (Laxon, 1994) retrackers. In this study, the retracked measurements using the Ice-1 retracker, which is optimised for general continental ice sheets, are used (D. Wingham, personal communication, 2008). Additionally, the 5.6 m level Ultra Stable Oscillator (USO) anomalies from cycles 44-56 were corrected using the ESA's correction tables.

The Envisat 18-Hz regional stackfile over the Amundsen Sea sector is created by the similar procedure as described in Chapter 3.2. The only difference is that the latitudes of the 18-Hz stackfile bins are computed by linearly interpolating the latitudes of the 1-Hz stackfile bins. A new Antarctic DEM on 1 km grids that combines Ice Cloud and land Elevation Satellite (ICESat) and ERS geodetic phase data (Bamber and Gomez-Dans, 2005; data courtesy, J. Bamber) is used to correct the surface gradient problem as described in Chapter 3.5. The DEM is also used as a mean surface profile to calculate the ice sheet surface anomalies.

The ice sheet surface anomalies at each 1-Hz stackfile bin are computed by averaging ten surface anomalies at 10-Hz stackfile bins per each cycle. The ice sheet elevation differences (dH) are then computed at 1-Hz stackfile bins from the averaged ice surface anomalies. The ice sheet elevation change time series are computed for individual 1˚ × 1˚ regions covering 80˚S to 74˚S and 240˚E to 270˚E by averaging the elevation differences (dH). After time series are generated for the 1˚ × 1˚ regions, a composite time series is generated for the Amundsen Sea sector by averaging all region time series in the drainage basin.

Additionally, time series of backscatter coefficient change $(d\sigma_0)$ are also generated for the 1˚ × 1˚ regions using the same procedure which produced the elevation change (dH) time series. The purpose is to check whether spurious elevation changes occur due to the backscatter coefficient changes (Wingham et al., 1998; Davis and Ferguson, 2004). According to Wingham et al. (1988) and Davis and Ferguson (2004), a high degree of correlation between the elevation changes (dH) and the backscatter coefficient changes $(d\sigma_0)$ exists for many regions in Antarctica. When the scattering properties of the ice sheet surface changes with time, significantly different waveforms can be obtained which produce different elevation changes (Davis and Ferguson, 2004). Hence, this correlation can introduce spurious elevations changes and they have to be adjusted by subtracting the product of the correlation gradient (CG) and the power change $(d\sigma_0)$ for each grid cell such as (Davis and Ferguson, 2004):

$$dH_{corrected(i)} = dH_i - d\sigma_i \cdot CG \tag{5.1}$$

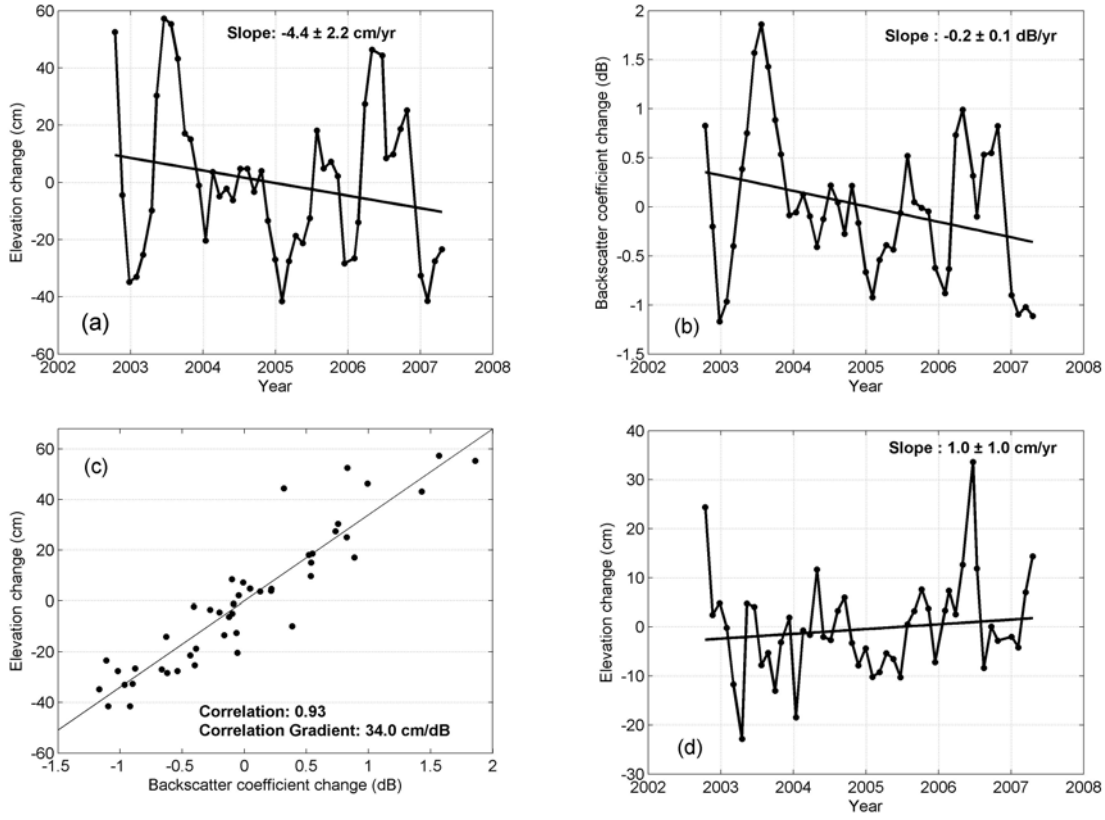

Figure 5.2: Envisat elevation change time series for 1˚ × 1˚ region whose centre coordinate is 79.5˚S, 242.5˚E. (a) Unadjusted elevation change time series. (b) Backscatter coefficient change times series. (c) Scatter plot showing correlation between dH and $d\sigma_0$. (d) Adjusted elevation change time series.

In Figure 5.2 (a) and (b), it can be seen that the seasonality and the linear trend of the elevation time series are dominated by the correlation between dH and $d\sigma_0$ time series. The linear trend in the dH time series has changed from -4.4 cm/year to +1.0 cm/year because the negative linear trend in the $d\sigma_0$ time series is responsible for the negative linear trend in the unadjusted dH time series (Davis and Ferguson, 2004).

Both CG and the correlation coefficient (CC) have spatial variability over the ice sheet, which are shown in Figure 5.3. Unlike Shepherd et al. (2002) who found no correlation between dH and $d\sigma_0$ time series in the Amundsen Sea sector, about 9% of individual regions had correlation values larger than 0.7. Although majority of the regions does not show the correlation, the adjustment is applied to each region time series regardless of the magnitude of the correlation because regions with small CC also show small CG with some exceptions (Davis and Ferguson, 2004). This is can be seen in Figure 5.4 which shows the least squares fit to the scatter points nearly passes through the origin. In case of generating the basin time series, e.g. over the Amundsen Sea sector in this study, the effect of the adjustment to the linear trend of the time series might be negligible (Davis and Ferguson, 2004).

(a)

(b)

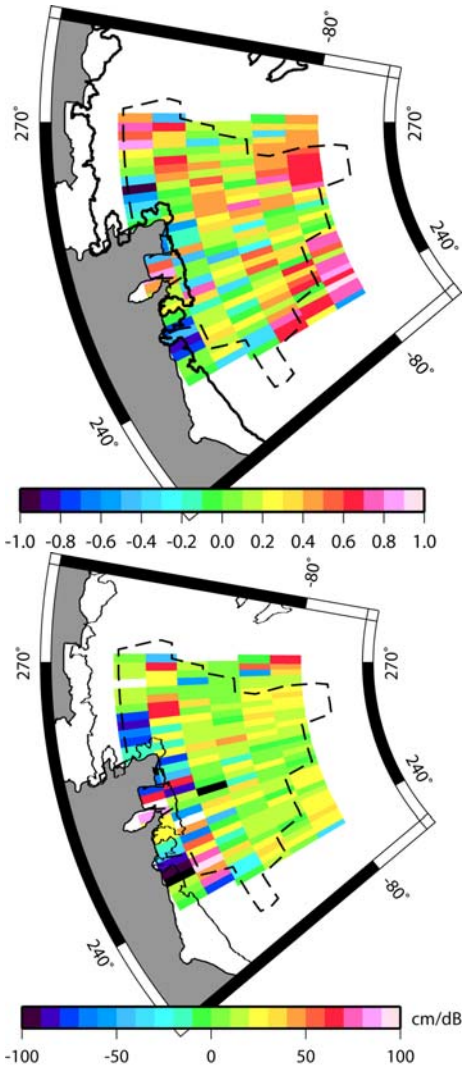

Figure 5.3: Spatial variations of (a) correlation coefficient (CC) between dH and $d\sigma_0$ time series and (b) correlation gradient (CG) over each 1˚ × 1˚ region. The solid line represents the ground line and the dashed line shows the Amundsen Sea sector.

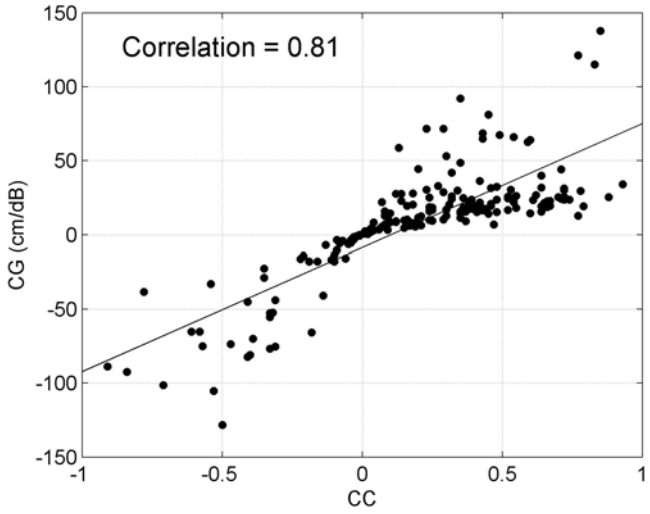

Figure 5.4: Scatter plot of correlation coefficient (CC) and the correlation gradient (CG) in individual 1˚ × 1˚ region.

Figure 5.5 shows the spatial distributions of the standard deviations of the Envisat time series from September 2002 to May 2007 for all 1˚ × 1˚ regions before and after the surface gradient correction using the Antarctic DEM. It is clear to see that the spurious height changes caused by the satellite orbital drift are reduced overall after the gradient correction. It is also interesting to note that the 1˚ × 1˚ regions which have high standard deviation values near the coast show almost uniform reduced standard deviations after the correction. Histograms shown in Figure 5.6 further demonstrated the feasibility of applying the gradient correction using the DEM because the count values on the y-axis have increased for <1 m histogram bins.

(a)

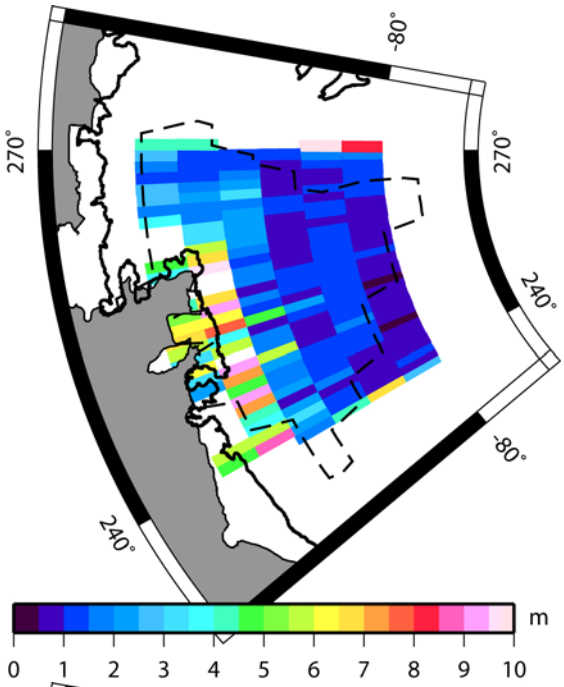

(b)

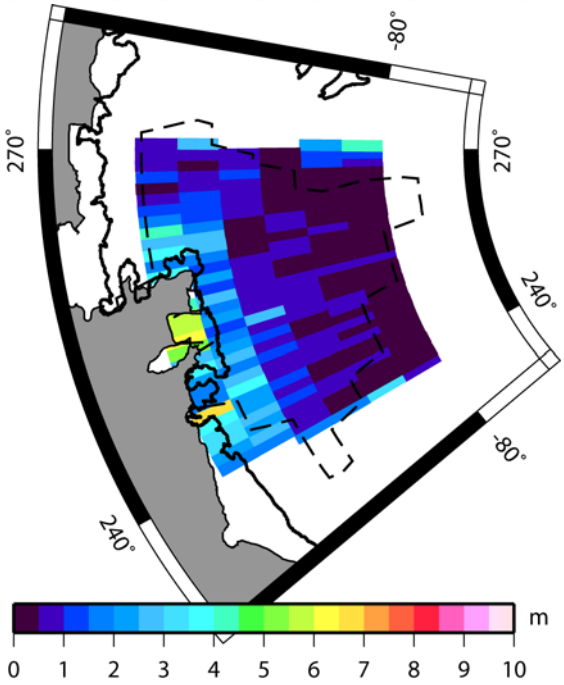

Figure 5.5: Spatial distributions of the standard deviations of the Envisat time series from September 2002 to May 2007 for all 1˚ × 1˚ regions (a) before and (b) after the surface gradient correction using the Antarctic DEM.

(a)

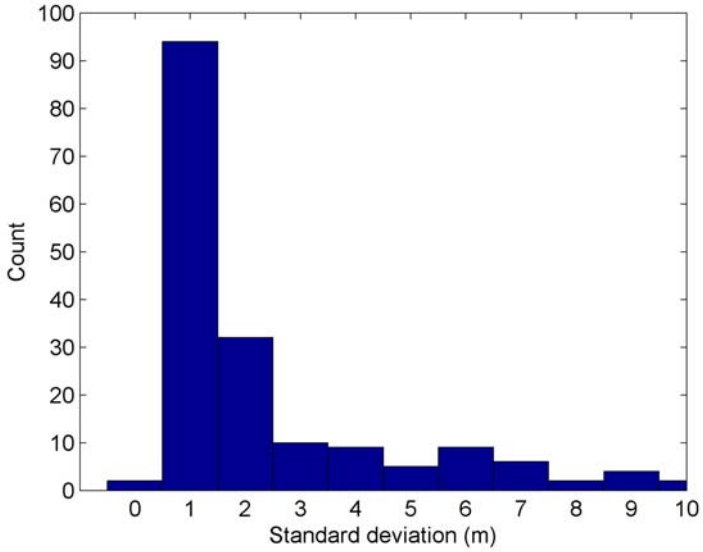

(b)

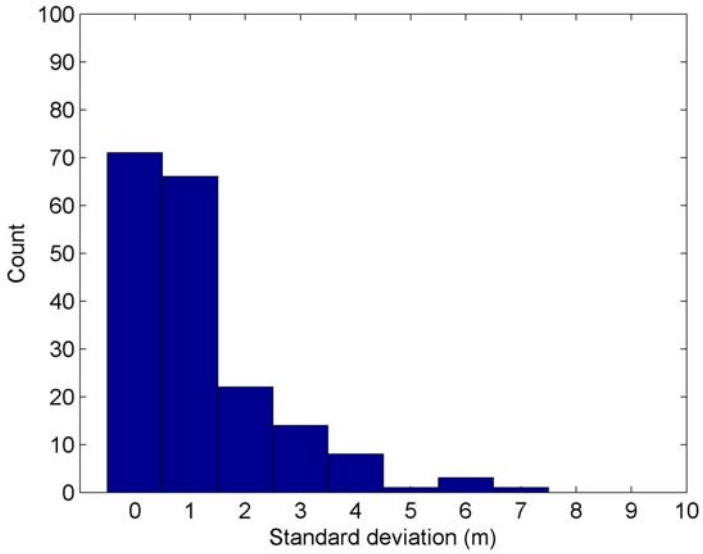

Figure 5.6: Histograms of the standard deviations of the Envisat time series from September 2002 to May 2007 for all 1˚ × 1˚ regions (a) before and (b) after the surface gradient correction using the Antarctic DEM.

Finally, the linear trend estimates are computed from each 1˚ × 1˚ region and the basinwide time series over the Amundsen Sea sector by simultaneously fitting the trend and the annual and semi-annual signals. The basinwide time series over the Amundsen Sea sector are formed using area-weighted averages of the *dH* data over each 1˚ × 1˚ region. Furthermore, basin mask from Vaughan et al. (1999) is used. The estimated linear trends are further corrected by subtracting the crustal uplift due to GIA. To be consistent with Davis et al. (2005), the subglacial topogphy vertical motion is assumed to be

isostatic uplift due to GIA, and it is forward modelled using the Ivins and James (2005) (or IJ05) model. The deformation of the subglacial topography due to present-day ice melting (elastic deformation) is not considered in this study.

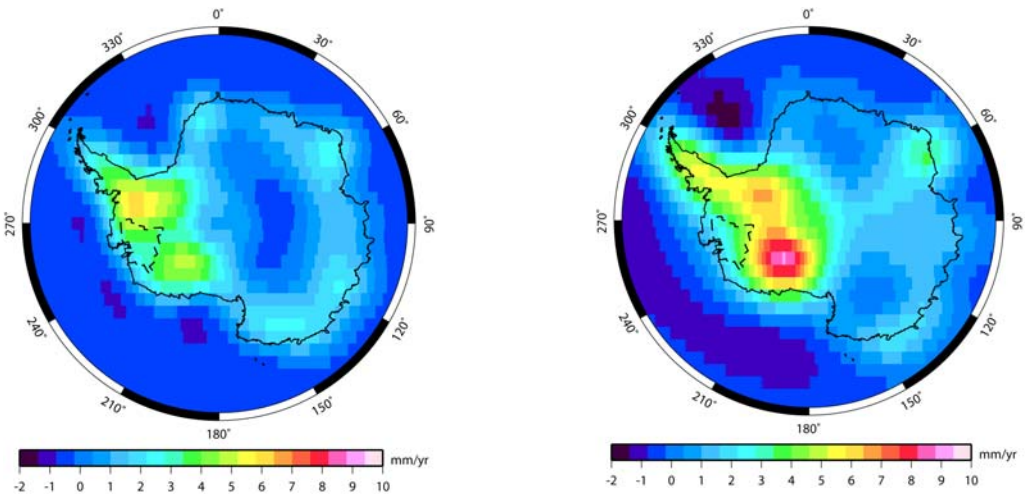

Figure 5.7: Crustal uplifts predicted from (a) IJ05 and (b) RF3S20 (β=0.4) GIA models. Basin G-H is shown with dashed lines.

Figure 5.8 shows the rate of elevation change (dH/dt) from the adjusted Envisat time series from September 2002 to May 2007 for all 1° × 1° regions. It exhibits strong negative trends near the coast, which change to positive trends in the interior regions. It also shows the strong positive trends in the area adjacent to the peninsular basins. These patterns agree well with the previous studies such as Wingham et al. (1988), Davis et al. (2005), Wingham et al. (2006a), and Rignot et al. (2008).

Figure 5.9 shows the basinwide time series before and after adjustment for backscattered power and isostatic uplift. The linear trend estimated from the basinwide time series is compared with the estimates from previous studies of Wingham et al. (1988), Davis and Ferguson (2004), Davis et al. (2005) and Wingham et al. (2006a). It should be noted that the estimated linear trends from Davis et al. (2005) and Wingham et al. (2006a) are different because of their different analysis although they used the altimeter data from the same source. For example, Wingham et al. (2006a) did not use ERS-1 data if its coverage is less than 85% of that of ERS-2 to avoid possible biasing. Table 5.1 summarizes their estimated linear trends over the Amundsen Sea sector with that estimated from this study. There is good overall agreement in the strong negative trend of about 10 cm/year, and according to Wingham et al. (2006a), 1992-2001 mean accumulation rate anomaly with respect to 1979-2001 mean accumulation rate over basin G-H is -1.9 cm/year, which means the strong negative trend in the elevation change reflect the ice mass loss, not short-term changes in snow fall, supporting the evidence of

an increase in basal melting of the Pine Island and Thwaites (Rignot and Jacobs, 2002).

(a)

(b)

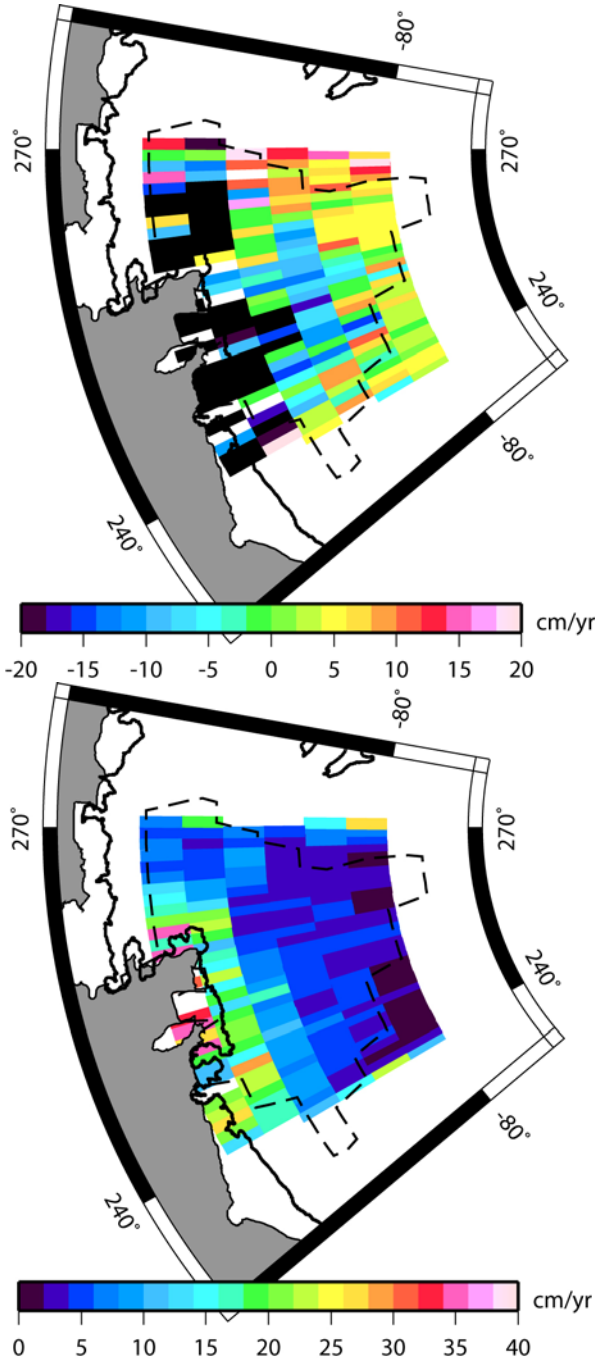

Figure 5.8: Spatial plots of (a) dH/dt trends for each region, and (b) their formal uncertainties after adjustment for backscattered power and isostatic uplift.

(a)

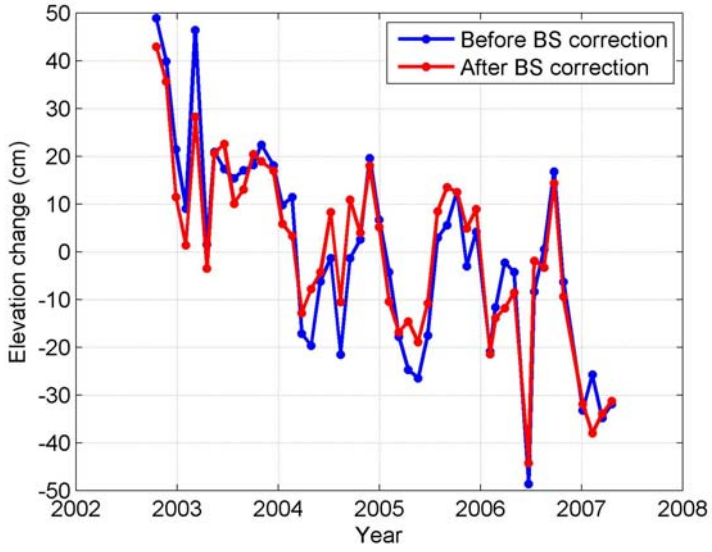

(b)

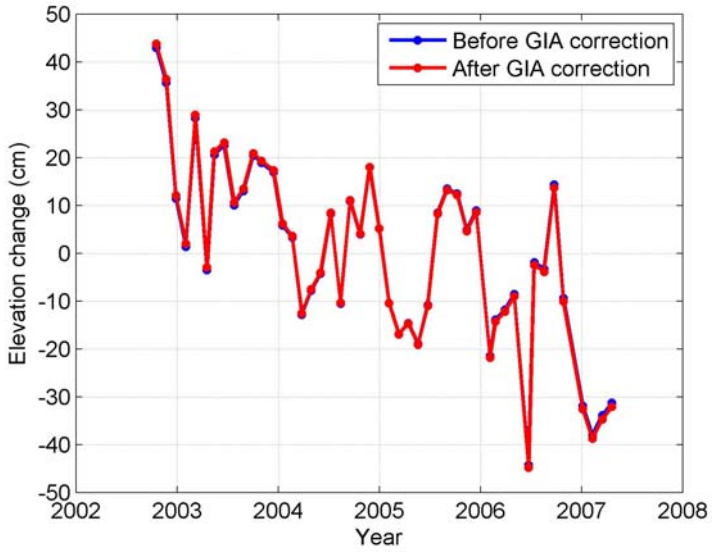

Figure 5.9: Basinwide time series over the Amundsen Sea sector from September 2002 to May 2007 (a) before and after adjustment for backscattered power, and (b) before and after correcting for crustal uplift predicted using IJ05 GIA model.

	Time Span	Observed Area (10^6 km^2)	dH / dt (cm/year)
Wingham et al. (1988)	1992-1996	0.43	-11.7 ± 1.0
Davis and Ferguson (2004)	1995-2000	0.40	-8.9 ± 1.3
Davis et al. (2005)	1992-2003	0.39	-10.0 ± 0.4
Wingham et al. (2006a)	1992-2003	0.40	-6.8 ± 0.3
This study	2002-2007	0.40	-10.5 ± 1.5* -9.3 ± 1.2** -9.7 ± 1.2***

*: Before adjustment for backscattered power
**: After adjustment for backscattered power
***: After correcting for isostatic uplift using IJ05 GIA model

Table 5.1: Comparison of dH / dt from this study with previous studies. The observed area in this study is computed by $(R\Delta\theta)(R\Delta\lambda\cos\theta_i)$ for each $1^\circ \times 1^\circ$ region identified to be the Amundsen Sea sector using the mask from Vaughan et al. (1999). $R = 6371$ km, $\Delta\theta = \Delta\lambda = 1^\circ$ are used.

Finally, the basinwide time series from Davis et al. (2005) over the Amundsen Sea sector (or basin G-H) is combined with the time series from this study as shown in Figure 5.10. There is an overlap between September 2002 and May 2003. The seasonality and the amplitude of the overlapping part of two time series show an excellent agreement.

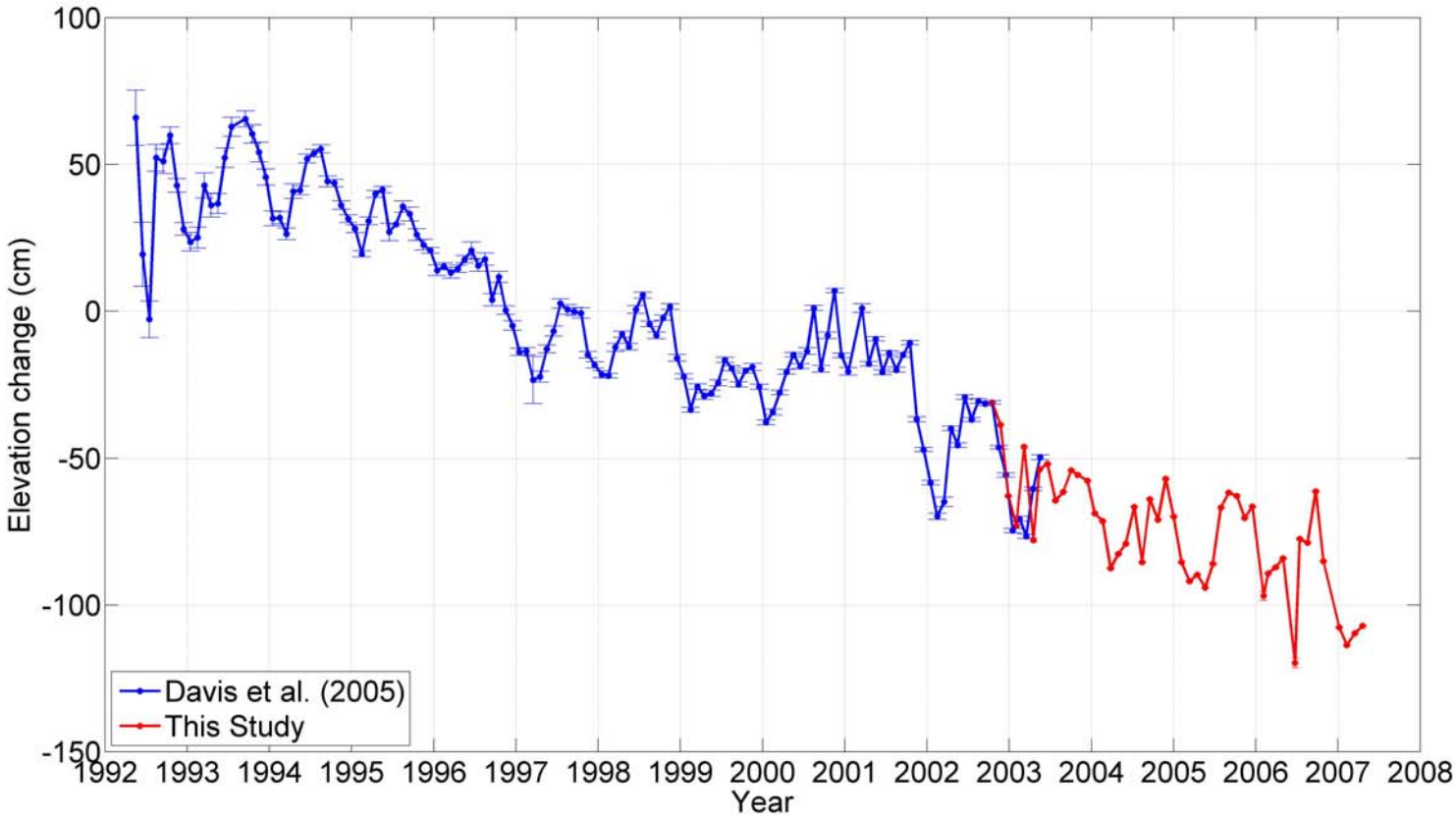

Figure 5.10: Basinwide time series over the Amundsen Sea sector from Davis et al. (2005) and this study.

5.3 Ice Mass Loss from GRACE

GRACE has been providing monthly measures of Earth gravity changes and used successfully in polar ice sheet mass balance studies (Velicogna and Wahr, 2006a, 2006b; Chen et al., 2006, 2008). However, GIA remains one of the strongest signals in GRACE, and it is difficult to separate GIA and ice mass balance (Wahr et al., 2000). Figure 2 shows the predicted mass change in terms of equivalent water thickness using IJ05, ICE-5G (VM4), and RF3S20 (β =0.4). It is apparent to see the substantial differences between the GIA models and this significant degree of uncertainty in the GIA models highlights the difficulties involved in the current approach adopted to remove the GIA effect using a forward model to estimate the Antarctica ice mass balance (Shum et al., 2008).

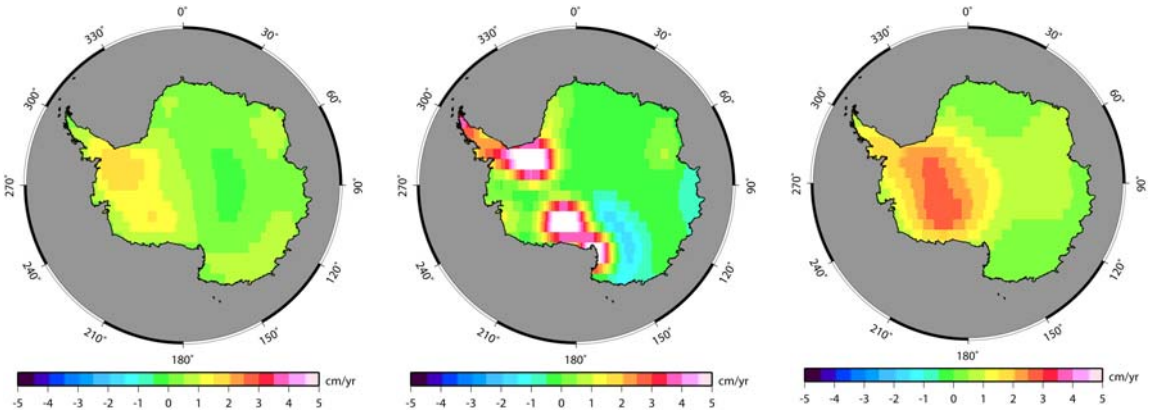

Figure 5.11: GIA models (left) IJ05, (middle) ICE-5G (VM4), (right) RF3S20 ($\beta = 0.4$) expressed in equivalent water thickness change after applying 300 km Gaussian filtering.

Another error source is the secular trend of the so-called geocenter correction, which is not included in the GRACE temporal gravity field solutions because GRACE is a twin-satellite system and the differential measurement (satellite-to-satellite tracking) diminishes GRACE's sensitivity to the geocenter motion which represent the longest wavelength component of the Earth's geopotential (Shum et al., 2008). This could affect the estimate of the ice sheet mass balance (Chambers et al., 2007). In this study, the geocenter correction determined using SLR (J. Ries, personal communication, 2008) is applied. Furthermore, as in Velicogna and Wahr (2006a), hydrologic contamination by signals outside Antarctica is removed using monthly global water storage fields from the Global Land Data Assimilation System (GLDAS) (Rodell et al., 2004; data courtesy, W. van der Wal). This study uses recent Release 4 (RL04) Jet Propulsion Laboratory (JPL) GRACE data product from April 2002 – December 2007 (65 months), which is longer than that used in recent study by Chen et al. (2008). After correcting for geocenter and hydrology contamination, the equivalent water thickness, Δh, can be computed as in

Wahr et al. (1988):

$$\Delta h(\theta,\lambda) = \frac{a\sigma_E}{3\sigma_w}\sum_{n=0}^{\infty}\sum_{m=0}^{n}\overline{P}_{nm}(\cos\theta)\frac{(2n+1)}{(k_n+1)}\times(\Delta\overline{C}_{nm}\cos(m\lambda)+\Delta\overline{S}_{nm}\sin(m\lambda)) \qquad (5.1)$$

with:

$\Delta\overline{C}_{nm},\Delta\overline{S}_{nm}$: geopotential spherical harmonic change

a : radius of Earth

n,m : degree and order

Continued

Equation (5.1) continued

k_n : load Love number of degree n that describes the Earth's elastic deformation

$\overline{P}_{nm}$: fully normalized associated Legendre function

σ_w : density of water (1000 kg/m^3)

σ_E : average density of the Earth (5517 kg/m^3)

After applying 300 km Gaussian filtering (Jekeli, 1981; Wahr et al., 1998), the equivalent water thickness is estimated at 1˚ × 1˚ grids over Antarctica from each of the 56 monthly gravity fields. Antarctic ice sheet balance is estimated from the equivalent water thickness time series by fitting a linear trend and annual and semiannual sinusoids. Figure 5.12 illustrates the spatial map of the rate of the estimated equivalent water thickness change over Antarctica showing the effect of geocenter, hydrology contamination and GIA corrections. It is apparent that the mismodeling of GIA could significantly influence the GRACE-derived ice mass balance estimates. Figure 5.13 shows the time series over entire grounded Antarctic ice sheet and the Amundsen Sea sector using the same mask as in Chapter 5.2 (Vaughan et al., 1999; data courtesy, A. Monaghan). The estimated mass balance varies with the choice of the GIA model: -0.62 ± 0.12 cm/year (IJ05), -0.44 ± 0.12 cm/year (ICE-5G (VM4)), and -1.21 ± 0.12 cm/year (RF3S20 β=0.4). It can be seen that the mass balance estimates can differ by almost a factor of 2. Thus, the incomplete GIA signal dominates the present-day mass balance signal from GRACE. As proposed by Wahr et al. (2000), a combination of satellite altimetry data and GRACE could potentially be used to separate the GIA and ice mass balance signals.

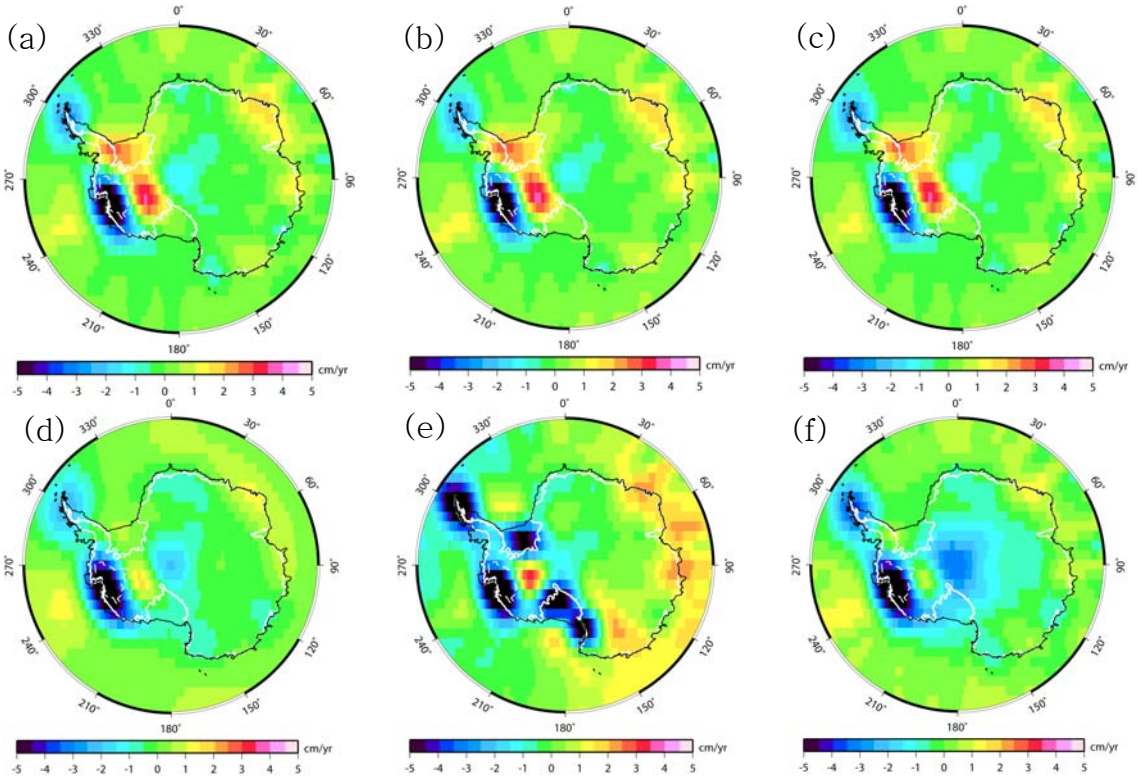

Figure 5.12: Spatial maps of mass rates (in terms of equivalent water thickness changes per year) estimated from 56 GRACE RL04 monthly gravity solutions with 300 km Gaussian filtering. (a) no correction (b) after geocenter correction (c) after correcting for geocenter and hydrology contamination (d) after correcting for geocenter, hydrology contamination and GIA using IJ05 (e) after correcting for geocenter, hydrology contamination and GIA using ICE-5G (VM4) (f) after correcting for geocenter, hydrology contamination and GIA using RF3S20 ($\beta = 0.4$). The white solid line indicates the grounding line and the white dashed line indicates the boundary of the Amundsen Sea sector.

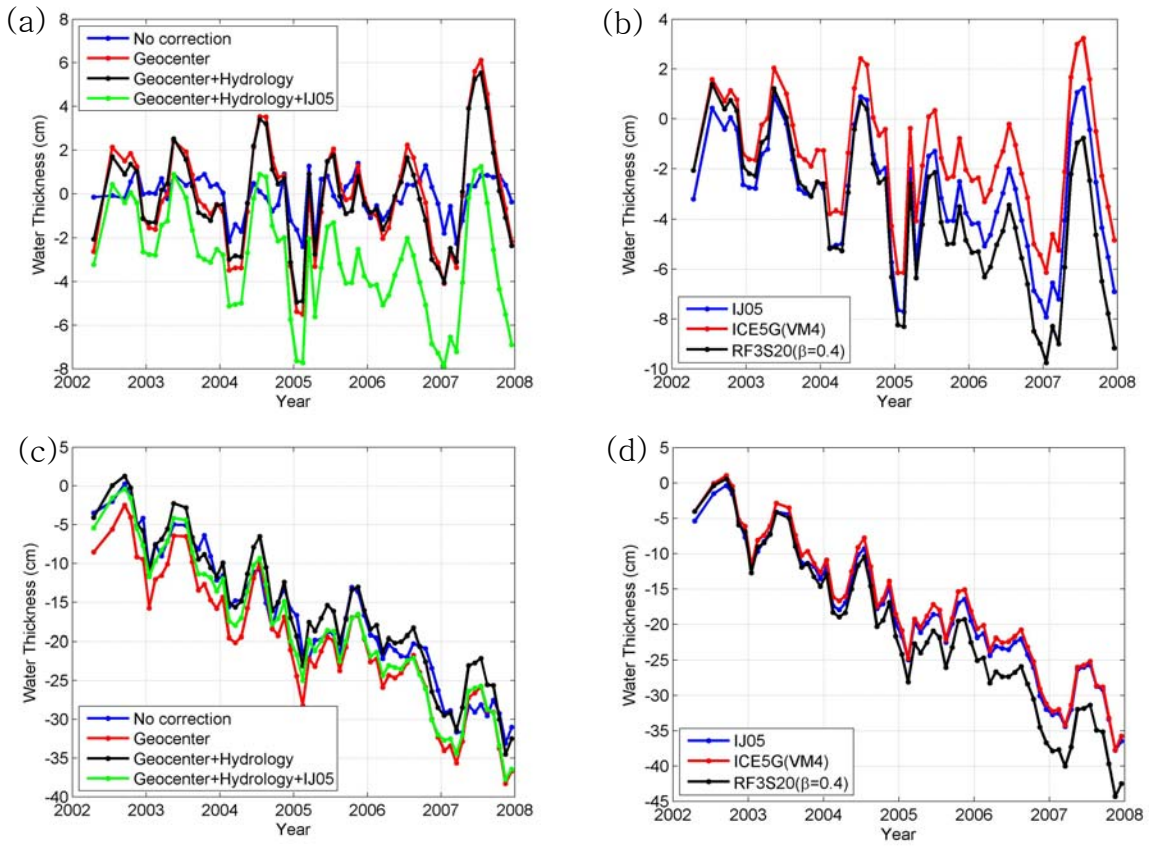

Figure 5.13: Time series of equivalent water thickness changes from April 2002 – December 2007 over entire grounded Antarctic ice sheet ((a) and (b)), the Amundsen Sea sector ((c) and (d)). (b) and (d) show the effect of GIA corrections using different GIA models (after correcting for geocenter and hydrology contamination).

	Antarctic grounded ice sheet (cm/year)	Basin G-H (cm/year)
No correction	-0.057 ± 0.059	-5.164 ± 0.179
With geocenter correction	0.047 ± 0.125	-4.963 ± 0.210
With geocenter + hydrology contamination correction	-0.004 ± 0.123	-5.032 ± 0.205
With geocenter + hydrology contamination correction + IJ05	-0.620 ± 0.122	-5.488 ± 0.190
With geocenter + hydrology contamination correction + ICE-5G (VM4)	-0.443 ± 0.123	-5.611 ± 0.205
With geocenter + hydrology contamination correction + RF3S20 ($\beta = 0.4$)	-1.207 ± 0.123	-6.791 ± 0.205

Table 5.2: Estimated mass rates in terms of equivalent water thickness changes over entire grounded Antarctic ice sheet and the basin G-H. It is noted that RF3S20 ($\beta = 0.4$) provides the largest Antarctic mass imbalance estimates.

5.4 Ice Mass Loss over the Amundsen Sea Sector

To estimate ice sheet mass balance through the elevation changes (dH/dt), "constant" ice sheet density has been used to determine volume change (Davis et al., 2005; Wingham et al., 2006a). However, the unknown depth and density of firn, a layer of old snow which is tens of meters thick (Paterson, 1994), complicates the conversion from dH/dt to mass change (Helsen et al., 2008). The firn layer densifies over time at a rate which depends on both accumulation rate and temperature, and the firn depth changes may have a large influence on altimetry-observed dH/dt which spans only about 15 years (van den Broeke et al., 2006). Helsen et al. (2008) derived a "corrected" dH/dt signal which is free of interannual fluctuations in firn depth. They combine a firn densification model (Zwally and Li, 2002) and time series of accumulation and temperature from a regional climate model (1980-2004), and simulated interannual firn depth variability over the entire continent. By subtracting simulated firn depth changes from altimetry-derived dH/dt, the corrected dH/dt is obtained. According to Helsen et al. (2008), the amount of ice mass loss is increased by correcting for firn depth fluctuations over the Amundsen Sea Embayment (basin G-H, G-F', H-H'). The uncorrected ERS-2 (1995-2003) dH/dt is -9.2 ± 0.7 cm/year, and subtracting the interannual firn depth variability (1980-2004) of 3.5 ± 0.5 cm/year results in the corrected ERS-2 dH/dt of -12.7 ± 0.9 cm/year. If the same firn depth variability is used, the "corrected" Envisat dH/dt (2002-2007) of basin G-H becomes -13.2 ± 1.3 cm/year.

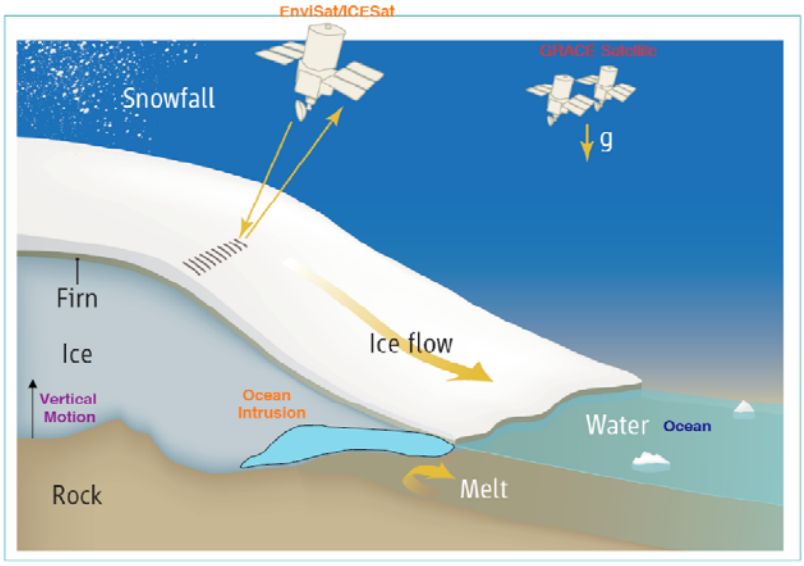

Figure 5.14: Schematics of ice mass balance measurements (altimetry and GRACE) [Modified from Fig.1 in Cuffey (2008)].

Mass changes (dM/dt) can be calculated from the elevation changes (dH/dt) such as (Helsen et al., 2008):

$$\frac{dM}{dt} = \frac{dH}{dt} \cdot Area_{ice} \cdot \rho_* \tag{5.2}$$

with:

$Area_{ice}$: area of the grounded ice

ρ_* : density of firn/ice

Helsen et al. (2008) used density of ice (ρ_i=917 kg m^{-3}) for the Amundsen Sea sector to calculate the mass change because changing ice dynamics is believed to be responsible for the elevation changes in that drainage basin. This is in agreement with Wingham et al. (2006a) who attributed the fluctuation to changes in ice for basin G-H based on glaciological or meteorological observations. Hence, the ice density is used to convert the uncorrected/corrected dH/dt to dM/dt in Table 5.3 which summarizes the ice mass loss in the Amundsen Sea sector calculated from previous studies and this study.

	Observation / GIA model used	dM / dt (Gt/year)	Equivalent sea level change (mm/year)
Davis et al. (2005)	Uncorrected ERS-1/2 (1992-2003) / Ivins et al. (2001)	-38 ± 2	0.11 ± 0.002
Wingham et al. (2006a)	Uncorrected ERS-1/2 (1992-2003) / Nakada et al. (2000)	-26 ± 1	0.07 ± 0.002
Helsen et al. (2008)	Corrected ERS-2 (1995-2003) / Ivins et al. (2001)	-55 ± 9	0.13 ± 0.010
This study	Uncorrected Envisat Corrected Envisat (2002-2007) / IJ05	-38 ± 5 -49 ± 5	0.10 ± 0.013 0.14 ± 0.014
This study	GRACE (2002-2007) / IJ05	-22 ± 1	0.06 ± 0.002

Table 5.3: Comparison of the estimated ice mass losses in gigaton (10^6 kg) per year over the Amundsen Sea sector (or basin G-H) and their contribution to the sea level change. The equivalent sea level change is computed by assuming the global ocean area to be 361 $\times$ 10^6 km^2 and density of sea water to be 1027 kg m^{-3}.

It can be seen that the "uncorrected" Envisat mass change estimates agree well with Davis et al. (2005) and the "corrected" Envisat mass change estimates agree well with "corrected" ERS-2 from Helsen et al. (2008). The GRACE mass change estimate shows discrepancy with altimetry-derived mass change estimates, and one possible cause can be "leakage" problem which is due to the restricted spectral resolution of the gravitational field estimates and the applied spatial smoothing (Wahr et al., 1998; Guo et al., 2008; Baur et al., 2008). Due to the fact that the smoothed value of mass change at a point is a weighted average of the unsmoothed values around that point, the signal at the land side is "leaked" into the ocean side and a part of the signal at the land side, which is added to the smoothed value at the ocean side, is lost (Guo et al., 2008). Therefore, correcting for this leakage could enhance the signal at the coastal land side, resulting in stronger negative ice mass trends in this case. Finally, as indicated before and also by Shum et al. (2008), the uncertainty in GIA models, which significantly influences GRACE observations, could be a primary reason of the discrepancy between GRACE and Envisat estimated ice mass balance over the Amundsen Sea sector.

CHAPTER 6

CONCLUSIONS AND FUTURE STUDIES

Satellite radar altimetry, which was initially designed for accurate measurements of sea surface height and shape globally, has been demonstrated to be applicable to non-ocean surfaces as well. In this study, three different applications have been examined: solid Earth crustal deformation due to GIA (Chapter 3), water level fluctuation over vegetated wetlands (Chapter 4), and ice sheet elevation changes over Antarctica (Chapter 5). The high-rate (10-Hz for TOPEX, 18-Hz for Envisat) regional stackfiles over the study regions have been developed based on the original 1-Hz global ocean stackfile for the collinear analysis.

In Chapter 3, an alternative modified threshold retracker for land waveforms was developed and 90-m resolution C-band SRTM DEM played an important role as a reference for selecting an optimal retracker and to provide surface gradient corrections for the computation of land surface anomalies. As a result, decadal vertical motion time series over a 1500 km by 1000 km region covering northern Ontario and northeastern Manitoba, and over the Great Lakes have been generated using TOPEX data. The vertical motion estimates qualitatively agreed well with other geodetic measurements from GPS and tide gauge/altimetry combination. Land altimetry solutions were further compared with GRACE-derived vertical motion and various GIA models and agreed well with the GIA model RF3S20 (β=0.4), and it can be concluded that the land altimetry solutions can be incorporated with other geodetic measurements to be used as additional constraints for GIA model improvements in the future (Wang et al., 2008). The extension of the study region to Fennoscandia, where large GIA amplitudes up to ~10 mm/year are observed (Milne et al., 2001), can be a future study. Other possible future studies include the use of other satellite radar altimeters, for example Envisat, by building 18-Hz stackfiles to increase the spatial coverage and data time span. However, it is anticipated that the vertical motion from ENVISAT would be less accurate due to the shorter time span and longer repeat period (35 days) than those of TOPEX.

The results presented in Chapter 4 are to show, for the first time, the water level variation in Louisiana's vegetated wetland over each 10-Hz stackfile bin with the highest along-track spatial resolution (~660 m) achievable from TOPEX. This is different from the previous studies (Birkett, 1998; Birkett et al., 2002; Maheu et al., 2003) which spatially averaged the 10-Hz measurements along the satellite track and river/wetland

intersections, allowing only one time series per intersection. Furthermore, the need for retracking over vegetated wetlands is examined by computing the retracked gates and comparing the water level time series from TOPEX and river gauge before and after applying retracking. The wetland water fluctuation in terms of amplitude of the TOPEX time series over each 10-Hz stackfile bin has been examined using the C-band SRTM DEM elevation and L-band ALOS SAR imagery. These observations could help quantify the depletion or rise of water level in wetlands and the precise estimate of water storage over wetlands. These observations can also be used to improve the hydrological modeling by providing large-scale calibration data sets to precisely estimate hydrological parameters for numerical modeling. Improving hydrological modeling is a critical step to enhance prediction and assessment capabilities for future flood events over wetlands. For a possible future study, other satellite radar altimeters could be used to enhance the spatial coverage and data time span, for example, by constructing 18-Hz stackfile using Envisat GDRs. Another possible study is to estimate the vertical crustal motions, the subsidence in Louisiana wetlands, at river gauge stations by combining the TOPEX-driven geocentric water level measurements and the long-term relative water level records from river gauges using a stochastic adjustment model (Kuo et al., 2004; 2008).

In Chapter 5, 18-Hz regional stackfile over the Amundsen Sea sector, West Antarctica is developed using Envisat GDR measurements. With 1-km resolution Antarctic DEM (data courtesy, J. Bamber), the ice sheet elevation changes over $1^\circ \times 1^\circ$ grids are estimated from September 2002 – May 2007 using collinear analysis which is free of the surface anisotropy which causes a systematic height difference as large as a few meters at the crossover points (Remy et al., 2006). The estimates of ice mass loss is estimated considering the interannual firn depth variation and compared with previous studies. The ice mass loss from GRACE JPL RL04 data from April 2002 – December 2007 is also estimated and it has been shown that GIA signal significantly affects GRACE-derived entire Antarctic mass loss by a factor of 2. The methodology can also be applied to other regions in Antarctica, for example, interior of East Antarctic ice sheet which increased in overall thickness as the overall contribution of the Antarctic ice sheet to the global sea level change will depend on the mass balance between the West and East Antarctica (Davis et al., 2005).

BIBLIOGRAPHY

Algiers. J., et al., TOPEX Ground System Software Interface Specification, Volume 2: Design (SIS-2), Altimeter Sensor Data Record (SDR) – Alt SDR Data, March 1993, JPL D-8591, Rev. C, 1993.

Alley, R., P. Clark, P. Huybrechts, and I. Joughin, Ice-sheet and sea-level changes, *Science*, 310, 456–460, 2005.

Alley, R., S. Anandakrishnan, T. Dupont, B. Parizek, and D. Pollard, D., Effect of sedimentation on ice-sheet grounding-line stability, *Science*, 1–5, 10.1126/science.1138396, 2007.

Alsdorf, D.E., J.M., Melack, T. Dunne, L.A.K. Mertes, L.L. Hess, and L.C. Smith, Interferometric radar measurements of water level changes on the Amazon floodplain, *Nature*, 404, 174-177, 2000.

Alsdorf, D., C. Birkett, T. Dunne, J. Melack, and L. Hess, Water level changes in a large Amazon lake measured with spaceborne radar interferometry and altimetry, *Geophy. Res. Lett.*, 28, 2671-2674, 2001.

Anandarkrishnan, S., G. Catania, R. Alley, and H. Horgan, Discovery of till deposition at the grounding line of Whillans Ice Stream, *Science*, 1–5, 10.1126/science.1138393, 2007.

Anzenhofer, M., C. Shum, and M. Rentsch, Coastal altimetry and applications, *Rep. 464*, Dept. of Geod. Sci. and Surv., Ohio State Univ., USA, 1999.

Bamber, J.L., Ice sheet altimeter processing scheme, *Int. J. Remote Sens.*, 15, 925-938, 1994.

Bamber, J. and J.L. Gomez-Dans, The accuracy of digital elevation models of the Antarctic continent, *Earth Planet. Sc. Lett.*, 237, 516-523, 2005.

Bell, R., M. Studinger, C. Shuman, M. Fahnestock, and I. Joughin, Large subglacial lakes in East Antarctica at the onset of fast-flowing ice streams, *Nature*, 445, 904–907, 2007.

Bhang, K.J., F.W. Schwartz, and A. Braun, Verification of the Vertical Error in C-Band SRTM DEM Using ICESat and Landsat-7, Otter Tail County, MN, *IEEE Trans. Geosci. Remote Sens.*, 45, 36-44, 2007.

Baur, O., M. Kuhn, and W.E. Featherstone, Investigations on reliable secular ice-mass and sea-level changes from GRACE, *IAG International Symposium on Gravity, Geoid & Earth Observation*, Chania, Greece, 23-27 June, 2008.

Bentley, C., Mass balance of the Antarctic ice sheet: Observational aspects, in: Bamber, J., Payne, A. (Eds.), Mass Balance of the Cryosphere: Observations and Modeling of Contemporary and Future Changes. Cambridge University Press, Cambridge, pp. 459–489, 2004.

Benveniste, J., ENVISAT RA-2/MWR product handbook, Issue 1.2, PO-TN-ESR-RA-0050, Frascati, Italy: European Space Agency, 2002.

Berrick, D.E. and B.J. Lipa, Analysis and interpretation of altimeter sea echo, *Adv. Geophys.*, 27, 61-100, 1985.

Berry, P.A.M., R.A. Pinnock, R.D. Hilton, and C.P.D. Johnson, ACE: a new global digital elevation model incorporating satellite altimeter derived heights, *Proc. ERS-Envisat Symposium*, SP-461, Gothenburg, Sweden, 2000.

Berry, P.A.M., Topography from land radar altimeter data: possibilities and restrictions, *Phys. Chem. Earth (A)*, 25, 81-88, 2000.

Berry, P.A.M., J.D. Garlick, J.A. Freeman, and E.L. Mathers, Global inland water monitoring from multi-mission altimetry, *Geophys. Res. Lett.*, 32, L16401, doi:10.1029/2005GL022814, 2005.

Berry, P.A.M., J.D. Garlick, and R.G. Smith, Near-global validation of the SRTM DEM using satellite radar altimetry, *Remote Sens. Environ.*, 106, 17-27, 2007.

Birkett, C.M., The contribution of TOPEX/POSEIDON to the global monitoring of climatically sensitive lakes, *J. Geophys. Res.*, 100, 25179-25204, 1995.

Birkett, C.M., Contribution of the TOPEX NASA radar altimeter to the global monitoring of large rivers and wetlands, *Water Resour. Res.*, 34, 1223-1239, 1998.

Birkett, C.M., L.A.K. Mertes, T. Dunne, M.H. Costa, and M.J. Jasinski, Surface water dynamics in the Amazon Basin: Application of satellite radar altimetry, *J. Geophys. Res.*, 107, doi:10.1029/2001JD000609, 2002.

Braun, A. and G. Fotopoulos, Assessment of SRTM, ICESat, and Survey Control Monument Elevations in Canada, *Photogramm. Eng. Rem. S.*, 73, 1333-1342, 2007.

Braun, A., C.-Y. Kuo, C.K. Shum, P. Wu, W. van der Wal, and G. Fotopoulos, Glacial Isostatic Adjustment at the Laurentide ice sheet margin: models and observations in the Great Lakes region, *J. Geodyn*., 10.1016/j.jog.2008.03.005, 2008.

Brooks, R.L., D.W. Lockwood, and J.E. Lee, Land effects on TOPEX radar altimeter measurements in Pacific Rim coastal zones, *NASA WFF Publ.*, 1997. (Available at http://topex.wff.nasa.gov)

Brown, G.S., The average impulse response of a rough surface and its applications, *IEEE Trans. Antennas Propag.*, 25, 67-74, 1977.

Calais E., J.Y. Han, C. DeMets, and J.M. Nocquet, Deformation of the North American plate interior from a decade of continuous GPS measurements, *J. Geophys. Res.*, 111, B06402, doi:10.1029/2005JB004253, 2006.

Callahan, P.S., TOPEX/POSEIDON Project, GDR User's Handbook, JPL D-8944, 1992.

Cazenave, A., P. Bonnefond, K. Dominh, and P. Schaeffer, Caspian sea level from Topex-Poseidon altimetry: level now falling, *Geophys. Res. Lett.*, 24, 881-884, 1997.

Cazenave, A., How fast are the ice sheets melting? *Science*, 314, 1250–1252, 2006.

Chambers, D.P., M.E. Tamisiea, R.S. Nerem, and J.C. Ries, Effects of ice melting on GRACE observations of ocean mass trends, *Geophys. Res. Lett.*, 34, L05610, doi:10.1029/2006GL029171, 2007.

Chelton, D.B., E.J. Walsh, and J.L. MacArthur, Pulse compression and sea level tracking in satellite altimetry, *J. Atmos. Ocean. Tech.*, 6, 407-438, 1989.

Chelton, D.B., J.C. Ries, B.J. Haines, L.-L. Fu, and P.S. Callahan, Satellite altimetry. In: L.-L. Fu and A. Cazenave (editors), Satellite Altimetry and Earth Sciences: A Handbook of Techniques and Applications, Elsevier, New York, 1-132, 2001.

Chen, J., C. Wilson, D. Blankenship, and B. Tapley, Antarctic mass rates form GRACE, *Geophys. Res. Lett.*, 33, L11502, doi:10.1029/2006GL026369, 2006.

Chen, J., C. Wilson, B. Tapley, D. Blankenship, and D. Young, Antarctic regional ice loss rates from GRACE, *Earth Planet. Sci. Lett.*, 266, 140-148, 2008.

Cuffey, K.M., A matter of firn, *Science*, 320, 10.1126/science.1158683, 2008.

Davis, C.H., Satellite radar altimetry over the continental ice sheets, Ph.D. dissertation, Univ. of Kansas, USA, 1992.

Davis, C.H. and H.J. Zwally, Geographic and seasonal variations in the surface properties of the ice sheets by satellite-radar altimetry, *J. Glaciol.*, 39, 687-697, 1993.

Davis, C.H., A robust threshold retracking algorithm for measuring ice-sheet surface elevation change from satellite radar altimeter, *IEEE Trans. Geosci. Remote Sens.*, 35, 974-979, 1997.

Davis, C.H. and A.C. Ferguson, Elevation change of the Antarctic Ice Sheet, 1995-2000, from ERS-2 satellite radar altimetry, *IEEE Trans. Geosci. Remote Sens.*, 42, 2437-2445, 2004.

Davis, C.H., Y. Li, J.R. McConnell, M.M. Frey, and E. Hanna, Snowfall-driven growth in East Antarctic ice sheet mitigates recent sea-level rise, *Science*, 308, 1898-1901, 2005.

Deng, X.L., W.E. Featherstone, C. Hwang and C.K. Shum, Improved coastal marine gravity anomalies in the Taiwan Strait from altimeter waveform re-tracking, *Proc. International Workshop on Satellite Altimetry for Geodesy, Geophysics and Oceanography*, Wuhan, China, September, 2001.

Deng, X., W.E. Featherstone, C. Hwang and P.A.M. Berry, Estimation of contamination of ERS-2 and POSEIDON satellite radar altimetry close to the coasts of Australia, *Marin Geodesy*, 25, 249-271, 2002.

Deng, X.L., Improvement of geodetic parameter estimation in coastal regions from satellite radar altimetry, Ph.D. dissertation, Curtin Univ. of Technology, Australia, 2003.

Deng, X., and W.E. Featherstone, A coastal retracking system for satellite radar altimeter waveforms: Application to ERS-2 around Australia, *J. Geophys. Res.*, 111, doi:10.1029/2005JC003039, 2006.

Douglas, B., Sea Level Rise: History and consequences, Chapter 3, Sea level change in the era of the recording tide gauge, 37–64, Academic Press, 2001.

Dupont, T. and R. Alley, Assessment of the importance of ice-shelf buttressing to ice-sheet flow, *Geophys. Res. Lett.*, 32, L04503, doi:10.1029/2004GL022024, 2005.

Dyke, A.S. and W.R. Peltier, Forms, Response times and variability of relative sea level curves in glaciated North America, *Geomorphology*, 32, 315-333, 2000.

Dyke, A.S., J.T. Andrews, P.U. Clark, J.H. England, G.H. Miller, J. Shaw, and J.J. Veilette, The Laurentide and Innuitian ice sheets during the Last Glacial Maximum, *Quartern. Sci. Rev.*, 21:9-31, 2002.

Farrell, W.E. and J.A. Clark, On postglacial sea level, *Geophys. J. Int.*, 46, 647-667, 1976.

Frappart, F., S. Calmant, M. Cauhopé, F. Seyler, and A. Cazenave, Preliminary results of ENVISAT RA-2-derived water levels validation over the Amazon basin, *Remote*

Sens. Environ., 100, 252-264, 2006.

Fricker, H., T. Scambos, R. Bindschadler, and L. Padman, An active subglacial water system in West Antarctic mapped from space, *Science*, 315, 1544–1548, 2007.

Gammill, S., et al., Hydrologic investigation of the Louisiana Chenier Plain, Louisiana Department of Natural Resources, 2002.

Guman, M.D., Determination of global mean sea level variations using multi-satellite altimetry, Ph.D. dissertation, Univ. of Texas at Austin, USA, 1997.

Gunter, B.C., R.E.M. Riva, T. Urban, B. Schutz, R. Harpold, M. Helson, and P. Nagel, *IAG International Symposium on Gravity, Geoid & Earth Observation*, Chania, Greece, 23-27 June, 2008.

Guo, J.Y., X.J. Duan, and C.K. Shum, Non-isotropic filtering and leakage reduction for determining mass changes over land and ocean using GRACE data, *Geophy. J. Int.*, submitted, 2008.

Hallikainen, M., F. Ulaby, and M. Abdelrazik, Dielectric properties of snow in the 3 to 37 GHz range, *IEEE Trans. Antennas Propag.*, 34, 1329-1340, 1986.

Han, S.-C., C. Jekeli, and C.K. Shum, Time-variable aliasing effects of ocean tides, atmosphere, and continental water mass on monthly mean GRACE gravity field, *J. Geophys. Res*., 109, B04403, doi:10.1029/2003JB002501, 2003.

Han, S.C., C.K. Shum, C. Jekeli, C.-Y. Kuo, C. Wilson, and K.W. Seo, Non-isotropic Filtering of GRACE Temporal Gravity for Geophysical Signal Enhancement, *Geophys. J. Int.*, 163, 18-25, 2005.

Hatton, R., R. DeLaune, and W. Patrick, Jr., Sedimentation, accretion, and subsidence in marshes of Barataria Basin, Louisiana, *Limnol. Oceanogr.*, 28, 494-502, 1983.

Hayne, G.S., Radar altimeter mean return waveform from near-normal-incidence ocean surface scattering, *IEEE Trans. Antennas Propag.*, AP-28, 687-692, 1980.

Hayne, G.S., D.W. Hancock III, and C.L. Purdy, The corrections for significant wave height and attitude effects in the TOPEX radar altimeter, *J. Geophys. Res.*, 99(C12), 24941-24955, 1994.

Hayne, G.S. and D.W. Hancock, Topex Side B sigma0 calibration table adjustment, NASA, Goddard Space Flight Center, Wallops Flight Facility, 2000.

Helsen, M.M., M.R. van den Broeke, R.S.W. van de Wal, W.J. van de Berg, E. van Meijgaard, C.H. Davis, Y. Li, and I. Goodwin, *Science*, 320, 1626-1629, 2008.

Hess, L.L., J.M. Melack, E.M.L.M Novo, C.C.F. Barbosa, and M. Gastil, Dual-season

mapping of wetland inundation and vegetation for the central Amazon basin, *Remote Sens. Environ*., 87, 404-428, 2003.

Hilton, R.D., W.E. Featherstone, P.A.M. Berry, C.P.D. Johnson, and J.F. Kirby, Comparison of digital elevation models over Australia and external validation using ERS-1 satellite radar altimetry, *Aust. J. Earth Sci.*, 50, 157-168, 2003.

Hwang, C., J. Guo, X. Deng, H.-Y. Hsu, and Y. Liu, Coastal gravity anomalies from retracked Geosat/GM altimetry: improvement, limitation and the role of airborne gravity data, *J. Geod.*, 80, 204-216, 2006.

Invins, E.R., X. Wu, C.A. Raymond, C.F. Yoder, and T.S. James, Temporal geoid of a rebounding Antarctica and potential measurement by the GRACE and GOCE satellites, *Int. Assoc. Geodesy Symp*., 123, 361, 2001.

Ivins, E., C. Raymond and T. James, Late-Pleistocene, Holocene and present-day ice load evolution in the Antarctic Peninsula: Models and predicted vertical crustal motion, in *Ice Sheets, Sea Level and the Dynamic Earth*, (ed. J.X. Mitrovica and B. Vermeersen), *Geodynamics Ser*. 29, 133-155, A.G.U., Washington, DC, 2002.

Ivins, E.R. and T.S. James, Antarctic glacial isostatic adjustment: a new assessment, *Antarct. Sci.*, 17, 541–553, 2005.

Ivins, E. R. Dokka, and R. Blom, Post-glacial sediment load and subsidence in coastal Louisiana, *Geophys. Res. Lett.*, 34, L16303, doi:10.1029/2007GL030003, 2007.

Jacobs, S., H. Helmer, C. Doake, A. Jenkins, and R. Frolich, Melting of the ice shelves and the mass balance of Antarctica, *J. Glaciol.*, 38, 130, 375–387, 1992.

Jekeli, C., Alternative methods to smooth the Earth's gravity field, *Rep. 327*, Dept. of Geod. Sci. and Surv., Ohio State Univ., USA, 1981.

Johansson, J., J.L. Davis, H.-G. Scherneck, G.A. Milne, M. Vermeer, J.X. Mitrovica, R.A. Bennett, B. Jonsson B., G. Elgered, P. Elósegui, H. Koivula, M. Poutanen, B.O. Rönnäng, and I.I. Shaprio, Continuous GPS measurements of postglacial adjustment in Fennoscandia 1. Geodetic Results, *J. Geophys. Res.*, 107 (B8), 2157, doi:10.1029/2001JB001685, 2002.

Johnston, P., The effect of spatially non-uniform water loads on the prediction of sea-level change, *Geophys. J. Int*., 114, 615-634, 1993.

Kaufmann, G., P. Wu, and D. Wolf, Some effects of lateral heterogeneities in the upper mantle on postglacial land uplift close to continental margins, *Geophys. J. Int.*, 128, 175-187, 1997.

Kouraev, A.V., E.A. Zakharova, O. Samain, N.M. Mognard, and A. Cazenave, Ob' river

dischange from TOPEX/Poseidon satellite altimetry (1992-2002), *Remote Sens. Environ.*, 93, 238-245, 2004.

Kruizinga, G.J., Dual-satellite altimeter crossover measurements for precise orbit determination, Ph.D. dissertation, CSR-95-4, Univ. of Texas, USA, 1997.

Kuo, C.Y., C.K. Shum, A. Braun, and J.X. Mitrovica, Vertical crustal motion determined by satellite altimetry and tide gauge data in Fennoscandia, *Geophy. Res. Lett.*, 31, L01608, doi:10.1029/2003GL019106, 2004.

Kuo, C.Y., C.K. Shum, A. Braun, K. Cheng, and Y. Yi, Vertical motion determined using satellite altimetry and tide gauges, *Terr. Atmos. Ocean. Sci.*, 19, 21-25, doi:10.3319/TAO.2008.19.1-2.21(SA), 2008.

Lambeck, K., T. Esat, and E. Potter, Links between climate and sea levels for the past three million years. *Nature*, 419, 199–206, 2002.

Lambert, A.N., N. Courtier, G.S. Sasagawa, F. Klopping, D. Winester, T.S. James, and J.O. Liard, New constraints on Laurentide postglacial rebound from absolute gravity measurements, *Geophys. Res. Lett.*, 28, 109-112, 2001.

Larsen, C., K. Echelmeyer, J. Freymueller, and R. Motyka, Tide gauge records of uplift along the northern Pacific-North America plate boundary, 1937 to 2001, *J. Geophys. Res.*, 108 (B4), 2216, doi:10.1029/2001JB001685, 2003.

Latychev, L., J. Mitrovica, M. Tamisiea, J. Tromp, and R. Moucha, Influence of lithospheric thickness variations on 3-D crustal velocities due to glacial isostatic adjustment, *Geophys. Res. Lett.*, 32, L01304, doi:10.1029/2004GL021454, 2005a.

Latychev, L., J. Mitrovica, J. Tromp, M. Tamisiea, D. Komatitsch, and C. Christara, Glacial isostatic adjustment on 3-D Earth models: a finite volume formulation. *Geophys. J. Int.* 161, 421–444, doi: 10.1111/j.1365-246X.2005.02536.x, 2005b.

Laxon, S., Sea ice altimeter processing scheme at the EODC, *Int. J. Remote Sens.*, 15, 915-924, 1994.

Legresy, B., F. Papa, F. Remy, G. Vinay, M. van den Bosch, and O.-Z. Zanife, ENVISAT radar altimeter measurements over continental surfaces and ice caps using the ICE-2 retracking algorithm, *Remote Sens. Environ.*, 95, 150-163, 2005.

Legresy, B., F. Remy, and F. Blarel, Along track repeat altimetry for ice sheets and continental surface studies, *Proc. 15 Years of progress in Radar Altimetry Symposium*, Venice, Italy, 2006.

Lemke, P., J. Ren, R. Alley, I. Allison, J. Carrasco, G. Flato, Y. Fujii, G. Kaser, P. Mote, R. Thomas, T.J. Zhang, and 44 contributing authors, Chapter 4, Observations: Changes

in Snow, Ice and Frozen Ground, IPCC WG1 Fourth Assessment Report 337–383. Cambridge University Press, Cambridge., 2007.

Lee, H., C.K. Shum, C.Y. Kuo, Y. Yi, and A. Braun, Application of TOPEX altimetry for solid earth deformation studies, *Terr. Atmos. Ocean. Sci.*, 19, 38-46, doi:10.3319/TAO.2008.19.1-2.37(SA), 2008a.

Lee, H., C.K. Shum, Y. Yi, A. Braun, and C.Y. Kuo, Laurentia crustal uplift observed using satellite radar altimetry, *J. Geodyn.*, doi:10.1016/j.jog.2008.05.001, 2008b.

Licciardi, J.M., P.U. Clark, J.W. Jenson, and D.R. MacAyeal, Deglaciation of a soft-bed Laurentide ice sheet, *Quatern. Sci. Rev.*, 17, 427-448, 1998.

Lidberg, M., J.M. Johansson, H.-G. Scherneck, and J.L. Davis, An improved and extended GPS-derived 3D velocity field of the glacial isostatic adjustment (GIA) in Fennoscandia, *J. Geod.*, 81, 213-230, 2007.

Lu, Z., M. Crane, O. Kwoun, C. Wells, C. Swarzenski, and R. Rykhus, C-band radar observes water level changes in swamp forests, *EOS*, 86, 14, 141-144, 2005.

Lythe, M., D. Vaughan, and the BEDMAP Group, BEDMAP: A new ice thickness and subglacial topographic model of Antarctica, *J. Geophys. Res.*, 106(B6), 11335–11351, 2001.

Maheu, C., A. Cazenave, and C.R. Mechoso, Water level fluctuations in the Plata Basin (South America) from Topex/Poseidon Satellite Altimetry, *Geophy. Res. Lett.*, 30(3), 1143, doi:10.1029/2002GL016033, 2003.

Mäkinen, J., and V. Saaranen, Determination of post-glacial land uplift from the three precise levellings in Finland, *J. Geod.*, 72, 516-529, 1998.

Martin, T.V., H.J. Zwally, A.C. Brenner, and R.A. Bindschadler, Analysis and Retracking of Continental Ice Sheet Radar Altimeter Waveforms, *J. Geophys. Res.*, 88, 1608-1616, 1983.

Milne, G., J. Mitrovica, and J. Davis, Near-field hydro-isostasy: the implementation of a revised sea-level equation, *Geophys. J. Int.*, 129, 464–482, 1999.

Milne, G.A., J.L. Davis, J.X. Mitrovica, H.-G. Scherneck, J.M. Johansson, M. Vermeer, and H. Koivula, Space-geodetic constraints on glacial isostatic adjustment in Fennoscandia, *Science*, 29, 2381-2385, 2001.

Mitrovica, J. X., J. Davis, and I. Shapiro, I. I., A spectral formalism for computing 3-dimensional deformation due to surface loads, 1. Theory, *J. Geophys. Res.*, 99(B4), 7057–7073, 1994a.

Mitrovica, J. X., J. Davis, and I. Shapiro, A spectral formalism for computing 3-

dimensional deformation due to surface loads, 2. Present-day Glacial Isostatic Adjustment, *J. Geophys. Res*., 99(B4), 7075-7101, 1994b.

Mitrovica, J.X., A.M. Forte, and M. Simons, A reappraisal of postglacial decay times from Richmond Gulf and James Bay, Canada, *Geophys. J. Int.*, 142:783-800, 2000.

Mitrovica, J., G., Milne, and J. Davis, Glacial isostatic adjustment on a rotating Earth, *Geophys. J. Int*., 147, 562–578, 2001.

Mitrovica, J., J. Wahr, I. Matsuyama, and A. Paulson, The rotational stability of an ice age Earth, *Geophys. J. Int.*, doi:10.111/j.1365-246X.2005.02609.x, 2005.

Morris, C.S. and S.K. Gill, Evaluation of the TOPEX/POSEIDON altimeter system over the Great Lakes, *J. Geophys. Res*., 99, 24527-24539, 1994.

Nakada, M., R. Kimura, J. Okuno, K. Moriwaki, H. Miura, and H. Maemoku, Late Pleistocene and Holocene melting history of the Antarctic ice sheet derived from sea-level variations, *Mar. Geol.*, 167, 85-103, 2000.

Nerem, R. and G. Mitchum, Estimates of vertical crustal motion derived from differences of TOPEX/POSEIDON and tide gauge sea level measurements, *Geophys. Res. Lett.*, 29 (19), 1934, doi:10.1029/2002G015037, 2002.

Pagiatakis, S.D. and P. Salib, Historical relative gravity observations and the time rate of change of gravity due to postglacial rebound and other tectonic movements in Canada, *J. Geophys. Res.*, 108 (B9), 2406, doi:10.1029/2001JB001676, 2003.

Papa, F., B. Legresy, N.M. Mognard, E.G. Josberger, and F. Remy, Estimating terrestrial snow depth with the Topex-Poseidon altimeter and radiometer, *IEEE Trans. Geosci. Remote Sens.*, 40, 2162-2169, 2002.

Papa, F., B. Legresy, and F. Remy, Use of the Topex-Poseidon dual-frequency radar altimeter over land surfaces, *Remote Sens. Environ.*, 87, 136-147, 2003.

Paulson, A., S. Zhong, and J. Wahr, Modeling post-glacial rebound with lateral viscosity variations, *Geophys. J. Int*., 163, 357–371, doi:10.111/j.1365-246X.2005.02645.x., 2005.

Paterson, W.S.B., The physics of glaciers, 3rd edition, Pergamon, Elsevier Science Ltd, 1994.

Peltier, W.R., Ice age Paleotopography, *Science*, 265, 195-201, 1994.

Peltier, W.R., Global glacial isostatic adjustment: paleogeodetic and space-geodetic tests of the ICE-4G (VM2) model, *J. Quatern. Sci.*, 17, 491-510, 2002.

Peltier, W.R., Global glacial isostasy and the surface of the ice-age Earth: The ICE-5G (VM2) model and GRACE, *Annu. Rev. Earth Planet. Sci.*, 32, 111-149, 2004.

Ramillien, G., A. Lombard, A. Cazenave, E. Ivins, M. Llubes, F. Remy, and R. Biancale, Interannual variations of the mass balance of the Antarctica and Greenland ice sheets from GRACE, *Global Planet. Change*, 53, 198–208, 2006.

Rapley, C.G., M.A.J. Guzkowska, W. Cudlip, and I.M. Mason, An exploratory study of inland water and land altimetry using Seasat data, *ESA Rep. 6483/85/NL/BI*, Eur. Space Agency, Neuilly, France, 1987.

Remy, F., B. Legresy, and J. Benveniste, On the Azimuthally Anisotropy Effects of Polarization for Altimetric Measurements, *IEEE Trans. Geosci. Remote Sens.*, 44, 3289-3296, 2006.

Rignot, E., Evidence for rapid retreat and mass loss of Thwaites Glacier, West Antarctica, *J. Glaciol.*, 47, 213-222, 2001.

Rignot, E. and S. Jacobs, Rapid bottom melting widespread near Antarctic ice-sheet grounding lines, *Science*, 296, 2020-2023, 2002.

Rignot, E. and R.H. Thomas, Mass balance of polar ice sheets, *Science*, 297, 1502-1506, 2002.

Rignot, E., J.L. Bamber, M.R. van den Broeke, C. Davis, Y. Li, W.J. van de Berg, and E. van Meijgaard, Recent Antarctic ice mass loss from radar interferometry and regional climate modeling, N*ature Geoscience*, 1, 106-110.

Rodell, M., P.R. Houser, U. Jambor, J. Gottschalck, K. Mitchell, C.-J. Meng, K. Arsenault, B. Cosgrove, J. Radakovich, M. Bosilovich, J.K. Entin, J.P. Walker, D. Lohmann, and D. Toll, The Global Land Data Assimilation System, *Bull. Am. Meteorol. Soc.*, 85, 381-394, 2004.

Rodriguez, E., Altimetry for non-Gaussian oceans: height biases and estimation of parameters, *J. Geophys. Res.*, 93, 14107-14120, 1988.

Rodriguez, E. and B. Chapman, Extracting ocean surface information from altimeter returns: the deconvolution method, *J. Geophys. Res.*, 94, 9761-9778, 1989.

Sandwell, D.T. and B. Zhang, Global mesoscale variability from the Geosat Exact Repeat Mission: correlation with ocean depth, *J. Geophys. Res.*, 94(C12), 17971-17984, 1989.

Sella, G., S. Stein, T. Dixon, M. Carymer, T.S. James, S. Mazzotti, and R.K. Dokka, Observation of glacial isostatic adjustment in “stable” North America with GPS, *Geophys. Res. Lett.*, 34, L02306, doi:10.1029/2006GL027081, 2007.

Sturm, M., J. Holmgren, and G.E. Liston, A seasonal snow cover classification system for local to global applications, *J. Climate*, 8(5), 1261-1283, 1995.

Shepherd, A., D.J. Wingham, and J.A.D. Mansley, Inland thinning of the Amundsen Sea sector, West Anantarctica, *Geophys. Res. Lett.*, 29, doi:10.1029/2001GL014183, 2002.

Shepherd, A., D. Wingham, and E. Rignot, Warm ocean is eroding West Antarctic Ice Sheet, *Geophys. Res. Lett.*, 31, L23402, doi:10.1029/2004GL021106, 2004.

Shepherd, A. and D. Wingham, Recent sea-level contributions of the Antarctic and Greenland Ice Sheets, *Science*, 10.1126/science.1136776, 315, 2007.

Shum, C.K., R.A. Werner, D.T. Sandwell, B.H. Zhang, R.S. Nerem, and B.D. Tapley, Variations of global mesoscale eddy energy observed from Geosat, *J. Geophy. Res.*, 95(C10), 17865-17876, 1990.

Shum, C.K., Y. Yi, K.C. Cheng, C.Y. Kuo, A. Braun, S. Calmant, and D.P. Chambers, Calibration of Jason-1 altimeter over Lake Erie, *Marine Geodesy*, 26, 335-354, doi:10.1080/01490410390253487, 2003.

Shum, C.K., C.-Y. Kuo, and J.-Y. Guo, Role of Antarctic ice mass balance in present-day sea level change, *Polar Science*, in press, 2008.

Strawbridge, F. and S. Laxon, ERS-1 altimeter fast delivery data quality flagging over land surfaces, *Geophys. Res. Lett.*, 21, 1995-1998, 1994.

Tamisiea, M.E., J.X. Mitrovica, and J.L. Davis, GRACE gravity data constrain ancient ice geometries and continental dynamics over Laurentia, *Science,* 316, doi:10.1126/science,1137157, 2007.

Tapley, B.D., S. Bettadpur, M. Watkins, and C. Reigber, The gravity recovery and climate experiment: Mission overview and early results, *Geophys. Res. Lett.*, 31, L09607, doi:10.1029/2004GL019920, 2004.

Templet, P. and K. Meyer-Arendt, Louisiana wetland loss: a regional water management approach to the problem, *Environ. Manage.*, 12, 181-192, 1988.

Thomas, R., E. Rignot, G. Casassa, P. Kanagaratnam, C. Acuna, T. Akins, H. Brecher, E. Frederick, P. Gogineni, W. Krabill, S. Manizade, H. Ramamoorthy, A. Rivera, R. Russell, J. Sonntag, R. Swift, J. Yungel, and J. Zwally, Accelerated sea-level rise from West Antarctica, *Science*, 306, 255–258, 2004.

Tushingham, A.M. and W.R. Peltier, ICE-3G: A new model of Pleistocene deglaciation based upon geophysical predictions of postglacial relative sea level change, *J.*

Geophy. Res., 96, 4497-4523, 1991.

Ulaby, F.T., R.K. Moore, and A.K. Fung, Microwave Remote Sensing. Active and Passive, Vol II: Radar Remote Sensing and Surface Scattering and Emission Theory, Addison-Wesley Publishing Company, 1982.

Ulaby, F.T., R.K. Moore, and A.K. Fung, Microwave Remote Sensing. Active and Passive, Vol III: From Theory to Applications, Addison-Wesley Publishing Company, 1986.

van den Broeke, M., W.J. van de Berg, and E. Van Meijgaard, Snowfall in coastal West Antarctica much greater than previously assumed, *Geophys. Res. Lett.*, 33, L02505, doi:10.1029/2006GL025239, 2006.

van der Wal, W., P. Wu, M.G. Sideris, and C.K. Shum, Use of GRACE determined secular gravity rates for glacial isostatic adjustment studies in North-America, *J. Geodyn.*, doi:10.1016/j.jog.2008.03.007, 2008.

Vaughan, D.G., J.L. Bamber, M. Giovinetto, J. Russell, and A.P.R. Cooper, Reassessment of net surface mass balance in Antarctica, *J. Climate*, 12, 933-946, 1999.

Vaughan, D., How does the Antarctic Ice Sheet affect sea level rise? *Science*, 308, 1877–1888, 2005.

Visser, J., C. Sasser, R. Chabreck, and R. Linscombe, Marsh vegetation types of the Mississippi River deltaic plain, *Estuaries*, 21, 818-828, 1998.

Visser, J., C. Sasser, R. Linscombe, and R. Chabreck, Marsh vegetation types of the Chenier Plain, Louisiana, USA, *Estuaries*, 23, 318-327, 2000.

Velicogna, I. and J. Wahr, Measurements of time-variable gravity show mass loss in Antarctica, *Science*, 311,1754-1756, 2006a.

Velicogna, I. and J. Wahr, Acceleration of Greenland ice mass loss in spring 2004, *Nature*, 443, doi:10.1038/nature05168, September 2006b.

Wahr, J., D. Han, and A. Trupin, Predictions of vertical uplift caused by changing polar ice volumes on a viscoelastic Earth, *Geophys. Res. Lett*., 22, 977–980, 1995.

Wahr, J., M. Molenaar, and F. Bryan, Time variability of the Earth's gravity field: hydrologic and oceanic effects and their possible detection using GRACE, *J. Geophys. Res.*, 103(B12), 30205-30229, 1998.

Wahr, J., D. Wingham, and C. Bentley, A method of combining ICESAT and GRACE satellite data to constrain Antarctic mass balance, *J. Geophs. Res*., 105, 16279–16294, 2000.

Walker, J., J. Coleman, H. Roberts, and R. Tye, Wetland loss in Louisiana, *Geogr. Ann.*, 69A(1), 189-200, 1987.

Wang, H. and P. Wu, Effects of lateral variations in lithospheric thickness and mantle viscosity on glacially induced surface motion on a spherical, self-gravitating Maxwell Earth, *Earth Planet. Sci. Lett.*, 244, 576-589, 2006a.

Wang, H. and P. Wu, Role of background viscosity in the investigation of postglacial rebound induced crustal motion in a laterally heterogeneous mantle, *J. Geodyn.*, 42, 85-94, 2006b.

Wang, H., P. Wu, and W. van der Wal, Using postglacial sea level, crustal velocities and gravity-rate-of-change to constrain the influence of thermal effects on mantle lateral heterogeneities, *J. Geodyn*., doi:10.1016/j.jog.2008.03.003, 2008.

Wdowinski, S., F. Amelung, F. Miralles-Wilhelm, T.H. Dixon, and R. Carande, Space-based measurements of sheet-flow characteristics in the Everglades wetland, Florida, *Geophy. Res. Lett.*, 31, L15503, doi:10.1029/2004GL020383, 2004.

Wehr, T. and E. Attema, Geophysical validation of ENVISAT data products, *Adv. In Space Res*, 28, 83-91, 2001.

Wessel, P. and W.H.F. Smith, Generic Mapping tools, 6, http://imina.soest.hawaii-edu/gmt, 2001.

Wingham, D., A. Ridout, R. Scharroo, R. Arthern, and C. Shum, Antarctic elevation change from 1992 to 1996, *Science* 282, 456–458, 1998.

Wingham, D., A. Shepherd, A. Muir and G. Marshall, Mass balance of the Antarctic ice sheet, *Phil. Trans. R. Soc. A,* 364, 1627–1635, doi:10.1098/rsta.2006.1792, 2006a.

Wingham, D., C. Francis, S. Baker, C. Bouzinac, D. Brockley, R. Cullen, P. de Chateau-Thierry, S. Laxon, U. Mallow, C. Mavrocordatos, L. Phalippou, G. Ratier, L. Rey, F. Rostan, P. Viau, and D. Wallis, CryoSat: A mission to determine the fluctuations in Earth's land and marine ice fields, *Adv. In Space Res.,* 37, 841–871, 2006b.

Wu, P., and W. van der Wal, Postglacial sea levels on a spherical, self-gravitating viscoelastic earth: effects of lateral viscocity variations in the upper mantle on the inference of viscosity contrasts in the lower mantle, *Earth Planet. Sci. Lett.*, 211, 57–68, 2003.

Wu, P., Using commercial finite element packages for the study of Earth deformations, sea levels and the state of stress, *Geophys. J. Int*, 158, 401–408, 2004.

Wu, P., Effects of lateral variations in lithospheric thickness and mantle viscosity on glacially induced surface motion in Laurentia, *Earth Planet. Sci. Lett.*, 235, 549-563,

2005.

Wu, P., Sensitivity of relative sea levels and crustal velocities in Laurentide to radial and lateral viscosity variations in the mantle, *Geophys. J. Int.*, 165, 401-413, 2006.

Yi, Y., OSU Stackfile, Department of Civil and Environmental Engineering and Geodetic Science, Ohio State Univ., USA, 2000.

Zwally, H.J., A.C. Brenner, J.A. Major, R.A. Bindscadler, and J. Marsh, Growth of Greenland Ice Sheet: Measurement, *Science*, 246, 1587-1589, 1989.

Zwally, H.J., GSFC Retracking Algorithms, *http://icesat4.gsfc.nasa.gov/*, 1996.

Zwally, H.J. and A.C. Brenner, Ice Sheet Dynamics and Mass Balance. In: L.-L. Fu and A. Cazenave (editors), Satellite Altimetry and Earth Sciences: A Handbook of Techniques and Applications, Elsevier, New York, 351-369, 2001.

Zwally, H.J. and J. Li, Seasonal and interannual variations of firn densification and ice-sheet surface elevation at the Greenland summit, *J. Glaciol.*, 48, 199-207, 2002.

Zwally, H., M. Giovinetto, J. Li, H. Cornejo, M. Beckley, A. Brenner, J. Saba, and D. Yi, Mass changes of the Greenland and Antarctic ice sheets and shelves and contributions to sea-level rise: 1992–2002, *J. Glaciol.*, 51, 509–527, 2005.